Rapid and Agile Locomotion with Power-dense Millirobots

by

Duncan Ward Haldane

A dissertation submitted in partial satisfaction of the

requirements for the degree of

Doctor of Philosophy

in

Engineering - Mechanical Engineering

in the

Graduate Division

of the

University of California, Berkeley

Committee in charge:

Professor Ronald S. Fearing, Co-chair
Professor Alice M. Agogino, Co-chair
Professor Oliver M. O'Reilly
Professor Ruzena Bajcsy

Spring 2017

Rapid and Agile Locomotion with Power-dense Millirobots

Abstract

Rapid and Agile Locomotion with Power-dense Millirobots

by

Duncan Ward Haldane

Doctor of Philosophy in Engineering - Mechanical Engineering

University of California, Berkeley

Professor Ronald S. Fearing, Co-chair

Professor Alice M. Agogino, Co-chair

The development of legged robots can serve two purposes. The first is to enable more mobility for robotic platforms and allow them greater flexibility for moving through complex real-world environments. The second is that the legged robot is a scientific tool. It can be used to design new experiments that drive insights both for the development of new robotic platforms and the characteristic of animal locomotors from which they are inspired. This work presents a design methodology that targets the creation of extreme robotic locomotors. These are robots that outperform all others at a particular task. They are used to study locomotion at the edge of the current performance envelope for robotic systems.

The design methodology focuses on maximizing the power-density of the platform. We apply it to create first a rapid running robot, the X2-VelociRoACH, and two versions of a jumping robot, Salto and Salto-1P. In all of these robots, we centralize the actuation such that one actuator provides all the power for the energetic locomotory tasks. A kinematic coupling is designed for each platform, such that the correct behavior (running or jumping) happens by default when the energetic actuator is driven open-loop. The design methodology successfully created two robots at the edge of their respective performance envelopes.

The X2-VelociRoACH is a 54 gram experimental legged robot developed with this methodology that was developed to test hypotheses about running with unnaturally high stride frequencies. It is capable of running at stride frequencies up to 45 Hz, and velocities up to 4.9 m/s, making it the fastest legged robot relative to size. The top speed of the robot was limited by structural failure. High-frequency running experiments with the robot shows that the power required to cycle its running appendages increase cubically with the stride rate. Our findings show that although it is possible to further increase the maximum velocity of a legged robot with the simple strategy of increasing stride frequency, considerations must be made for the energetic demands of high stride rates.

For the development of the jumping robot Salto, we first devise the vertical jumping agility metric to identify a model animal system for inspiration. We found the most agile

animals outperform the most agile robots by a factor of two. The animal with the highest vertical jumping agility, the galago (*Galago senegalensis*), is known to use a power-modulating strategy to obtain higher peak power than that of muscle alone. Few previous robots have used series-elastic power modulation (achieved by combining series-elastic actuation with variable mechanical advantage), and because of motor power limits, the best current robot has a vertical jumping agility of only 55% of a galago. Through use of a specialized leg mechanism designed to enhance power modulation, we constructed a jumping robot that achieved 78% of the vertical jumping agility of a galago. The leg mechanism also has constraints which assure rotation-free jumping motion by default. Agile robots can explore venues of locomotion that were not previously attainable. We demonstrate this with a wall jump, where the robot leaps from the floor to a wall and then springs off the wall to reach a net height that is greater than that accessible by a single jump. Our results show that series-elastic power modulation is an actuation strategy that enables a clade of vertically agile robots.

We extend the work with Salto to see how the locomotory capacity of an extreme robotic locomotor can be extended without compromising the power density of the platform. Salto-1P uses aerodynamic thrusters and an inertial tail to control its attitude in the air. A linearized Raibert step controller was sufficient to enable unconstrained in-place hopping and forwards-backwards locomotion with external position feedback. We present studies of extreme jumping locomotion in which the robot spends just 7.7% of its time on the ground, experiencing accelerations of 14 times earth gravity in its stance phase. An experimentally collected dataset of 772 observed jumps was used to establish the range of achievable horizontal and vertical impulses for Salto-1P.

Contents

List of Figures

List of Tables

Acknowledgments

Many people and organizations contributed time and resources to support the research in this dissertation. Material support was provided by the National Science Foundation under IGERT Grant No. DGE-0903711, Grant No. CNS-0931463, NSF CMMI-1549667, and the NSF Graduate Research Fellowship Program. Additional support was provided by the United States Army Research Laboratory under the Micro Autonomous Science and Technology Collaborative Technology Alliance.

First I would like to thank my advisor Ron Fearing from whom I have learned so much. The dissertation committee has shared their time and experience during the preparation of this work. I would specifically like to thank professors Oliver O'Reilly, Shankar Sastry, Robert Dudley, Robert Full, Mimi Koehl, Alice Agogino, Dennis Lieu, Ruzena Bajcsy, and Pieter Abbeel for teaching me few things over the years. The CiBER-IGERT traineeship program has provided invaluable support, mentorship and preparation for the planning, execution and presentation of academic research.

Special thanks to Max Donelan and Tom Libby for numerous and energetic discussions on comparative biomechanics, dynamics, tails, and metrization. I have been able to work with an incredible set of collaborators over the years including Kevin Peterson, Fernando L. Garcia Bermudez, Mark Plecnik, and Justin Yim. Special thanks too to Austin Buchan for his help with custom drive electronics, general savvy, and friendship.

Chapter 1

Introduction

In this work we present a design methodology for creating mobile robots that have extreme performance for energetic tasks like rapid running and jumping. The study of rapid locomotion is interesting because as we seek to build ever improving legged robots, it is a useful exercise to investigate the efficacy of locomotion strategies in their respective limits. By having knowledge of system behavior at extremes we can more effectively guide the development of future platforms. Energetic jumping allows great locomotory flexibility. Humans participating in the sport of parkour opportunistically reach for disparate handholds and footholds on urban features such as walls, banisters, and railings. Arboreal animals leap between branches, and mountain goats bound across cliff faces. The farther a system can leap, the greater is its reach, and the larger the set of available footholds becomes. These are examples of agile behaviors, and at present, robots fall short of the jumping performance shown by these extreme animal locomotors. This mode of locomotion is interesting for robotics because it enables rapid movement through complex terrain and added flexibility for how the robot interacts with the environment. The farther a robot can jump the better it can discretize its environment, clearing larger gaps and obstacles and making path-planning easier [24]. A robot proficient at jumping locomotion would be able to move through its environment in new and previously insupposable ways.

The power density of a platform sets the limit on how quickly it can increase its energetic state. To extremize the ability of robots to perform energetic tasks, we present a power-density-first design methodology. The basis of this design methodology is that the robot's capacity for doing energetic work is centralized and assigned to a single power-dense actuator. This strategy increases the power density in a number of ways. The higher the ratio of the mass of the actuator to the mass of the rest of the robotic system, the higher the power density of the platform. If the locomotory system of a robot includes actuators that do not actively propel the robot, their mass and complexity reduce the power density of the robot. In addition, if multiple energetic actuators are used, they work against each other when performing dynamic tasks (reducing the effective power density) unless specific kinematic considerations are made [1].

There are a number of methods that have been used to allow a single actuator to perform

coordinated behaviors. Referred to as uni-drive robots, the single-actuator design of these systems is motivated by a reduction in mass and complexity [78]. These robots replace actuators with a series of clutches attached to a mechanical power distributor such as a flexible shaft. This actuation paradigm is then applied to create traditional robotic structures like an x-y gantry [57], a hyper-redundant manipulator [4], or a three-fingered hand [54]. Although a uni-drive system centralizes actuation, a number of engineering considerations makes it a poor fit for a dynamic locomotory robot. Flexible shafts have high transmission losses and the clutches still impose considerable mechanical complexity (and mass). An alternative approach is to create a singly actuated mechanism that performs the locomotory task without the need for multiple active degrees of freedom. This mechanism is designed such that the desired behavior happens by default. For example, the mechanism in a running robot should produce stable running motion when the energetic actuator is driven open-loop. The mechanism translates a power input a dynamic locomotory output. This strategy increases the power density of the platform when the mechanism can be instantiated with less mass and effective power loss than another strategy.

In this work we apply this strategy to design a rapid running robot, described in Chapter2. In Chapter 3 we apply the same power-density-first design strategy to create an agile jumping robot. We extend the agile robotic research with Chapter4 in which we explore adding additional mass-minimal stabilizing actuators that enable spatial jumping. The prior work and state-of-the-art is summarized in each chapter individually as opposed to an aggregated presentation.

1.1 Summary of contributions

The contributions of this work fall in two main categories. The first is the underlying power-density-first approach used to create the robotic platforms in this work. The substantiating evidence of the method's efficacy are the world records set by these robots. The rapid running robot sets the speed record (relative to size) for legged robots. Part of the agile research was to determine an appropriate metric to measure the performance of robotic (and animal) jumpers. This metric is vertical jumping agility, and the two versions of the jumping robot successively set the world record in vertical jumping agility for battery-powered robots.

The second category of contributions are insights into the properties of and strategies for robotic locomotion. We demonstrate that the speed of a robotic platform can be increased by increasing the stride frequency without encountering a kinematic or a traction limit. The top speed is limited by material failure, and we find that it becomes energetically unfavorable to run at the highest achievable speed. Another contribution is evidence for the efficacy of a new actuation strategy (based upon a series-elastic actuator with a variable mechanical advantage) for jumping robots. The strategy increases the peak power of a jumper without hampering force controllability. We demonstrate that a highly agile jumping robot can use a novel wall-jumping maneuver to gain energy and height. Finally it is shown that aerodynamic thrusters enable attitude control for a small legged robot, and that a Raibert-style controller

is sufficient for repetitive and controlled jumping.

Chapter 2

Rapid Locomotion

2.1 Introduction

In this chapter we apply the power-density-first design methodology to create a rapid running robot shown in Fig.2.1.

Animals have a well-defined approach to running at high velocities. Fig. 2.2 is a plot of stride frequency vs. non-dimensional speed for the VelociRoACH [42] and *P. americana*, the American cockroach. Non-dimensional speed is defined as the Froude number, $F = \frac{v}{\sqrt{gl}}$, where v is running speed, g is the gravitational constant, and l is leg length. This quantity allows comparision of running systems across size scales. The running dynamics of *P. americana* were used to establish targets for the VelociRoACH, and previous research has shown that the two systems are dynamically similar [39, 42]. The difference between the trends in this figure signify a fundamental difference between running animals and running robots. The knee in the cockroach data in Fig.2.2 indicates the stride frequency limit, the point at which the musculo-skeletal locomotory system of the cockroach can drive the legs no-faster. This limit exists for multiple species [32], such as ghost crabs [15], dogs [47], and cheetahs [52]. The common trend across these species is that the animal will run near its stride frequency limit, and increase velocity by increasing stride length. This is as opposed to the trend in the VelociRoACH data wherein the speed increases linearly with stride frequency. The VelociRoACH's leg kinematics are not easily changed because they are rigidly defined by kinematic structures which couple the output of two separate motors to drive a total of six legs [42].

Limitations on stride kinematics are common across many dynamic running robots. iSprawl [59] had only a single drive actuator, with two servos to adjust the angle of each middle leg in the saggital plane. The RHex robot has a total of six motors, each controlling the angle of one of its six legs. Kinematic adaptations which would increase the stride length of these robots are possible, but they incur a cost in complexity either in hardware, control, or both. The other option to increase speed is to simply increase the stride frequency of the system without altering the kinematics. This is the strategy adopted by VelociRoACH. As

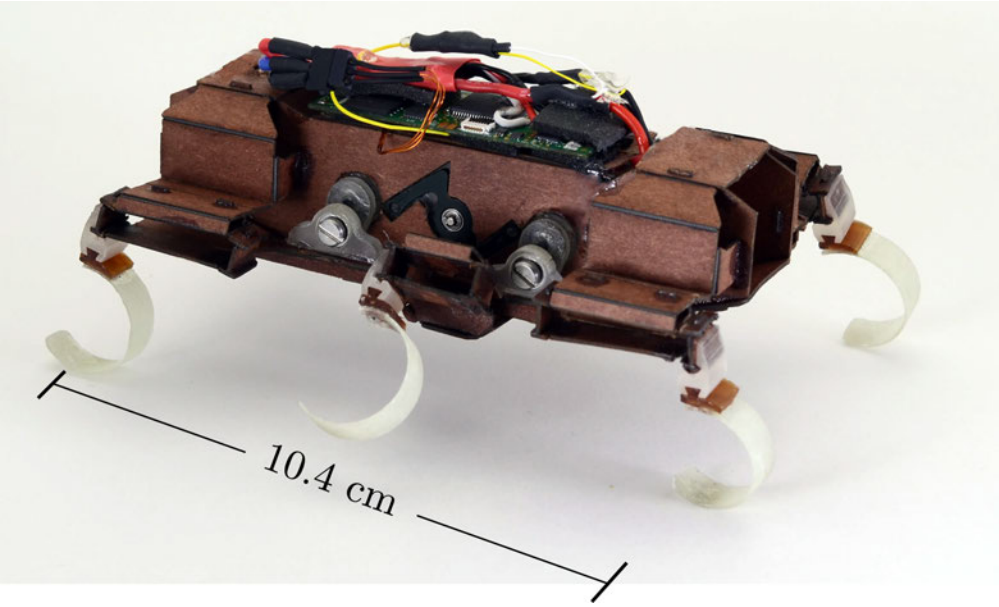

Figure 2.1: The X2-VelociRoACH, built to test hypotheses about high-frequency running. Adapted from [38].

shown in Fig.2.2, the stride frequency was simply increased until the robot reached the same non-dimensional velocity as the cockroach. This stride frequency is unnaturally high for a running system of VelociRoACH's mass.

The stride frequency limit of an animal can generally be predicted by its body mass [32]. This result is an effect of underlying principles of dynamic similarity across a wide array of terrestrial animals [3, 16]. These principles establish underlying locomotory dynamics which are invariant across size scales. Given several animal examples, gait characteristics such as velocity or stride frequency can be determined for a robotic system using dynamic similarity scaling [42, 5, 26]. The stride frequency limit for several animals is plotted against their body mass in Fig. 2.3. Dynamic scaling expects that the stride frequency of smaller animals will be higher than that of larger animals[1]. Also shown in Fig.2.3 are the masses and stride frequency limits of several running robotic platforms. All of these platforms are capable of a higher stride frequency than an animal of the same mass would be expected to use. Engineered systems such as these legged robots are not subject to the same physiological constraints as their animal counterparts, so it is reasonable that these robots have used an increased stride frequency to increase the span of velocities that they are able to achieve. An area that has not been fully explored is what happens when the stride frequency of a robot is pushed even higher. The trade-offs that occur in this operating regime have not been assessed. Addressing these questions, and the effect of system power density, will inform the design of future running robots.

[1]The stride frequency scales with $\sim \alpha_M^{-0.17}$ where α_M is the ratio of masses of the two systems being compared.

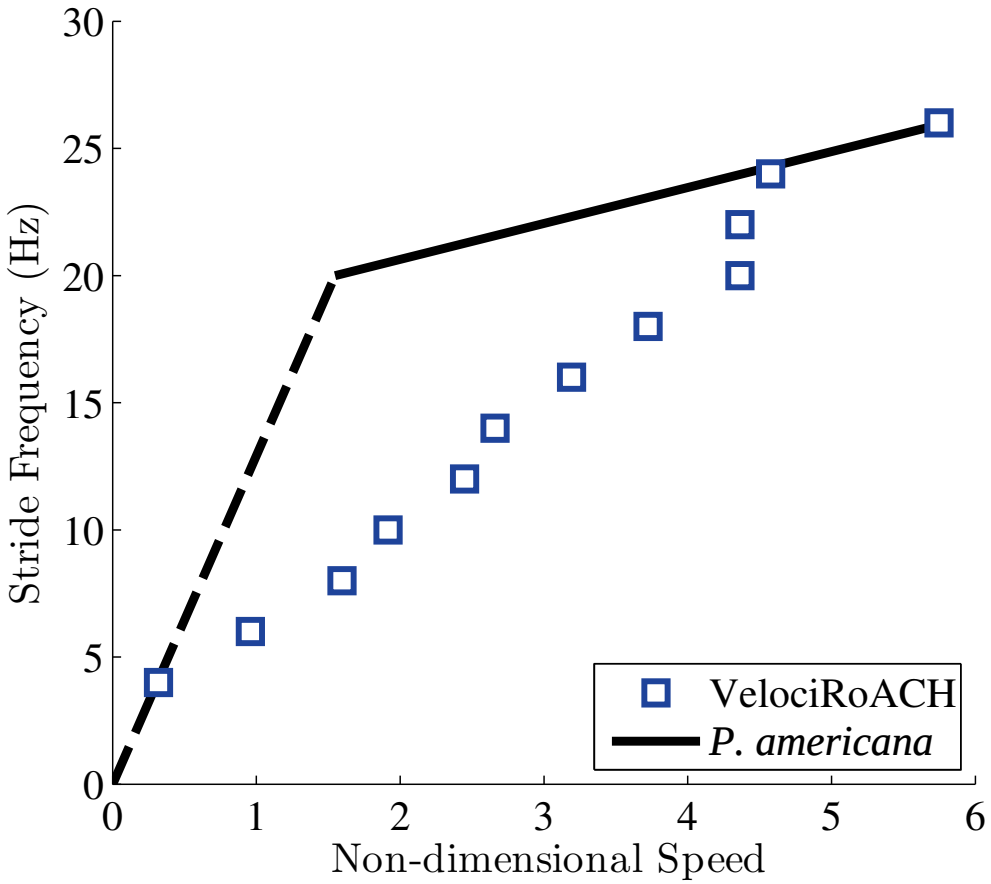

Figure 2.2: Stride frequency vs. non-dimensional speed for the American cockroach (trend-line extracted from Full & Tu [34]) and VelociRoACH [42]. The non-dimensional speed is equivalent to the Froude number (defined in text). The dotted line indicates walking behaviors, the solid line indicates running. The VelociRoACH has a running gait (defined by the presence of an aerial phase) above 8 Hz. Adapted from [38].

In this work we present the design of the experimental robotic platform, X2-VelociRoACH, which has been created to test what happens to legged locomotion in the frequency limit. The design and fabrication of the platform is shown in Section 2.2. Results from high-frequency running experiments are given in Section 2.3. The power consumption characteristics of gaits with unnaturally-high stride frequencies are given in Section 2.4.

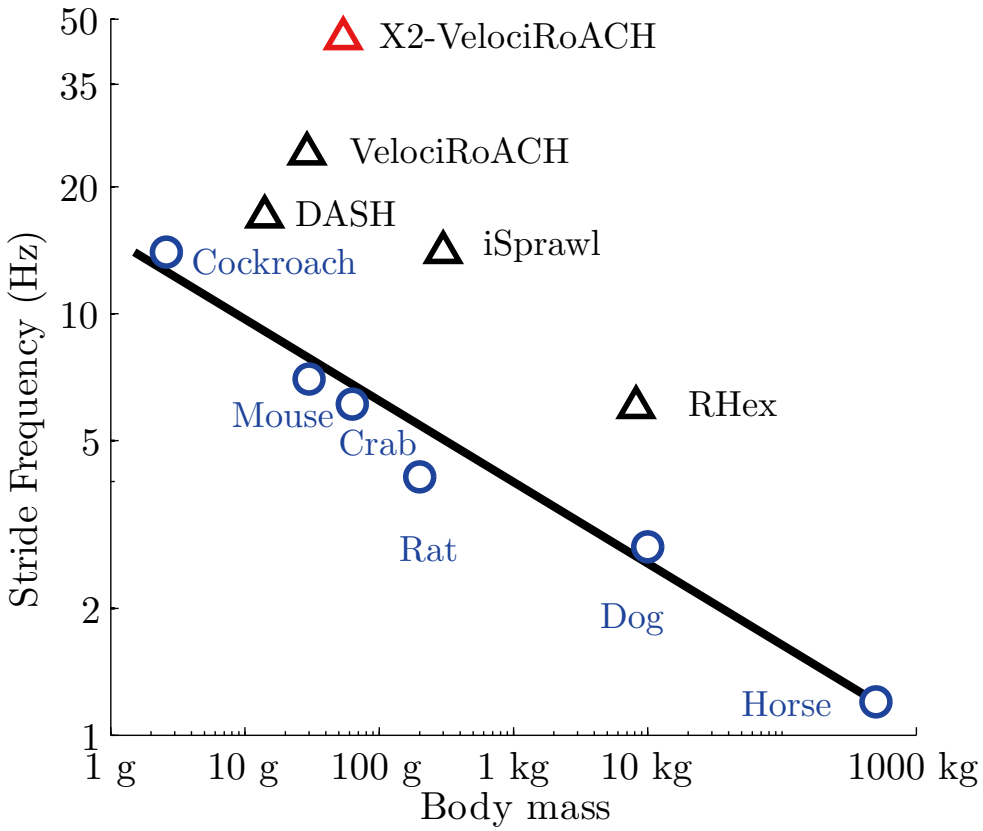

Figure 2.3: Stride frequency vs. body mass for a range of running animals and robots. Animal data from Full [32]. The X2-VelociRoACH presented in this work has the highest stride frequency of any extant running robot. Adapted from [38].

2.2 Methods

Design and Construction of the X2-VelociRoACH

The X2-VelociRoACH was built to test how the power-density-first design strategy can be used to increase the running speed and energetic capacity of a running robot. We based the design on the extant running robot, VelociRoACH. VelociRoACH was made using the Smart Composite Microstructures (SCM) process which creates linkages by combining rigid and flexible materials using planar processes [50]. It has been used to create several milliscale [13, 81, 51, 42] and microscale [10, 49] legged robots. Linkages made with SCM have been used reduce the requisite number of actuators for legged robots which allows for the use of larger, more power dense actuators. The geometric parameters of the SCM kinematic linkages which couple motor rotation to leg motion were maintained between VelociRoACH and the X2-VelociRoACH, so both robots have the same stride kinematics. This allows for a point of direct comparison to the prior art. A number of challenges had to be overcome

to make the X2-VelociRoACH a reality. Firstly, the power density of the platform had to increase to make more power available for cycling the legs more quickly. Secondly, the coupling between the motor and the SCM linkages had to be rigidified. The robustness of the SCM components had to be increased to cope with the loads exerted on the robot by the legs.

Power transmission

The original VelociRoACH used two coreless brushed DC motors to drive its legs, one for either side of the robot [42]. To increase the power density of the new platform we replaced these motors with a single out- runner brushless motor the *Air King AX-1306*. This motor has a listed voltage constant of $K_v = 2200\frac{\text{rpm}}{\text{V}}$, phase winding resistance of 0.88Ω, and current limit of 6A. We statically measured the torque constant to be $5.5\frac{\text{mNm}}{\text{A}}$, which indicates a somewhat lower K_v of $1720\frac{\text{rpm}}{\text{V}}$. The estimated maximum rotational frequency (for a 7.4V battery, after gearing down by 2.48:1) is then 85 Hz; the maximum torque produced would be 81 mNm. This motor weighs nine grams and has a peak output power of 6.5 W after gearing. X2-VelociRoACH therefore has significantly more power than VelociRoACH, whose two motors have a combined peak power output of 1.3 W.

The hobby-grade motor used in the X2-VelociRoACH is far less expensive than high-quality brushless motors like the *Faulhaber 0602*[2] and is more power-dense (but less efficient). The out-runner form factor of the motor allows for a large gap radius, reducing the requisite gear ratio. In conjunction with the smart composite microstructures process, the low cost allows us to stay within the paradigm of ultra-low cost microrobots, to which VelociRoACH belongs. For all their advantages hobby-grade motors of this type have a major downside for the purposes of legged robotics: they have no Hall effect sensors to specify commutation of the motor. Lacking a specialized micro-scale brushless motor controller, we have employed a hobby-grade sensorless electronic speed controller (ESC) (*Hobbyking 6A ESC*). Controllers of this type measure the back-EMF generated by the spinning motor to control commutation which has several implications: they have a high minimum speed, and they do not cope well with varying loads. This second point is critical, the inability of these controllers to cope with the slightly varying loads from a flapping mechanism in a MAV [66] caused complications; the impact loads generated by legged locomotion cause greater ones (see Section 2.3).

The X2-VelociRoACH's transmission is shown in Fig 2.4. The brushless motor drives two cranks through a single 2.48:1 reduction, which puts the maximum power point of the motor at a stride frequency of 50 Hz. This dual drive constrains the drive layer of the robot to be parallel, replacing the parallel four-bar mechanism that served the same function in VelociRoACH [42]. Previous SCM robots [42, 51, 81] used a simple pin-bushing connection to couple crank rotation to the SCM layer. This strategy did not properly constrain the drive plate at high velocities so we employed bearings mounted in 3D printed plastic, which were connected to the crank with a shoulder bolt (as can be seen in Fig. 2.1). We sought

[2]Which has been used in other small scale robots, e.g. [21]

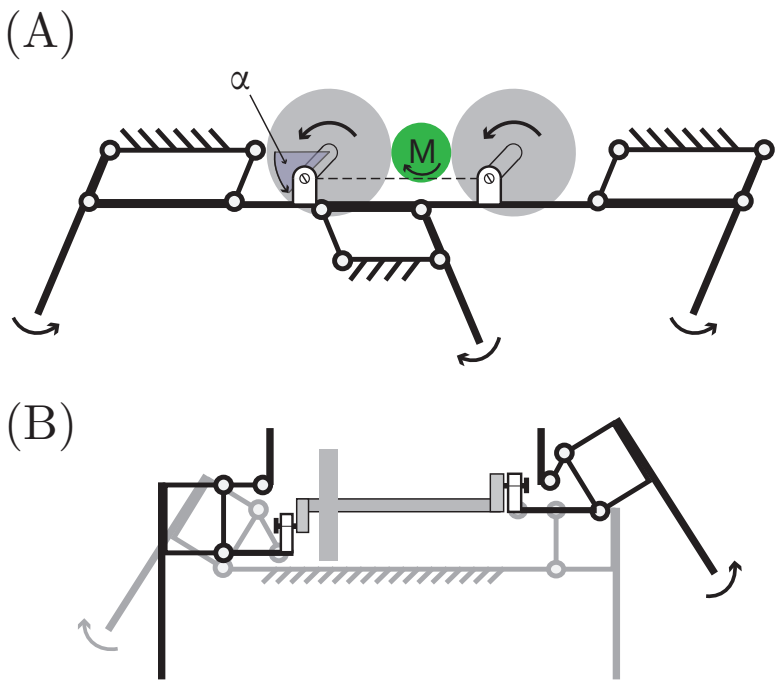

Figure 2.4: A conceptual kinematic drawing of the X2-VelociRoACH's drive mechanism. (A) A side view of the mechanism. The motor (shown in green) drives two parallel crankshafts through two gears (shown in gray). (B) A front view of the mechanism showing how the driven cranks are offset by 180°, thereby constraining the gait to alternating tripod. The crank angle α is also shown on the figure. Adapted from [38].

to enable the rapid fabrication of this robot, thus the majority of the transmission was 3D printed, including the gears. The 3D printed plastic material was not strong enough to use as a drive shaft so hollow shafts were printed, which were internally reinforced with carbon-fiber tubing.

This transmission physically constrains the gait of the X2-VelociRoACH to alternating tripod, as shown in Fig.2.4B, meaning it cannot use differential steering like previous robots [42, 81]. However we have shown that simple differential steering is not desirable for repeatable dynamic running [22], and steering can be more readily accomplished using a multi-functional inertial [61], or aerodynamic [60] appendage. Steering is unnecessary for the experimental goals for the X2-VelociRoACH; it can be added later to enable field operation.

Damage mitigation

It has been proposed that animals running at high stride frequencies incur higher peak forces [52]. This is certainly the case with the X2-VelociRoACH. Materials which have been previously used to create SCM millirobots are unable to withstand the high loads that occur

in high frequency running. We observed that these loads are proportional to the inertia of the running appendages, so fiberglass legs were used. These legs were made with six layers of alternating $\pm 45°$ and $0°/90°$ S grade fiberglass in a wet-layup epoxy process. The fiberglass legs had an inertia of 62 g mm^2, 30% less than the rubber legs used by VelociRoACH [42].

In the past, 25 μm polyethylene terephthalate (PET) film has been used for the flexure layer of several robots [42, 51, 81]. A X2-VelociRoACH made with PET was tested to destruction to determine the achievable stride frequency limit. While running in air, the inertial forces from the recirculating limbs were enough to destroy the flexures before the stride frequency reached 45 Hz. On the ground, one three second run at 32 Hz was enough to tear flexures. Tendons made of Kevlar filament placed across flexures were able to extend the running life by a small amount, but these failed eventually as well. We experimented with a composite of tough Spectra fibers sandwiched between two sheets of polyester film (*Cuben Fabric*) as a flexure layer. This material is similar in dimension and bonding chemistry to the PET film, and greatly extended the running life of the robot. However, flexures made with this material still failed after a few trials of high frequency running, as shown in Fig.2.5a. We therefore decided to use rip-stop nylon (*1.9 oz Uncoated rip-stop nylon.* From *ripstopbytheroll.com*) as our flexure layer[3]. Flexures made with rip-stop nylon did not fail in any of our experiments. Instead, the rigid component of the SCM composite began to fail at the highest achievable stride frequencies, as shown in Fig.2.5b. This material failure sets the limit for the top speed of the robot.

Despite these material limits, the X2-VelociRoACH was able to run on the ground at stride frequencies up to 45 Hz without incurring significant damage. More dynamic performance from this robot is achievable if new materials and processes that further increase the durability of SCM robots are developed.

Control electronics

The X2-VelociRoACH is driven by the imageProc 2.5[4] [8] robot control board. Motor current measurements are unavailable from the sensorless speed controller, so a low-side shunt resistor was used to measure current consumption for the entire robot. We estimated the motor power by offsetting the total power consumption by the levels recorded while the motor is powered down. A Hall-effect based encoder was placed on the brushless motor output to determine the position of the legs. The imageProc collects telemetry data including current measurements, battery voltage level, 6-axis inertial measurements, and motor position at 1000 Hz. The integrated 802.15.4 radio interface was used for communication and external control[5]. A 7.4V, 180mAh battery powered the robot, lasting for approximately twenty minutes before needing recharging.

[3] This material is now used in the flexure layer of the commercialized version of the DASH robot

[4]Embedded board: https://github.com/biomimetics/imageproc_pcb

[5]Embedded code: https://github.com/dhaldane/roach

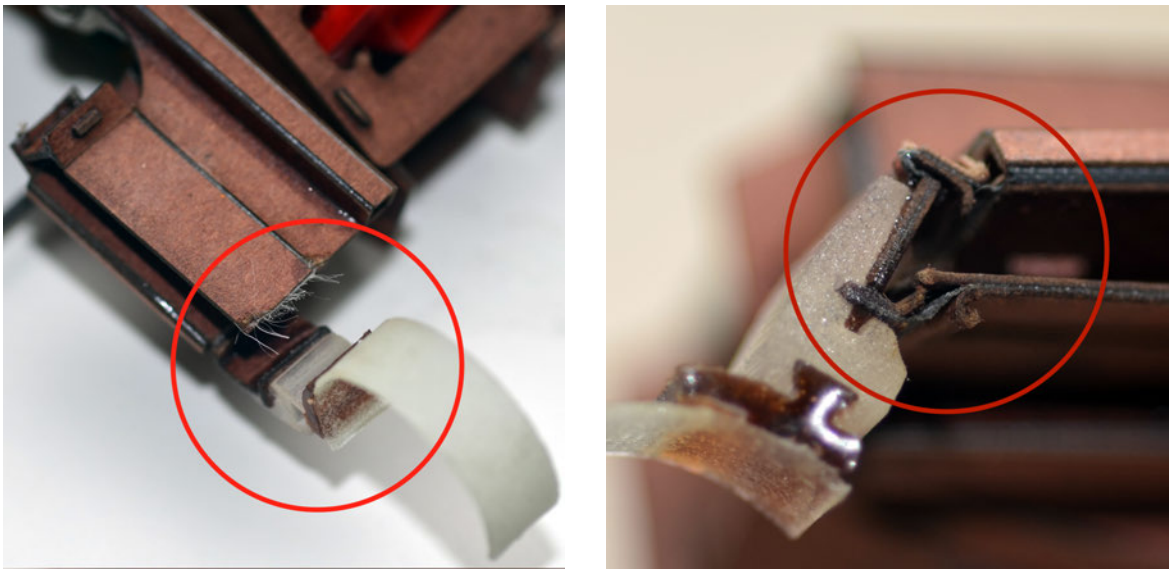

(a) A failed Cuben fabric flexure. Failure of this material was typified by fiber pullout.

(b) The rigid material failing by peeling at a hip flexure.

Figure 2.5: Failure modes of SCM mechanisms after high frequency running. Adapted from [38].

Experiments

A number of experiments were conducted to determine the characteristics of high-frequency running. The X2-VelociRoACH was run without the legs touching the ground to establish the cost of recirculating the legs in the absence of any interaction with the ground. During these experiments, the robot was held firmly by hand. Another set of off-the-ground experiments were run with the robot's legs removed to determine the contribution of appendage inertia to the overall cost. Running experiments across a wide range of speeds were conducted on level closed-pile carpet. Motion data was collected from the robot by recording high-speed video at 600 frames per second, and digitizing visual markers with *Pro-Analyst* motion analysis software.

To facilitate data collection, all experiments were run with the same aerodynamic stabilizer developed for VelociRoACH [42]. All experiments were run on the same robot, with on-ground running first, appendages in the air second, and without appendages in the air last. For each experiment, a range of open-loop throttle commands was sent to the sensorless speed controller to explore the span of achievable performance.

2.3 Results

Fig.2.6 shows several stills from a high-speed video of the robot running with a stride frequency of 45 Hz. These stills demonstrate behaviors typical to high frequency running.

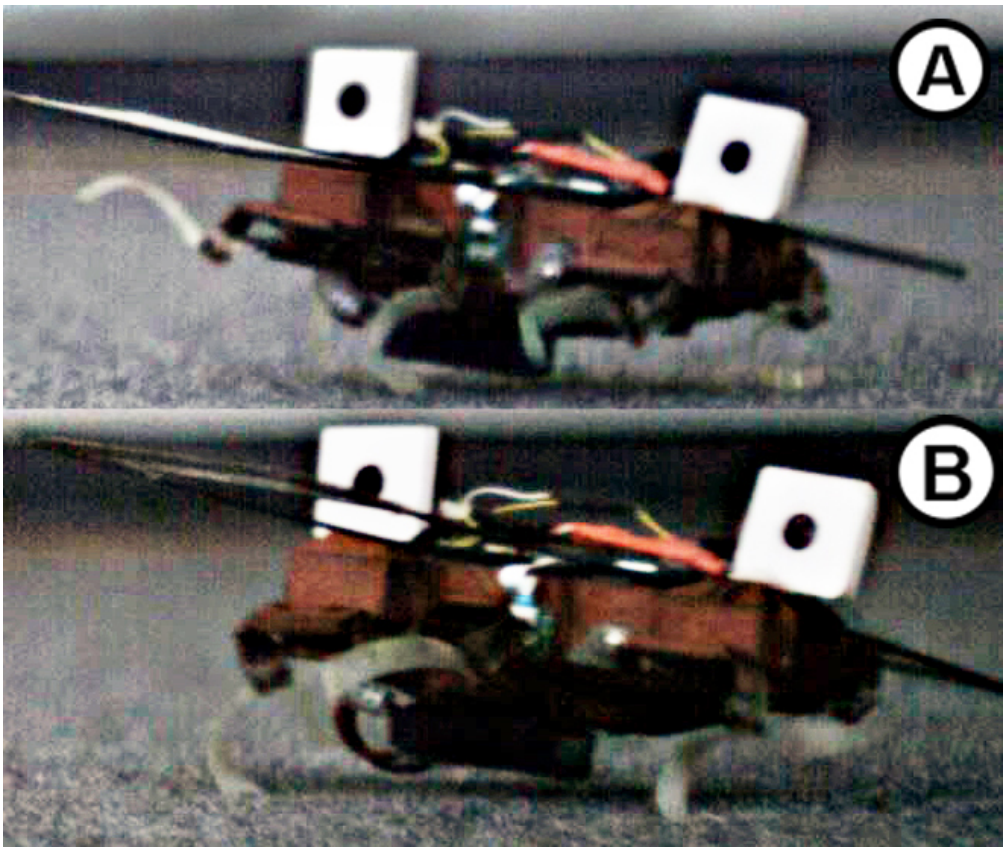

Figure 2.6: Stills from a high-speed video (583 fps) of the X2-VelociRoACH running at 45 Hz. Adapted from [38].

Fig.2.6A shows hyper-extension of the flexible 'C' legs. High inertial forces occuring during high frequency running tend to stretch out the robot's appendages. There is also a significant increase in the robot's range of leg angles; inertial forces acting on the semi-compliant SCM mechanisms cause increases in both abduction and adduction angle. At high velocities the touchdown angle of the leg approaches the vertical, as shown in Fig.2.6B. It should be noted that the battery of the X2-VelociRoACH is mounted on the bottom of the platform. It is very close to the ground, but never made contact in any of the experiments.

Fig.2.7 shows the fore-aft acceleration of the X2-VelociRoACH over approximately 70 strides during steady state running at 45 Hz. This figure demonstrates the strong periodicity of high-frequency running gaits. Well defined regions of positive and negative acceleration (as have been well documented in low-frequency running) can also be seen.

Fig.2.8 shows the speed of the X2-VelociRoACH as a function of stride frequency. The robot was unable to run at stride frequencies below 35 Hz due high impact loads interfering with the brushless ESC. Gaits in this lower frequency region were typified by repeated motor stalls followed by ~ 500 ms of rapid leg motion as the ESC attempted to generate a measurable back-EMF (electro-motive force) from the motor. This phenomena caused large

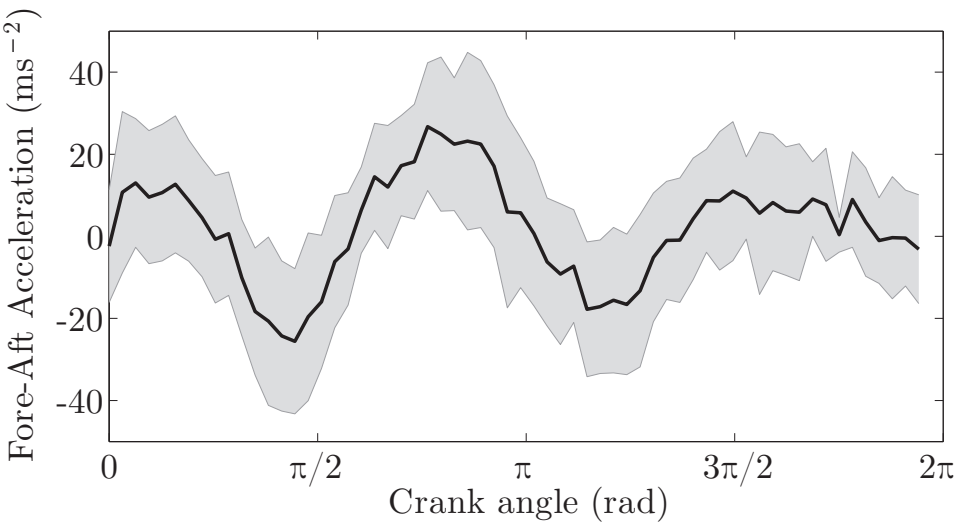

Figure 2.7: Fore-aft accelerations of the X2-VelociRoACH running at 45 Hz as a function of the crank angle. Approximately 70 strides were averaged, the shaded region is one standard deviation. Adapted from [38].

perturbations in height and pitch angle as the robot attempted to proceed forward.

Above 35 Hz, in the regime of stable running, the forward velocity increased linearly with stride frequency to a maximum of 4.9 m/s, without significant changes in slope. Also shown on the graph is a kinematic limit on the velocity of the robot. The peak leg tip velocity occurs at mid-stance (as described in previous works [22]). If the robot were on the boundary of the kinematic limit, it would be moving at this top speed over the entire stride. Fig.2.9 shows the average stride length of the robot as a function of stride frequency. The increasing trend in this graph shows that the robot travels a greater distance per stride at higher frequencies. This may be caused by an increase in the effective leg length caused by the aforementioned inertial forces. Alternatively, the robot could be generating impulses when the legs collide with the ground at high speeds. Because the leg touches down near the vertical these impulses would be propulsive, allowing the robot to generate additional thrust.

To estimate the effects of inertial loads during high-frequency locomotion we created a full simulation of the X2-VelociRoACH kinematic mechanism in Solidworks. Shown in Fig.2.10, this model has one degree of freedom and predicts the motor loading caused by inertial effects of the mechanism and appendages. The simulated motor drove the mechanism at a constant stride frequency, and Solidworks Motion was used to calculate the power required to produce the motion. Data from three of these simulations are presented in Fig. 2.11. The peak power required increases cubically with the stride frequency, as would be expected for an inertial load forced to track a sinusoidal position input. To validate the Solidworks simulation, data from the robot running in air at 40 Hz are presented in Fig.2.12. This plot shows the crank angle with the cyclic trend removed, as a function of time, over one stride

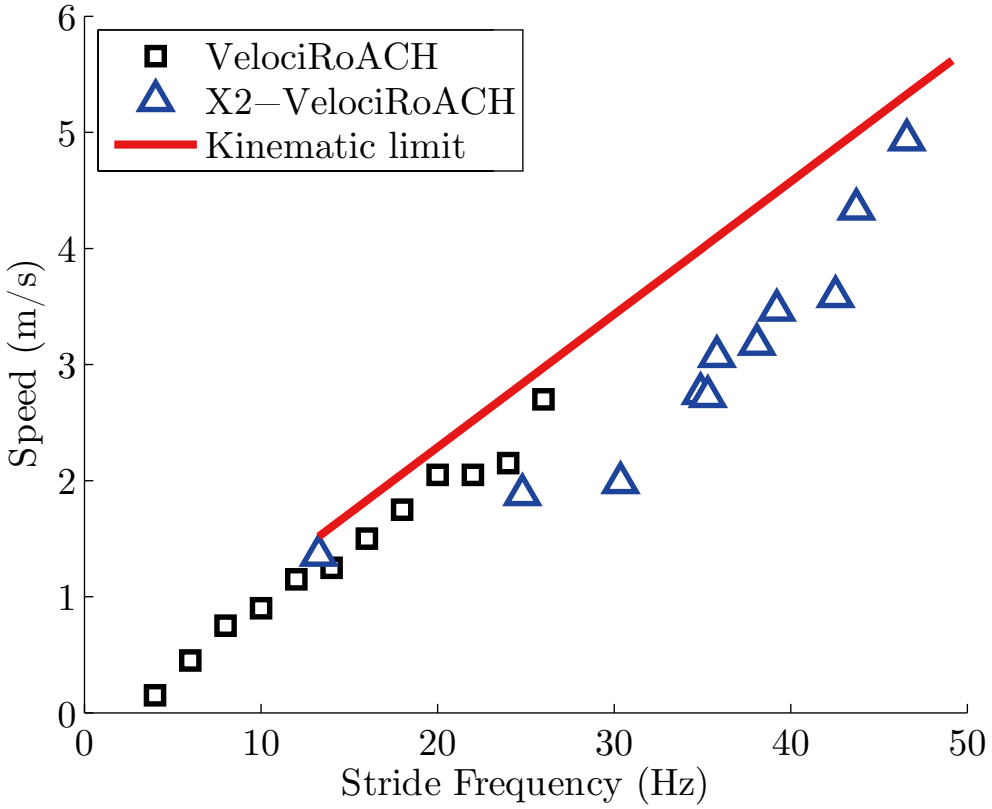

Figure 2.8: Speed as a function of stride frequency for the X2-VelociRoACH, and VelociRoACH [42]. Also shown is a kinematic upper bound on the stride frequency. Adapted from [38].

period. The sensorless speed controller drives the motor with an open-loop duty cycle, so we would expect the crank angle to lag in regions of the cycle which require positive torque input. Conversely, the crank angle is expected to lead in regions which require negative torque input. Fig.2.12 confirms these expectations, indicating that the simulation is at least somewhat valid.

Fig.2.13 shows the mechanical power the X2-VelociRoACH uses as a function of stride frequency for three different running scenarios: running on the ground, running in the air, and running in the air without legs. The mechanical power was calculated by recording electrical motor power measurements, and combining them with a model of the transmission efficiency:

$$\text{Electric power} \sim \frac{\text{Mechanical power}}{\eta} \leq \text{avg}\left(\frac{|\tau||\dot{\theta}|}{\eta}\right) \tag{2.1}$$

where η is the efficiency, τ is the motor torque, and $\dot{\theta}$ is the motor velocity.

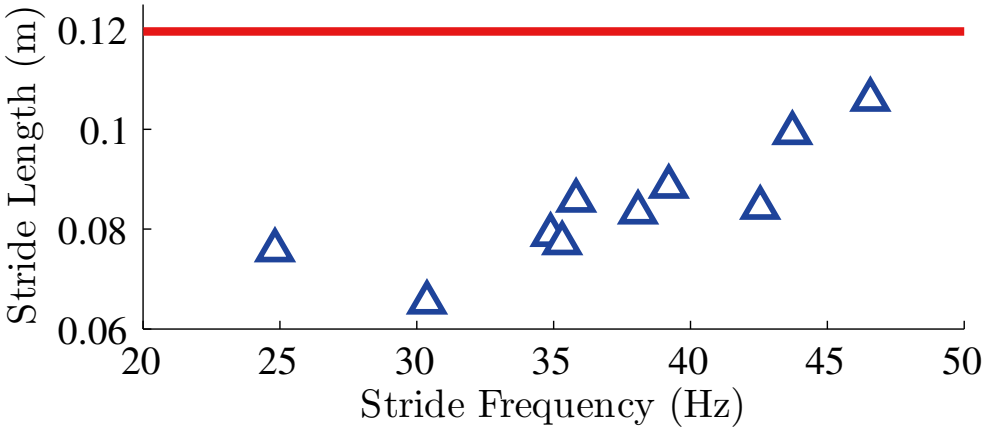

Figure 2.9: Distance traveled over a single stride (one full crank rotation), as a function of stride frequency. The red line is the distance a robot with wheels of the same radius as the nominal leg length would travel. Adapted from [38].

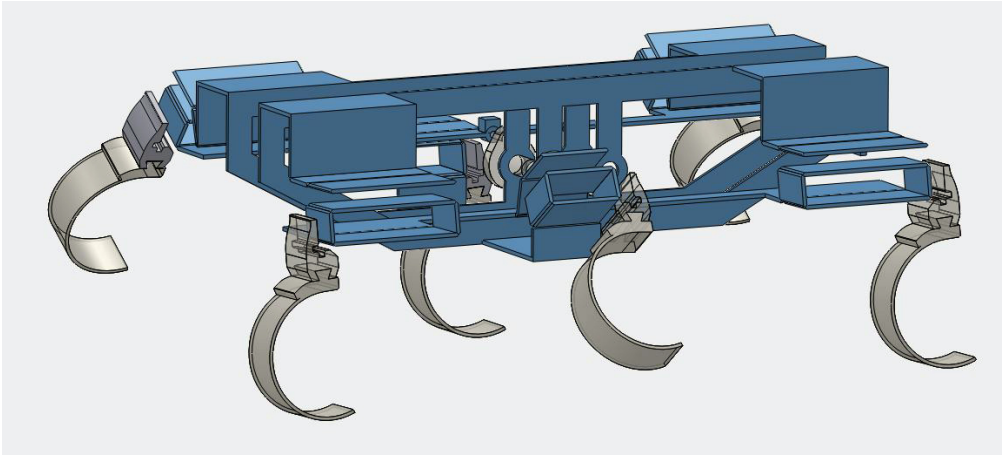

Figure 2.10: A rendering of a Solidworks model of X2-VelociRoACH. The leg mechanisms have one degree of freedom, and are driven by a single virtual motor. Adapted from [38].

The efficiency of a DC brushless motor is a direct function of its speed so we fit an efficiency model to the transmission by measuring the power input to the system for a range of known output loads and speeds. The efficiency of the combined brushless ESC/motor/transmission system peaked at 36%. The low-cost nature of the hobby components and the non-ideal properties of 3D printed gears make this low efficiency understandable.

Data collected from VelociRoACH [42] are shown as a point of comparison. Also shown on the graph is the predicted inertial power cost, which was calculated using the Solidworks model shown in Fig.2.10. This estimate is calculated by integrating the positive power requirements from the Solidworks model over a stride, and multiplying by the stride rate. This assumes that the sensorless ESC does no work to brake the motor. This consideration

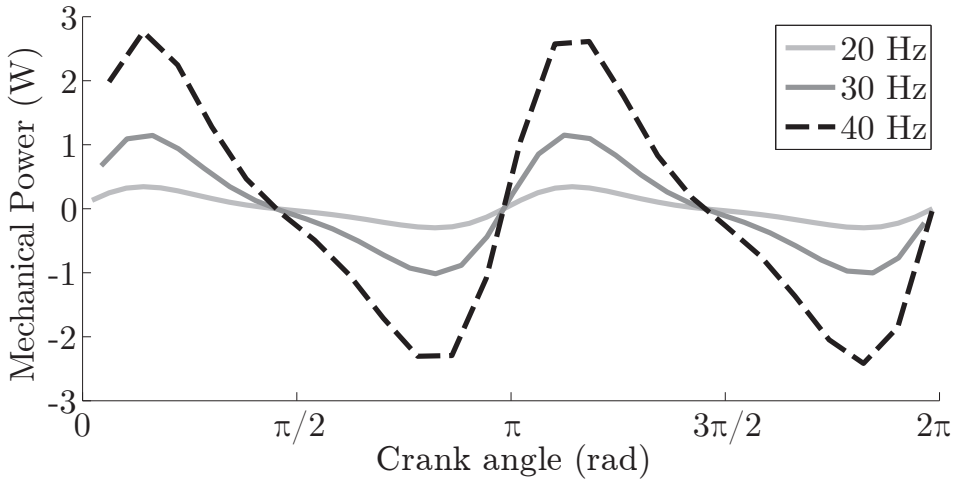

Figure 2.11: Power requirements for driving the motor at constant rates, as a function of crank angle (see Fig.2.4). The peak amplitude increases cubically with stride frequency. Adapted from [38].

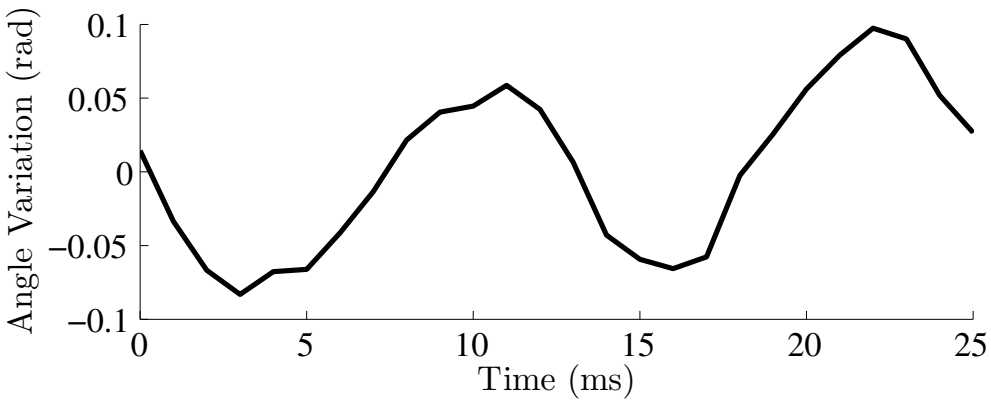

Figure 2.12: Variation of crank angle over a full rotation for one in-air stride at 40 Hz, as measured by the Hall-encoder on the motor. Adapted from [38].

is shown in the inequality in Eq. 2.1.

An upper bound for frictional dissipation is also shown. This upper bound is given by $P = \mu m g v_{\text{bnd}}$, where μ is the frictional coefficient (0.55), g is the gravitational constant, and v_{bnd} is the kinematic speed limit for a given frequency (from Fig.2.8). This bound corresponds to the robot being dragged along the ground at its maximum attainable speed. This is maximum amount of energy that could be dissipated by the legs using friction. When it is exceeded, we can be sure that power is being consumed by another source.

For the experimental data, the least power was consumed by the robot running in the air without its legs attached. The linear increase in this graph shows the power cost in running from only the transmission and kinematic mechanism. When the legs are added to the robot,

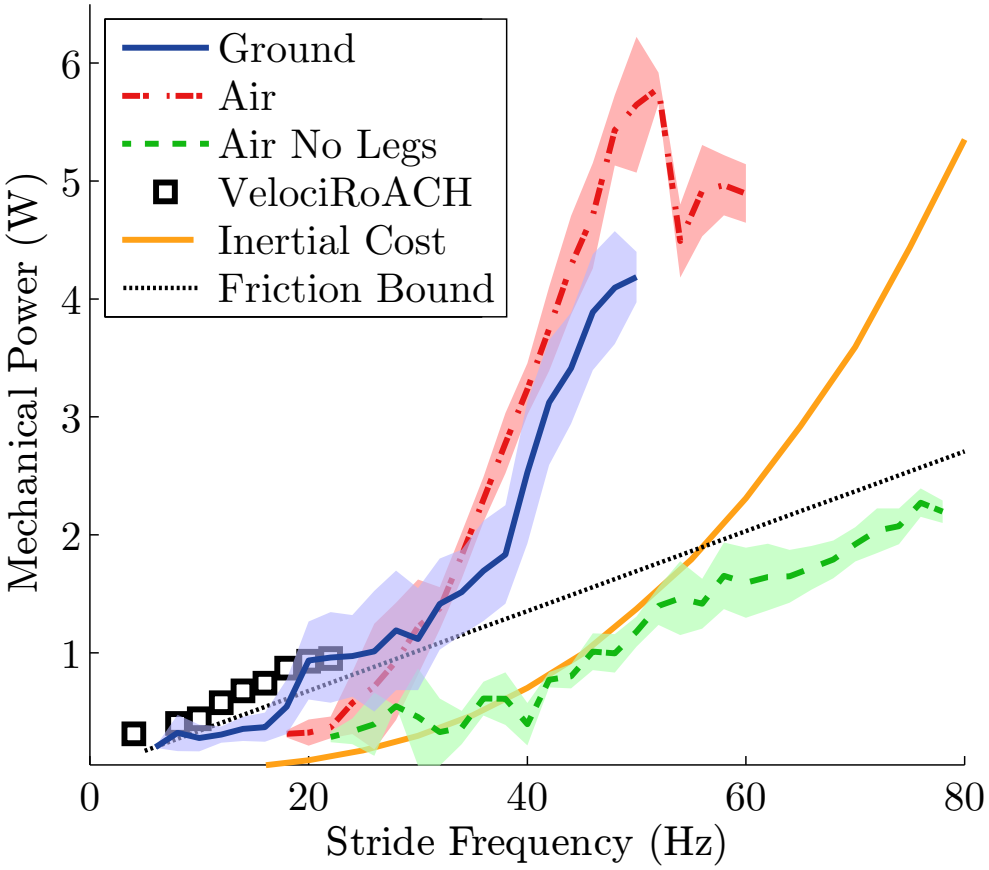

Figure 2.13: Power as a function of stride frequency for the X2-VelociRoACH for running in air, with and without legs, and running on the ground. The data are segmented by individual stride; the middle line is the average, the shaded region is one standard deviation. Adapted from [38].

the mechanical power requirement greatly increases. The power cost incurred by running on the ground is not greater than the power required to move the legs. There may be an issue with this data in that the order in which the trials were run may affect the trends. The robot was run in the air after it was run on the ground, so the accumulated damage may have caused the power draw in the air to be higher. In any case, the effect of running in the air vs. on the ground at high frequencies is less than the effect of damage that the robot accrues during high-frequency running.

Fig.2.14 shows the specific resistance of X2-VelociRoACH as a function of stride frequency. Data from VelociRoACH are provided as a reference. To allow a more direct comparison between the two platforms, the specific resistance was calculated as $S = \frac{P_m}{mgv}$ where P_m is the total *mechanical* power (as opposed to electrical power which is sometimes used instead, and is strictly larger from losses in the drive electronics), g is the gravitational

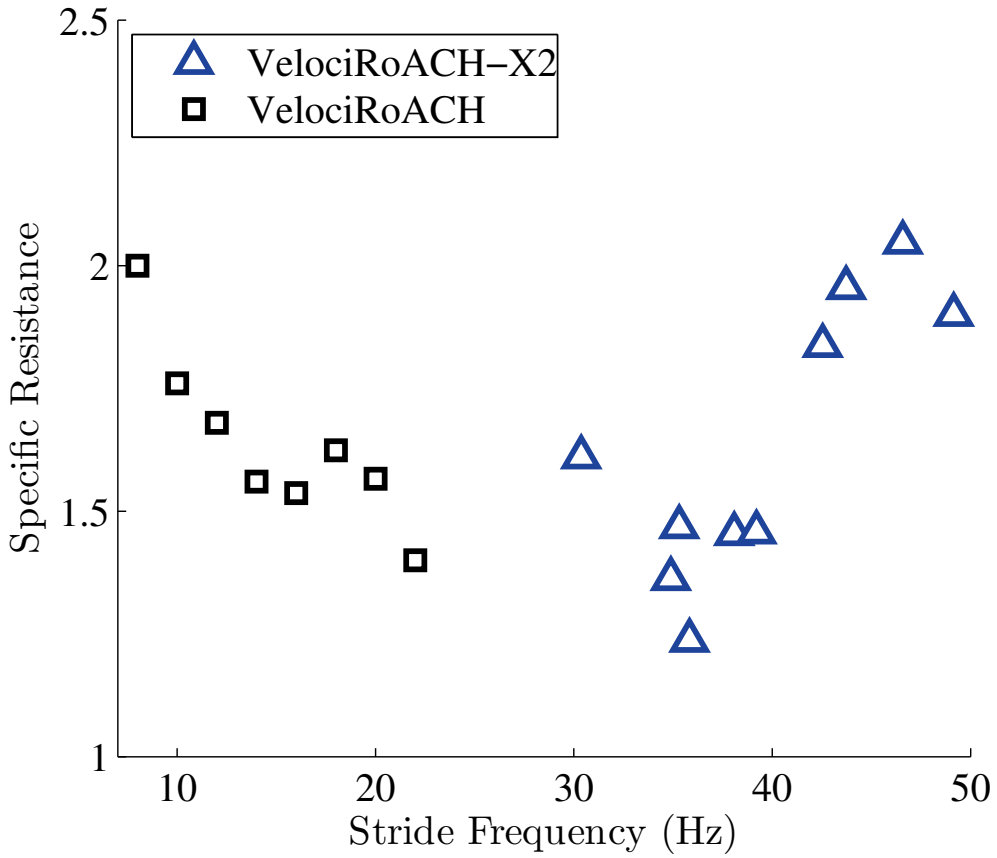

Figure 2.14: Specific resistance (calculated using mechanical power, not electrical) as a function of stride frequency for the X2-VelociRoACH, and VelociRoACH [42]. Adapted from [38].

Table 2.1: Comparison to Similar Running Robots

	X2-VelociRoACH	**VelociRoACH** [42]	**DynaRoACH** [51]	**iSprawl** [59]	**Research RHex** [97]
External Dimensions (LxWxH) (cm)	10.4 x 6.4 x 4.9	10 x 6.5 x 4.2	10 x 4.5 x 3	15.5 x 11.6 x 0.7	54 x 39 x 12
Mass (g)	54.6	29.1	23.7	300	8200
Top Speed (body-lengths/second)–(m/s)	47 (4.9)	27 (2.7)	14 (1.4)	15 (2.3)	5 (2.7)
Stride Frequency (Hz)	45	24	20	14	6
Specific Resistance (Electric power)	3.3	0.98	1.1	1.75	0.72

constant and v is the forward velocity. The specific resistance of the X2-VelociRoACH increases at its highest speeds due to the high rates of power consumption associated with high-frequency running.

2.4 Discussion

With the X2-VelociRoACH we have yet to find a fundamental speed limit for legged locomotion. The velocity increased with increased stride rate without the trend becoming sub-linear (Fig.2.8), showing that further gains in velocity can be achieved if the stride frequency can be further increased. The X2-VelociRoACH had an observed top speed of 4.9 m/s while running at 45 Hz, making it faster than the vast majority of untethered running robots in terms of absolute speed, and faster than all extant running robots in terms of relative speed (shown in Table 2.1). One limit that was encountered was one of material strength. The loads experienced by the flexures increase with the square of the stride frequency (as predicted from Solidworks Motion simulations), so accumulated damage is especially problematic for high-frequency running. Because the gain in velocity is linear, further gains in speed (which would be accomplished by increasing stride frequency) will have diminishing returns in terms of platform survivability.

During high-frequency locomotion, the power draw of the X2-VelociRoACH is dominated by the inertial cost of recirculating the running appendages. When running above 20 Hz, the robot draws more power than the legs would be able to dissipate by any frictional interaction. We can see this inertial cost in the sharp increase in the power required for locomotion at high-speeds. When the robot is run in the air with its legs attached, it has a similar power draw to the robot running on the ground. More data collected in a properly randomized experimental trial would further elucidate these trends. The real power required to drive the legs at a constant speed (in the absence of friction) is zero, as shown by Fig.2.11. The X2-VelociRoACH has no means of storing and returning the energy fluctuations from inertial effects but if greater efficiency was desired, a flywheel or spring [9] could be added to the robot to reduce the robot's power consumption at high stride rates. This design adjustment would not mitigate the high loads applied to the flexures so a further increase in maximum speed is not expected, given the strength limits of current materials.

The large increase in power cost at high stride frequencies led to an interesting trend in the overall specific resistance of the robot. The specific resistance[6] of legged invertebrate locomotion is monotonically decreasing [33] with stride frequency. This trend is also shown in the VelociRoACH data. The fact that the specific resistance of the X2-VelociRoACH increases at its highest attainable (and furthest removed from the bio-inspired regime) stride frequencies is an important point. Locomotion at these unnaturally high frequencies is less efficient than an intermediate speed. Increasing the velocity with higher stride rates is possible, but it comes with a considerable cost in power and efficiency.

[6]Cost of Transport is reported in [33]. Specific resistance is cost of transport normalized by the gravitational constant.

2.5 Conclusion

An interesting question for legged robotics is where the limits to maximal speed running come from. Most running animals prefer to run near their maximum stride frequency and increase their velocity by increasing their stride length. In this work we have shown an alternative strategy of simply increasing the stride frequency to increase velocity. This simple strategy can be readily used by biomimetic millirobots, whereas increasing stride length would require a higher degree of articulation than is available on these underactuated platforms. An alternative to a higher degree of articulation are passively extensible legs which could exaggerate the trend seen in Fig. 2.9.

With the X2-VelociRoACH we have increased the stride frequency of a legged robotic platform far beyond what an animal of equivalent size would use. This platform runs at a higher stride frequency than any other extant legged robot. The top speed of 4.9 m/s was observed at 45 Hz, the highest frequency the robot could use without losing appendages. This robot runs at a higher Froude number than any other, 11.3. The power-density-first design strategy enabled the increased speed of this robot. The current limitation on the maximum speed of the X2-VelociRoACH is therefore one of material strength. Due to the choice of actuation scheme the minimum speed for stable running was 2.75 m/s, which makes the X2-VelociRoACH a highly specialized runner. Position based control of the brushless motor would improve the performance of this robot at low speeds.

We investigated the energetic costs associated with high-frequency running. The power demand increases greatly at high stride frequencies due to the rapidly cycling the running appendages. This causes the specific resistance of the platform to increase at its highest attainable speeds. This trend is uncommon to animal locomotion, because animals increase stride length instead of stride frequency [32].

While using stride frequencies far removed from the bio-inspired regime, the power consumption of the X2-VelociRoACH is dominated by inertial forces. The gain in velocity with stride frequency is linear, whereas the power costs increase cubically. These diminishing gains in velocity motivate other strategies for increasing the speed of the platform.

Chapter 3

Agile Locomotion

3.1 Introduction

We also apply the power-density-first design methodology to create a jumping robot. Our goal is to create a platform capable of highly energetic locomotion: agile gaits characterized by repeated high-amplitude jumps.

Agility Metric

To establish how our design approach facilitates agile locomotion, we anchor the study with an agility metric. Our goal for this metric is that it is defined for both animal and robotic systems and is simple to calculate from purely extrinsic measures (i.e., requires no invasive measurements of muscle force or power). We define vertical jumping agility to be the height that a system can reach with a single jump in Earth gravity, multiplied by the frequency at which that jump can be made. Vertical jumping agility is then equal to

$$\frac{h}{t_{\text{stance}} + t_{\text{apogee}}} \tag{3.1}$$

where h is the jump height, t_{stance} is the total stance time from the onset of actuation, and t_{apogee} is the flight time from when the jumper leaves the ground until the apogee of a jump (when the vertical velocity is zero). This metric can be ascertained from a video of a maximal jump, satisfying the goal of definition by extrinsic measure. This metric is an extension of previous work defining vertical agility as the product of the gravitational constant and the maximum jumping height [31]. By considering the rate at which platforms can jump, we can more clearly differentiate between systems. Because jumps terminate with zero vertical velocity, a ballistic limit

$$h \leq \frac{g}{2\omega^2} \tag{3.2}$$

where h is the jump height, ω is the jump frequency, and g is the gravitational constant is determined when the stance time drops to zero and the platform spends all its time in flight. Other forms of vertical locomotion such as climbing, running uphill, or flapping flight can be described with a vertical agility metric but are not subject to the ballistic limit because the vertical velocity does not reach zero before another cycle occurs.

Vertical jumping agility is measured in vertical meters per second, corresponding to the average vertical speed that a system can attain with repeated jumps (or how quickly a predator would have to chase an animal leaping from branch to branch up a tree). Because it is defined as a climb rate in a gravitational environment, the vertical jumping agility of any system is limited to its power-to-weight ratio. This metric is a dimensional quantity because the jump heights and distances imposed by the environment do not vary with platform size. If locomotion over adverse terrain requires a vertical jump of 1 m, then a 1-m jump is required, regardless of system mass. Vertical jumping agility describes how much and how quickly an animal can change its energetic state; it does not consider planar changes of direction or turning behaviors, which have been addressed by previous work [45]. The interplay of jump frequency and height gain is shown in Fig. 3.1 for three robots using different actuation strategies, as well as the most vertically agile animal for which data were found (*Galago senegalensis*, the lesser galago). This figure shows a series of repeated vertical jumps for each system over an interval of 4.0 s, the time required for one full wind-and-jump cycle by the EPFL Jumper [62]. Over this time interval, the EPFL Jumper jumps once to attain a height of 1.3 m; the more agile galago jumps five times to a height of 8.5 m.

In nature, vertical jumping agility is important for predator-prey interactions, which drive the evolution of specialized performance in both participants [71]. The choice of prey escape tactic frequently depends on the environment: Anoles encountered at ground level escape by running, whereas those in shrubs prefer to jump [64]; saxicolous species of snow skinks use jumping; the arboreal species almost invariably climb [70]; and black-tailed deer stot more frequently when surprised in high vegetation [90]. The jumping ability of prey animals determines hunting tactics in jumping spiders [11], and the vertical jumps of caracals allow them to prey upon birds in flight [89]. The vertical jumping agility of a prey animal may mediate its success when vertically escaping pursuit; any prey animal escaping upward with multiple jumps (or by climbing) will escape its predator if it has a greater vertical jumping agility. Vertical jumping agility could be a contributor to evolutionary fitness, resulting in model animal systems that can guide the creation of more vertically agile robots. Furthermore, the creation of vertically agile robots may provide biologically relevant insights into animal locomotion. Fig. 3.2 shows the height gain and jump frequency (defined for a single jump), for a range of animal and robotic systems, as well as hyperbolae of constant vertical jumping agility and the aforementioned ballistic limit of jumping locomotion. All the constant agility curves intersect the ballistic limit, indicating that the highest agilities can only be realized by increasing jump height. The highest observed vertical jumping agility was 2.2 m/s from the galago. The robot developed in this work has an agility of 1.75 m/s, which is higher than that of the previously most agile robot, 1.12 m/s (Minitaur [58]). We will refer to this chart while assessing how the choice of actuation topology has affected

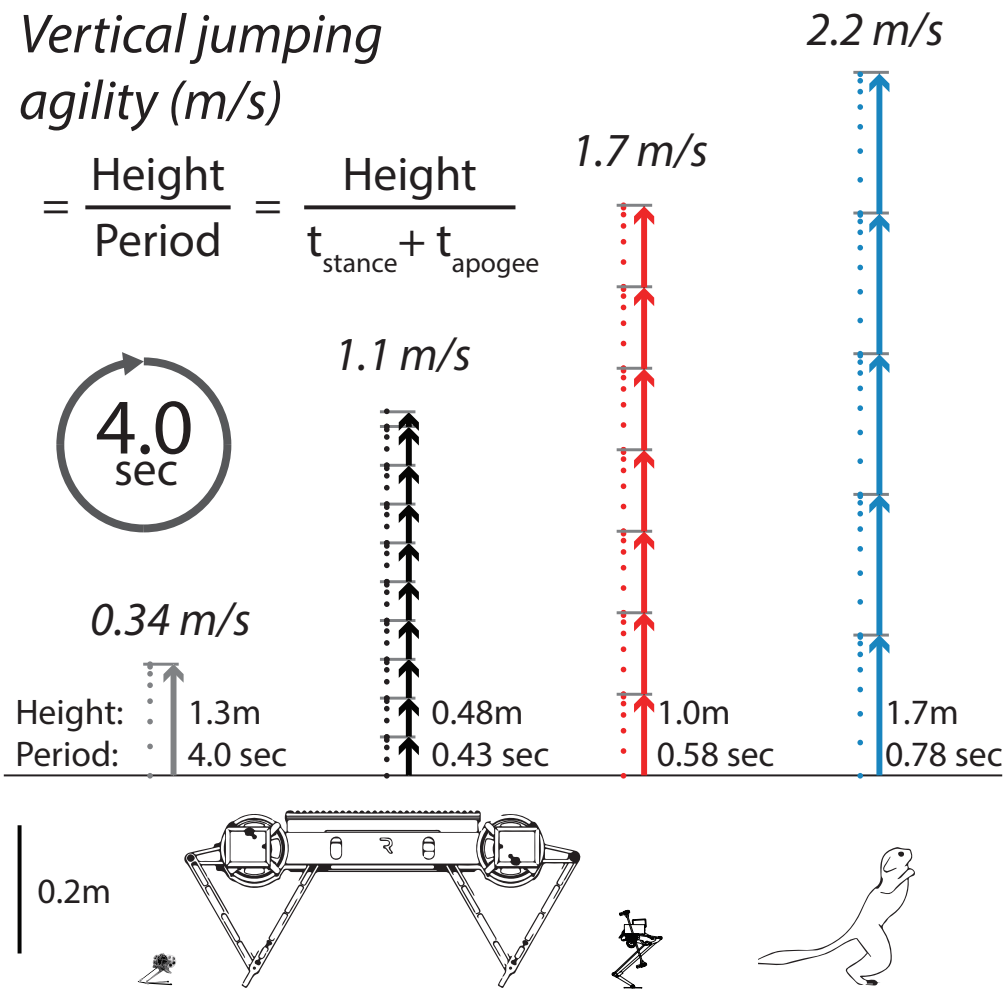

Figure 3.1: Four seconds of agile jumping. (Left to right) A series of jumps for the most agile systems for various actuation strategies: parallel-elastic(EPFLJumper), rigid (Minitaur), series-elastic power-modulating (this work), and animal (G. senegalensis). Each arrow represents one jump; the jump period and height gain are shown next to each series. Adapted from [43].

vertical jumping agility in robotic systems.

Power modulation is an adaptation found in natural systems (and designed into some robotic systems) that increases the peak power available for jumping. Known as power amplification in the biomechanics literature (a misnomer [84]), power modulation occurs whenever the instantaneous power developed by a muscle-tendon complex exceeds the maximum available from the muscle alone [84]. It has been observed across diverse phylogenetic lines in chameleons [37], salamanders [27], pipefish [94], and mantis shrimp [77], and its role has been studied to explain the performance of jumping animals [48] [69] [2] [7] . During a power-modulating behavior, muscles transfer energy into series-elastic or parallel-elastic

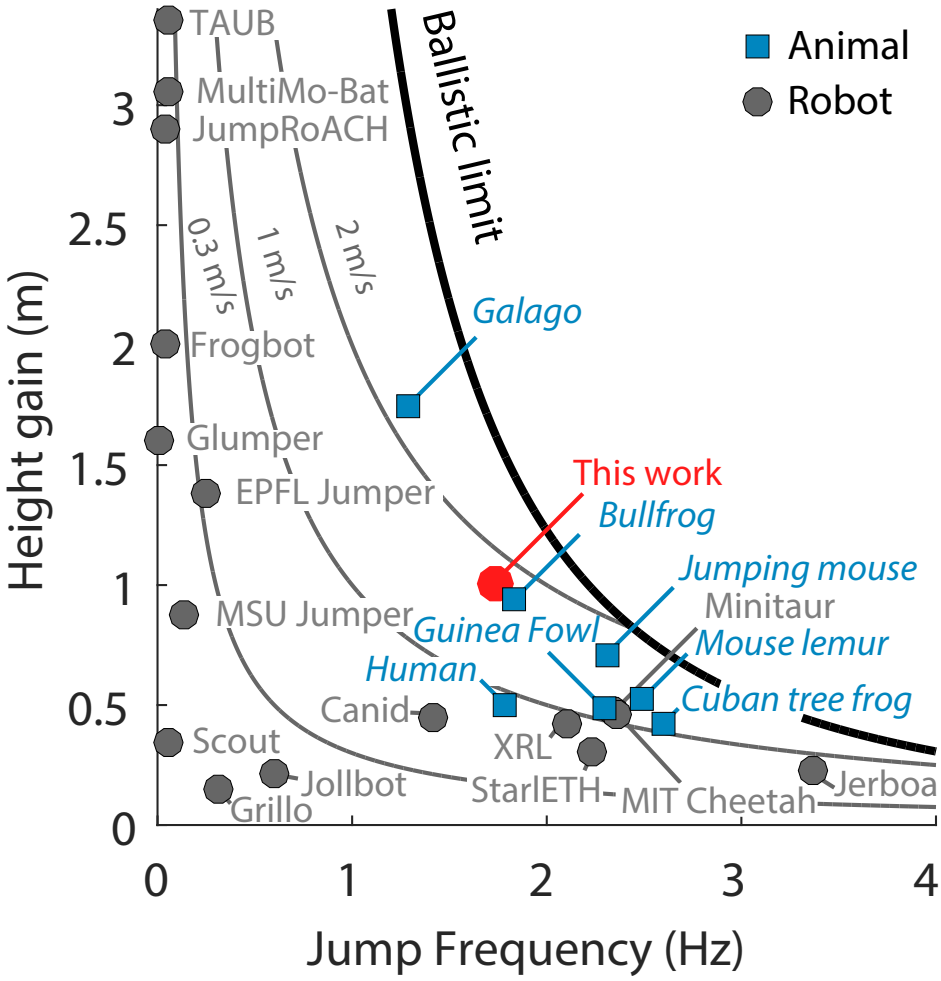

Figure 3.2: Height gain and jump frequency for animal and battery-powered robotic systems. The ballistic limit for jumping and hyperbolae defining constant agility for 0.3, 1, and 2 m/s are also shown. Animal species: *G. senegalensis* (galago [2]), *Rana catesbeiana* (bullfrog [7]), *Zapus trinotatus* (jumping mouse [44]), *Microcebus murinus* (mouse lemur [65]), *Osteopilus septentrionalis* (Cuban tree frog [69]), *Numida meleagris* (guinea fowl [48]), and *Homo sapiens* (human [18]). Data from explosion-powered robots [98] are not shown. Adapted from [43].

structures and then release that stored energy at power levels greater than what the muscle alone can produce. The arrangement of elastic structures determines how power flows from the actuators and how stored potential energy is converted into kinetic energy.

A robotic jumper can use a rigid actuation strategy, with no substantial compliance between the actuators and the environment. Minitaur [58] and the MIT Cheetah [75] have leveraged the fact that electromagnetic actuators scale favorably with size [88] and use rigid, torque-dense actuators. These systems have similar vertical jumping agility and can jump at

rates greater than 2Hz; the more agile of the two (Minitaur) has 54% greater power density than estimates made for the galago [2], but half the vertical jumping agility. All of the animal systems in Fig. 3.2 have nonnegligible compliance in the muscle-tendon complexes that power their jumps. This compliance enables power modulation and allows them to attain greater vertical jumping agility than robotic jumpers of greater power density. Several robots have incorporated compliant elements (for a survey, see [95]); the robots with nonrigid actuators in Fig. 3.2 use either parallel-elastic or series-elastic elements.

A parallel-elastic robot has a compliant element attached in parallel with the leg structure, coupling leg extension to energetic state. The disadvantages of this approach are that the position of the leg cannot be changed without doing energetic work and that collision losses are increased [100] (should the actuator not be decoupled). As opposed to series-elastic robots, parallel-elastic robots can work to increase their energetic state while airborne, and energy storage is only limited by maximum actuator force and strain energy storage density. Small jumping robots [62, 23, 104, 91, 6, 67, 93] (inspired by insects using a similar strategy, i.e., [92]) use a high-force, low-speed actuator to wind a parallel-elastic leg mechanism (sometimes over a number of minutes) and then decouple the motor, allowing the stored energy to be returned rapidly. This design choice resulted in the highest robotic jumps, but none of the parallel-elastic robots attained a vertical jumping agility greater than 0.34 m/s, with most populating the region near the vertical axis in Fig. 3.2. The choice of decoupling the actuator to enable rapid energy release means that these parallel-elastic jumpers cannot control power release within a given jump. Previous work with the bow-leg hopper [102] has shown that this can be sufficient to control a monoped that has low step-to-step energetic variation.

A series-elastic robot interposes a spring element between a rigid actuator and the environment. This reduces the impedance of the jumping appendage, safeguards a potentially fragile actuator, allows force controllability and passive energy recovery, and enables power modulation [35, 74] without coupling leg position to energetic state. Robots using series-elastic actuators [55, 19, 36, 46] have a greater vertical jumping agility than all of the parallel-elastic systems but less than the rigidly actuated Minitaur and MIT Cheetah. An adaptation has been found in animals adapted for saltatorial locomotion that increases the peak power output of a series-elastic actuator, which could increase robotic vertical jumping agility.

Previous work has shown that a mechanical advantage (MA) adaptation can increase the energy that a series-elastic muscle-tendon complex can deliver [83]. MA is defined here as the ratio between the reaction force at the foot to the force applied by the actuator. A low MA means that the muscle can apply a high force (which stores energy in the elastic tendon), with low ground contact force, preventing the large upward acceleration that would otherwise result. Animals with pronounced degrees of power modulation have an MA profile that starts low to store energy and then increases throughout the stroke, rapidly releasing energy for high-power jumps [83]. The magnitude of this effect is shown by the galago, whose jump requires 15 times more power than its muscles alone produce [2]. A robotic series-elastic actuator with an MA adaptation (SE+MA) would use a series-elastic actuator

Table 3.1: Jumping Energy Delivery Mechanisms

Mechanism	**Robots** (*agility* (m/s))	**Animals** (*agility* (m/s))
Stiff connection	**1.12** [58], 1.07 [76] , 0.36 [17]	–
Catch mechanism	**0.34** [62], 0.065 [23] 0.045 [87] 0.13, 0.0037 [6], 0.12 [105] 0.042 [72], 0.019 [91] 0.10 [56] 0.16 [101] 0.19 [99]	**0.64** [92]
Series Elastic	**0.89** [55], 0.67 [36] 0.64 [46], 0.77 [19]	0.89 [18], **1.1** [48]
Power modulation	*This work* **2.8** (Predicted)	**2.2** [2] , 1.1 [69] 1.6 [44], 1.7 [7]

to drive a limb with an MA profile designed to increase the energy delivered over the stroke, more than what would be otherwise realizable. This strategy preserves the benefits of a series-elastic actuator, which are well-matched to the task of agile locomotion.

The data from Fig. 3.2 are also presented in Table 3.1, sectioned by the mechanical strategy used to transfer energy from actuators to the center of mass. The agility for each system is presented as well. The data in this table do not constitute a complete review of all systems.

Any robot that drives a leg with nontrivial kinematics using a series-elastic actuator (such as the proposed Skippy [30]) is capable of power-modulating behavior. However, to the authors knowledge, a treatment involving designing the MA profile of a limb to increase the energy that it can deliver and experimental evidence of the efficacy of this approach have yet to be presented. We seek an understanding of how the fundamental choice of actuation strategy and power-density affects vertical jumping agility and engineering methods by which an SE+MA actuator can be instantiated in a physical prototype. We also seek to explore vertical jumping agility enabled behaviors using a robotic prototype with an SE+MA appendage, Salto (Expansion: Saltatorial Locomotion on Terrain Obstacles).

Design study

We first explored the interplay between actuation strategy and vertical jumping agility using a model of an SE+MA system that is shown in Fig. 3.3 A. Here, a mass (M) was driven by a series-elastic actuator composed of a linear motor (force: $F = F_{\max} - \frac{VF_{\max}}{V_{\max}}$, where

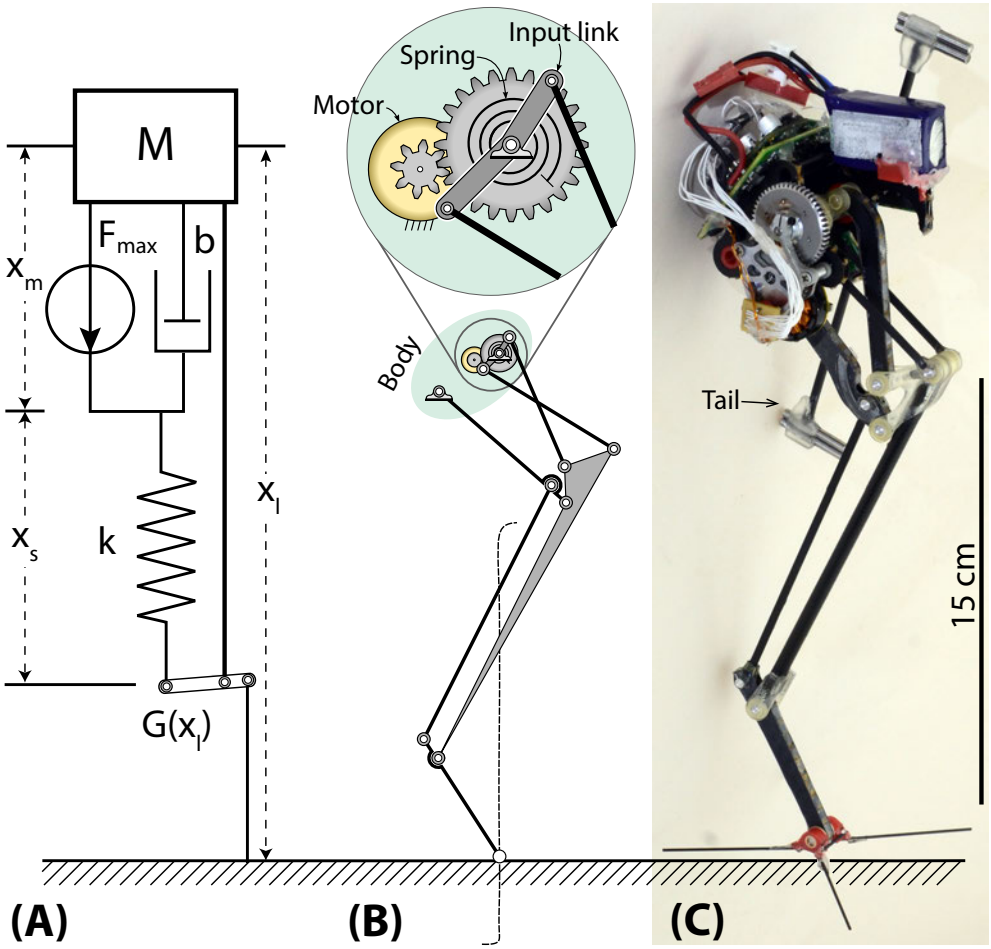

Figure 3.3: Power modulation modeled and instantiated. (A) Model of a power-modulating system with a series-elastic actuator and an MA element. (B) Linkage schematic for the robotic mechanism. (C) Photograph of an integrated robotic platform, Salto. Adapted from [43].

V is actuator velocity) and a linear spring of stiffness k that applied force to the ground through a transmission with an MA ($G(x_l)$) that is a function of leg extension. We created a robotic platform (Salto) to experimentally evaluate power modulation. Figure 3.3 B shows a diagram of a linkage synthesized to instantiate an SE+MA MA profile. Salto, shown in Fig. 3.3 C, was used to perform experiments including vertical jumps and a wall jump maneuver.

All current robots fall short of the galagos vertical jumping agility. The following design study explains this shortfall by evaluating the power density (peak mechanical power per unit mass) that robotic systems would require to match the galagos performance. The mass and leg extension have been fixed to that of the galago (0.25 kg and 0.15 m, respectively), and we explored the choice of rigid, parallel-elastic, series-elastic, and SE+MA actuators for two different power densities. The rigid and parallel-elastic actuators have been idealized as

constant power motors, thus including robotic designs with specialized transmissions (like Grillo [87]). Our prototype will not have a specialized transmission; to closer match reality, the series-elastic and SE+MA designs use the previously presented linear motor model. The SE+MA MA function that we explored was piecewise constant, starting leg extension with a low MA to store energy and ending with a high MA to return it. This adaptation is parameterized by G_R, the ratio of ending MA to starting MA.

Fig. 3.4 shows rigid, parallel-elastic, series-elastic, and SE+MA jumpers for power densities of 10 and 100 W/kg, in the vertical jumping agility metric space. Along each curve are points that correspond to various values of G_R; the series-elastic design without an MA adaptation occurs at $G_R = 1$. The series-elastic and SE+MA designs in Fig. 3.4 were determined by specifying mass, leg extension, power density, and the MA ratio and optimizing for agility over F_{max} , G_{store} , spring stiffness k, and transition point. The rigid case was solved analytically. A galago has a power density of about 93 W/kg [2]. Fig. 3.4 shows that the highest jump for a galago (100W/kg) with ideal rigid actuators would only be 0.68m, a 60% reduction in height, with a vertical jumping agility of only 1.8 m/s.

Both series-elastic and SE+MA systems can jump higher than a rigid jumper of the same power density. The actuator delivers energy to the elastic element instead of directly accelerating the body; this extends stance time and thus the net energy delivered [35, 74]. The energy in the elastic element can be returned without power limit, and SE+MA designs converged to a limit wherein the starting MA was low enough that gravity prevented extension of the leg until a large amount of energy was stored and the ending MA rapidly returned the energy. Increasing the MA ratio increased the jump height for SE+MA systems. The vertical jumping agility for the 10-W/kg case does not increase substantially with this gain in jump height, which is fundamentally limited to a vertical jumping agility of 1.0m/s ($10\text{W}/((1\text{kg})9.81ms^2)$), the equivalent constant-speed elevator limit. The 100-W/kg system sees substantial gains in agility as the MA ratio is increased; the SE+MA actuator allows more energy to be delivered. The agility curve associated with this power density lies outside the bounds of Fig. 3.4.

The hypothetical parallel-elastic jumper continuously applies constant power, winding in the air and in stance (similar to Grillo [87] and the bow-leg hopper [20]), and returns that power as an impulse. This jumper would operate along the ballistic limit until the intersection with the vertical agility curve defined by that jumpers power-to-weight ratio and then trace that constant vertical agility curve. Physically, this corresponds to jumping with zero stance times until hitting the power-to-weight limit and then increasing jump height by increasing stance time. The 10-W/kg parallel-elastic robot in Fig. 3.4 would operate along the curve of agility=1m/s, with the intersection point with the ballistic limit beyond the extent of the graph. The 10-W/kg power-modulating jumper asymptotically approaches this limit. The galago's vertical jumping agility could be attained by the constant-power wind-up jumper with a power density of only 21.9W/kg. However, this achievement implies that force can only be applied as an impulse, whereas the other actuation strategies retain the capacity to control force. We can design a hypothetical robotic galago for each actuation strategy. For this robot, the jump height, mass, and leg extension match data inferred for a

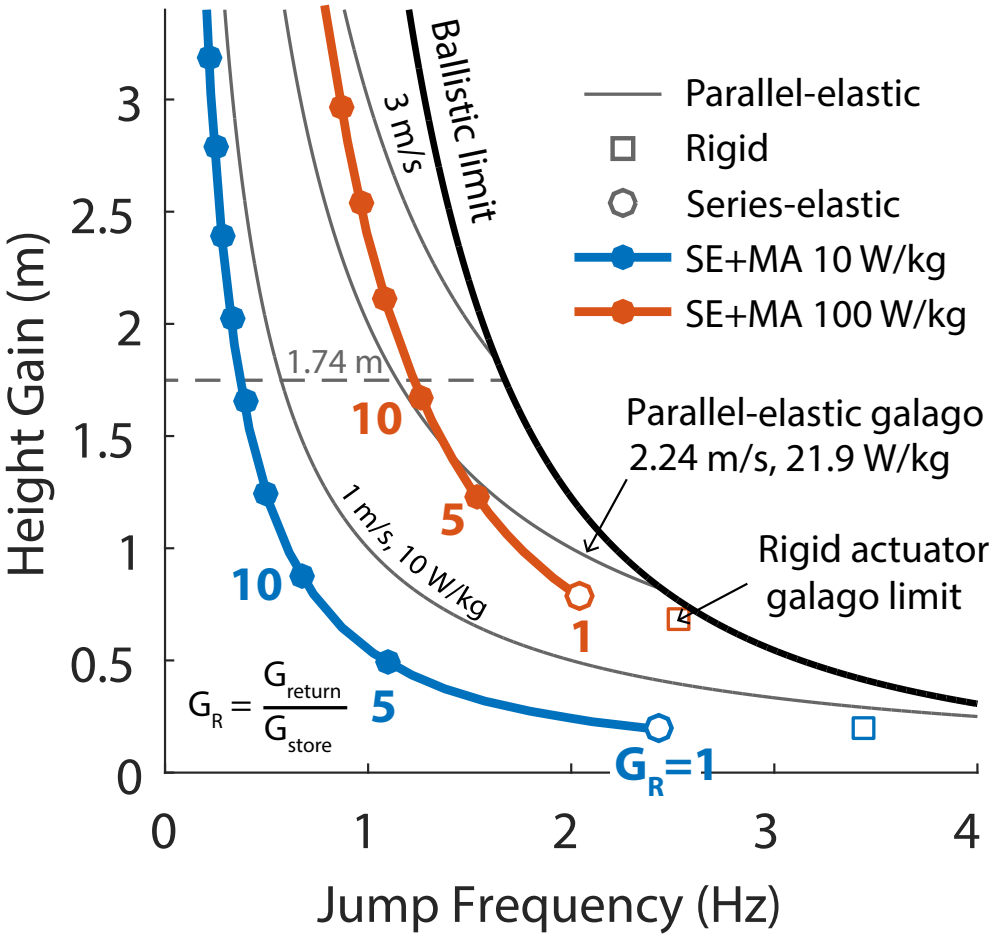

Figure 3.4: The effect of actuation on vertical jumping agility. Design points for rigid, parallel-elastic, series-elastic, and SE+MA jumpers for a galago-scale robot (mass, 0.25 kg; leg extension, 0.15 m) are shown. Dots correspond to locations of MA ratio $G_R = 1$, 5, 10, 15, etc. Adapted from [43].

galago [2]. If there are sufficient parameters, the vertical jumping agility matches that of the galago; otherwise, the vertical jumping agility is left unconstrained. Given these constraints, we then determine the minimum power density requisite for the jump, specifying that the system starts with zero energy.

The result of the design study is shown in Table 3.2, with data from the galago and experimental results from Salto. The rigid and basic series-elastic systems needed the highest power densities to match the jump height of the galago. The higher power densities of these systems resulted in lower stance times for the jumps (as compared with SE+MA), resultingin higher vertical jumping agility. The series-elastic system required a lower power density than the rigidly actuated system, because the spring enabled power modulation, as has been previously observed [35, 74]; the parallel-elastic robot needed a much lower power.

Table 3.2: Actuation strategies for designing a hypothetical robotic galago.

	Galago	Hypothetical rigid	Hypothetical series-elastic	Hypothetical parallel-elastic	Hypothetical SE+MA	EPFL Jumper	Salto
Mass (kg)	0.25	0.25	0.25	0.25	0.25	0.007	0.100
Leg Length (m)	0.15	0.15	0.15	0.15	0.15	0.10	0.150
Maximum jump height (m)	1.74	1.74	1.74	1.74	1.74	1.38	1.008
Jump Frequency (Hz)	1.29	1.66	1.59	1.29	1.29	0.248	1.74
Vertical jumping agility (m/s)	2.24	2.89	2.78	2.24	2.24	0.34	1.75
Power density (W/kg)	92.7	343	325	21.9	90.0	50	137

No parallel-elastic robot has attained this performance; thus, we present data from the most vertically agile parallel elastic robot (EPFL Jumper) for comparison. The hypothetical SE+MA robot has the lowest required power density of the actuation strategies that do not preclude force controllability, falling close to an estimate of galago power density by Aerts [2]. The rigid and series-elastic cases are strict subsets of the SE+MA system; hence, it is expected that the SE+MA system would do at least as well. However, the degree of improvement is substantial; it requires 3.8 times less power density than the rigid actuator and 3.6 times less power density than the optimized series-elastic actuator without an MA adaptation. The series arrangement of the actuator allows it to apply power through the stance phase.

The minimum power density values in Table 3.2 were determined using a grid search subject to the maximum leg extension constraint and minimum takeoff velocity for the galagos jump height. The rigid jumper was parameterized by its power; all other jumpers were parameterized by linear motor parameters F_{max} and V_{max} . The series-elastic jumper had a spring stiffness, and the SE+MA jumper had both spring stiffness and MA profile. Each parameter set was simulated in Earth gravity starting from rest and zero displacement. The parallel-elastic system was solved analytically.

3.2 SE+MA Prototype development

In this section we describe design methods used to create a robotic leg which uses the power modulation strategy. Our goal was to create a lightweight and robust device which satisfies all design specifications. The final appendage is a singly actuated one degree of freedom eight-bar linkage which uses only revolute joints. The physical prototype of the mechanism can be seen in Figs. 3.7c and 3.9.

Simulation

We use a dynamic simulation to evaluate the properties of our designed linkages. We determine Newton's equations of motion by describing linkages as trees of bodies connected by pin joints. Root bodies retain their full six translational and rotational states while child body states are simplified to joint coordinates. Loop-closure constraints are applied to handle closed kinematic chains. Ground contact is modeled as an asymmetric spring-damper

with a spring constant of 10^4 N/m and damping coefficient 50 Ns/m. Horizontal friction is modelled as approximate stick-slip friction with a coefficient of static friction of 0.5.

Our actuator model is a linear DC motor (with inertia and back EMF), driven by a voltage and current-limited input. The actuator model is characterized by the motor free-running speed, torque constant, and stall current at the peak supply voltage as well as the thermally limited maximum input current.

Friction is modeled as a resistive torque applied between the crank and the body. We matched friction parameters in the simulation to experimental measurements taken after construction of the device. Observations of dry friction torque were described by the relation:

$$\tau_F = C_1 \tau_{sp} + C_2$$

where τ_{sp} is the applied torque, $C_1 = 0.045$ and $C_2 = 0.015$Nm.

Linkage Synthesis

To design a power modulating mechanism, we investigated the space of planar linkages with only revolute joints. Sliders, cams, and gears were avoided to save weight and complexity. We seek to determine the simplest linkage topology which can satisfy all constraints while leaving the design space open for optimization. All four-bar linkages which generate straight line motion have pivots (joints between links in mechanism) in inconvenient locations [73], and few free design parameters. We therefore expanded consideration to single degree-of-freedom six-bar linkages.

We used a design procedure [79] that fully explores the space of Stephenson path generating linkages, providing hundreds of candidate linkage designs that serve as an atlas of useful start points for an optimization procedure.

From this atlas, we selected the design shown in Fig. 3.5(a) which produces straight line motion with compact geometry and an input crank that rotates 217°. To specify MA, a gradient descent optimization scheme was formulated to coordinate the input angle ψ to toe height y. The low MA required for power modulation is shown as the *Energy storage phase* in Fig. 3.6. For the rest of the stroke, we elected to specify a constant ground reaction force to avoid damage-causing impulsive acceleration profiles [6]. The average value of this portion of the stroke ensures that all stored energy is returned.

To compute the MA profile for constant force, we consider three configuration variables: the angle of the motor shaft, the angle of the input crank ψ, and the foot travel y. To simplify calculations, we consider a mean scenario where the motor holds an angle of ψ_{eq} for all time, the crank rotates from $\psi_{\max}$ to ψ_{eq}, and the foot translates from y_0 over a distance Δy. The input-output function is $\psi = g(y)$ of which its derivative with respect to y i.e. $g'(y)$ is identically MA. We require $g'(y)$ such that it multiplies by an unwinding spring torque to produce a constant output force F,

$$-k\big(g(y) - \psi_{\text{eq}}\big)g'(y) = F, \tag{3.3}$$

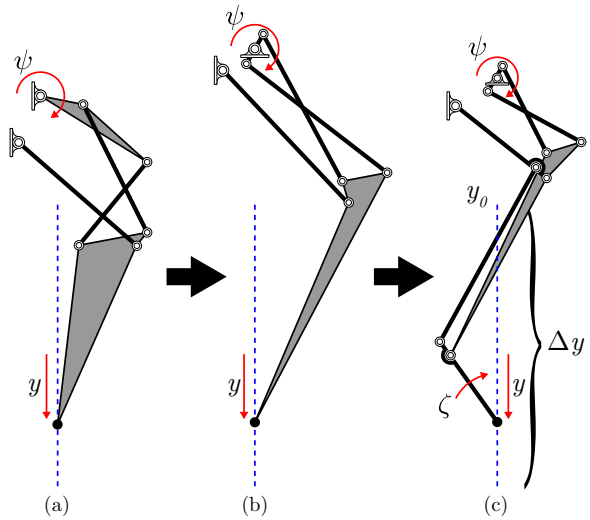

Figure 3.5: (a) An initial exploration of linkage designs focused on generating a straight line along distance y. (b) Six-bar optimization allowed specification of MA by coordinating y and ψ. (c) Eight-bar optimization added momentum balancing by coordinating y, ψ, and ζ. Adapted from [41].

with k as stiffness. The solution to this ordinary differential equation is

$$g(y) = (\psi_{\max} - \psi_{\text{eq}}) \sqrt{1 - \frac{y - y_0}{\Delta y}} + \psi_{\text{eq}}. \tag{3.4}$$

MA is shown in Fig. 3.6 as the target curve.

In addition to having the capacity for power modulation, we also specify that the jumping appendage generates no body rotation when jumping, or while extending the leg in the air. This decouples control of the body's angular momentum from motion of the leg and allows a smaller reorientation actuator to control rotation through a mechanism like an inertial tail. This strategy is in contrast to approaches that control both launch energy and angular momentum with one actuator, as the proposed Skipper robot does [30].

Previous work has addressed rotation minimization by optimizing the parameters of a four-bar leg such that the angular impulse generated during a single jump was minimized [72]. This approach is not extensible to a jumping appendage that performs a range of agile maneuvers. If the leg lifts off early, or at a different velocity the net angular impulse may not be zero. For our jumper, each 1% of launch energy (assuming a 1 joule jump) that bleeds into rotational kinetic energy produces 12 rad/s of angular velocity, making landings difficult. We therefore seek to define a set of conditions such that no angular impulse is generated by the jumping mechanism.

The fundamental constraint is that the ground reaction force generated by the mechanism always passes through the center of mass of the system. This behavior may be specified in a number of ways; we select the trivial case wherein the foot travels in a straight line. This line passes through the center of gravity of the body the leg is attached to, and the center of gravity of the moving jumping mechanism also falls on this line. To further decouple the

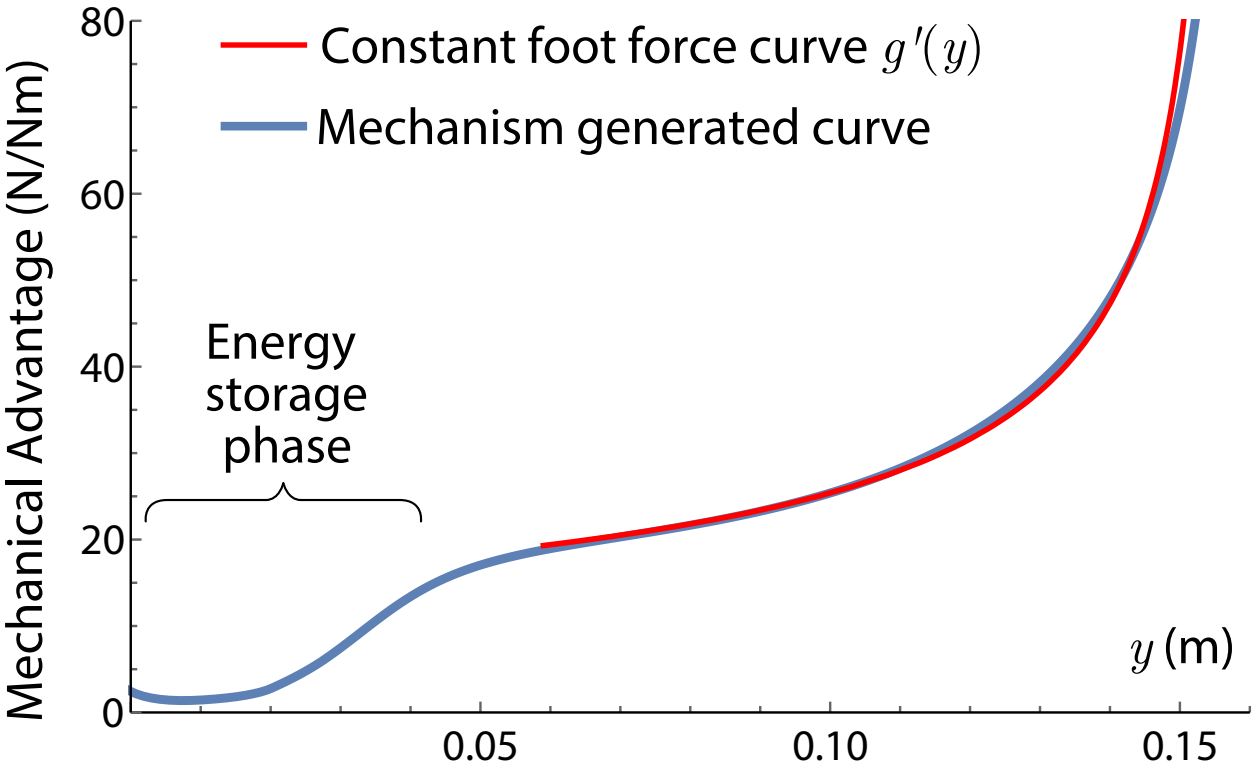

Figure 3.6: The variable MA of the robot's leg mechanism starts with an energy storage phase near singularity (low mechanical advantage) at the top of stroke, then transitions to follow a constant foot force curve. Adapted from [41].

action of the jumping mechanism from rotational dynamics, we stipulate that the angular momentum of the moving links is balanced. If this constraint were not met in a zero external moment environment (i.e. while airborne), the robot body would rotate to some angle dependent on the extension of the leg.

Optimization was performed on the design variables (as described by Plecnik et al [80]), $\mathbf{d}$, a vector of dimension 16 containing the coordinates of pivots and the foot point in a reference configuration defining dimensions of the linkage. Formulating vector loop equalities $\mathcal{C}_j$ for each position j creates constraints between $\mathbf{d}$, the unknown foot coordinates (x_j, y_j), and input crank angles ψ_j, $j = 1, \ldots, N-1$. The objective function is the weighted sum of squared differences between the desired and actual constrained values of these unknowns,

$$\begin{aligned} f = & w_{\text{pt}} \sum_{j=0}^{N-1} \left((\tilde{x}_j - x_j)^2 + (\tilde{y}_j - y_j)^2 \right) + \\ & w_{\text{ang}} \sum_{j \in l} \left((\cos \tilde{\psi}_j - \cos \psi_j)^2 + (\sin \tilde{\psi}_j - \sin \psi_j)^2 \right) \end{aligned} \tag{3.5}$$

where the tilde accent indicates specified desired values. The set l contains the indices of configurations where $\tilde{\psi}_j$ was specified. Symbols w_{pt} and w_{ang} are weights. Equality and

inequality constraints were placed on the elements of $\mathbf{d}$ to enforce packaging requirements, which are denoted as set $\mathcal{D}$. The optimization problem is then

$$\begin{aligned} \min \quad & f(x_j, y_j, \psi_i), \;\; j = 0, \ldots, N-1, \; i \in l \\ \text{subject to} \quad & \mathcal{D}, \; \mathcal{C}_j, \;\; j = 1, \ldots, N-1 \end{aligned} \tag{3.6}$$

The optimization procedure resulted in the design shown in Fig. 3.5(b) which was prototyped using a fixed spring to drive leg extension, shown in Fig. 3.7a. Test jumps of the prototype resulted in an angular velocity of 24.8 rad/s upon leaving the ground, (Fig. 3.7b). This was due to inaccuracies in our initial estimates for link masses, the real link masses violated the assumption that all leg mass would be balanced on the line of action.

The arrangement of links in design 3.5(b) made achieving this balance difficult. The ternary link had mass concentrated away from the body, and all links possess negative angular momentum about the center of mass. These problems were countered by adding a new foot link to the mechanism which was constrained by a second floating link, making the overall mechanism a single degree-of-freedom eight-bar. The addition of these links coarsely balanced momentum but disrupted the straight line, power modulation, and constant force requirements. In order to re-satisfy these requirements, an eight-bar optimization scheme was similarly formulated that allowed coordination of y, ψ, and rotation of the foot ζ to implement momentum balancing, which produced the final kinematic design which is shown in Fig. 3.5(c). We fabricated a spring-driven prototype of this design (Fig. 3.7c) to validate that the balancing procedure was successful. Jump experiments confirmed that there was no rotation produced by the action of the jumping mechanism, as shown in Fig. 3.7d. The obtained MA of this linkage is shown in Fig. 3.6 as the mechanism generated curve.

SE+MA Parameter Exploration

The degree of energy storage in a SE+MA appendage (and the power modulation factor) has a multivariate dependence on the parameters of the series elastic actuator and the MA function. The low MA in the energy storage phase enhances its capacity for energy storage; high average MA during leg extension ensures rapid and complete energy return.

Fig. 3.8 evaluates jump height for two of these parameters: (1) spring stiffness and (2) mechanical advantage in the energy storage phase. The latter refers to MA at the beginning of the stroke which was modified by adjusting the initial configuration of the mechanism according to Fig. 3. Jump height data were determined by simulating mechanisms from a range of energy storage phase MAs and spring stiffnesses. In these simulations of maximum jump height, the mechanism is constrained to move only vertically, the energy return phase MA function is held fixed (with an average value of 26.9 N/Nm), the current input is held at maximum, the motor is a DC actuator model producing a maximum of 25W of power, and the platform weight is 85 grams.

The highest jumps in Fig. 3.8 are found with 0.3 Nm/rad spring stiffness and energy storage phase mechanical advantage ≈ 4 N/Nm. With these parameters, the robot remains

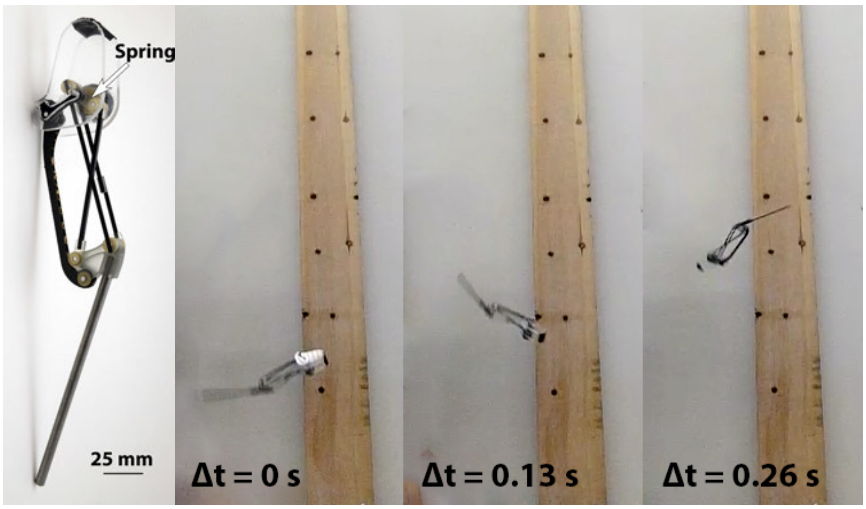

(a) (b)

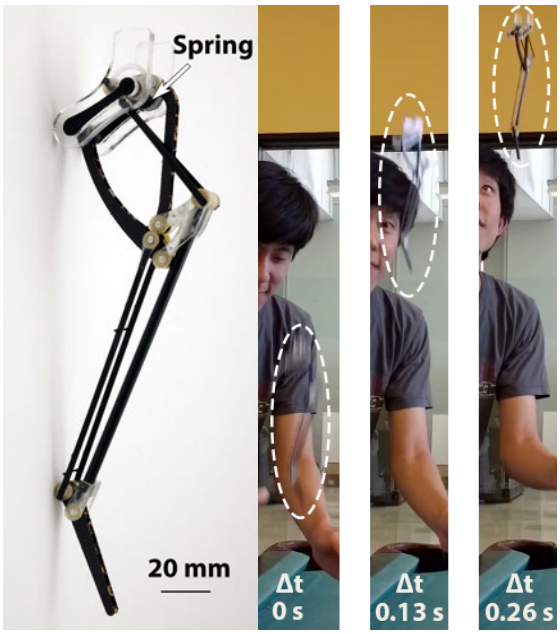

(c) (d)

Figure 3.7: (a) Image of the spring driven 6-bar (b) Stills from a high-speed video showing a rapid body rotation of 24.8 rad/s. (c) Image of the 8-bar leg mechanism (d) a spring powered jump with zero rotation. Adapted from [41].

in the energy storage phase (the region of low mechanical advantage marked in Fig. 3.6 from $0 < y <\approx 0.05$) long enough to transfer significant energy into the spring element. With stiffness less than the optimal value of 0.3 Nm/rad, the robot fails to lift off the ground. For this case, due to a low series spring stiffness, the motor is operating at high velocity and low torque, and the motor torque acting through the mechanical advantage applies a foot force

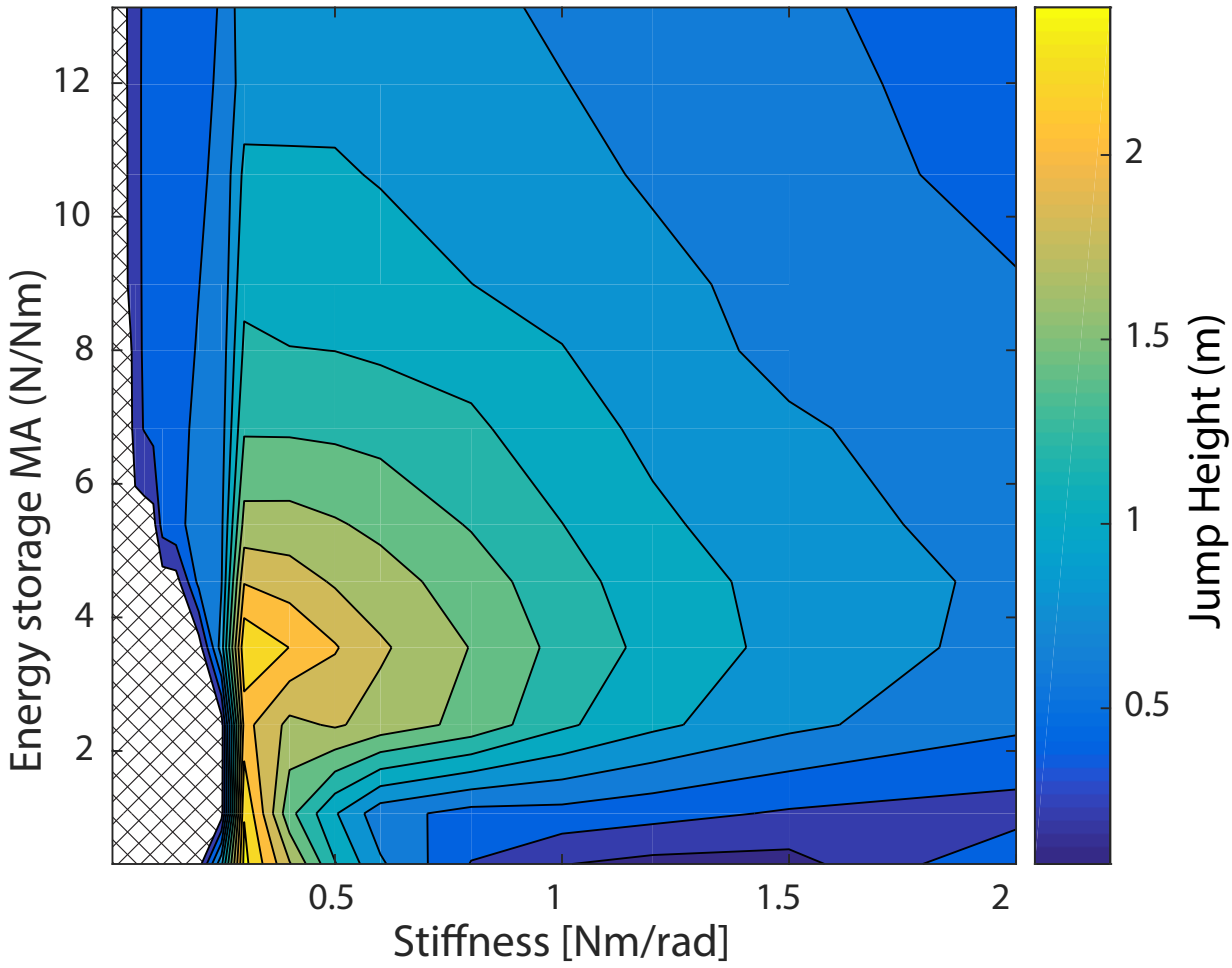

Figure 3.8: Parameter sweep for energy storage phase MA and spring stiffness evaluated for jump height for an 85 gram, 25W jumping robot. The robot is unable to jump in the hatched region. Adapted from [41].

less than or equal to the robot weight. Alternatively, with M.A. of 4 N/Nm and stiffness greater than 0.3 Nm/rad, the jumping performance decreases, as with less energy stored in the spring, the jump height is more dominated by the power of the actuator instead of any power modulating effects. In the limiting case of no series elastic element, the peak power applied is solely the motor peak power.

Leg prototype and experimental setup

We created a motor driven version of the SE+MA leg mechanism, shown in Fig. 3.9a to test its power-modulating properties. Aiming to minimize the moving mass of the linkage, we made as much of the mechanism as possible out of pre-fabricated carbon-fiber materials. We first simulated the mechanism jumping to its maximum attainable height of 2.2m, and

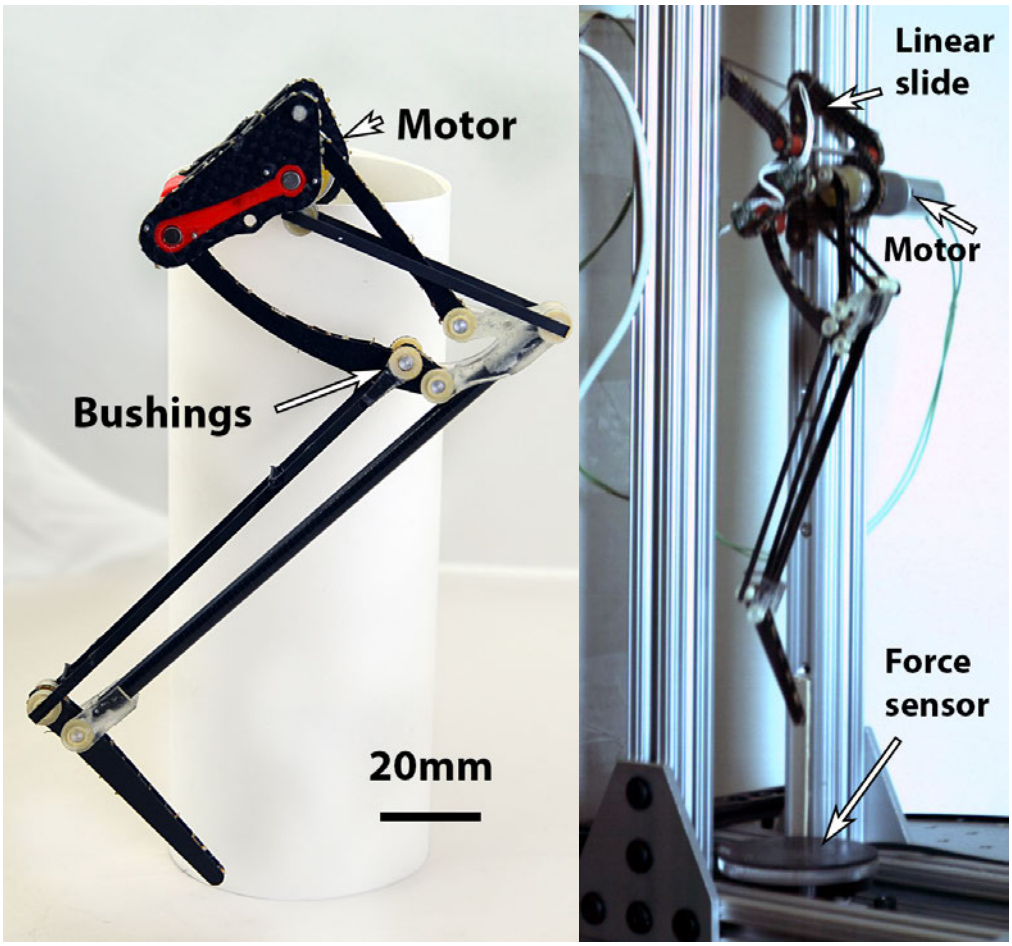

(a) (b)

Figure 3.9: (a) The power modulating leg mechanism, and (b) jumping on the test stand in a still taken from a high-speed video. Adapted from [41].

recorded the resulting internal forces. The binary and ternary links subject to compressive loads are milled from carbon-fiber sandwich panel with a Nomex honeycomb core using a grout-routing Dremel bit installed in an Othermill. The two binary links subject to tension are comprised of slender uni-directional carbon fiber tie rods. The quaternary link is comprised largely of a single carbon fiber tube.

The revolute joints of this robot are made using polymer bushings (*IGUS JFM-0304-05*) reamed and trimmed to accept 0.125" diameter precision ground 2024 Aluminum shaft. This choice saves weight over the alternative ball bearings, and precludes platform failure resulting from brinelling in the impact loaded joints. To connect the bushings to the structural carbon fiber, we use small pieces of molded polyurethane (*IE-3075, Innovative Polymers*). The input crank is entirely made from this material. As a result of this design methodology, the moving mass of the entire mechanism totals only 10.8 grams despite withstanding internal loads up

to 200N.

The elastic energy storage element in the power modulating leg is a torsional spring attached between the motor output and crank. We adopt the conic-sectioned latex element developed for the CMU series elastic snake [85] as our spring. Latex has by far the greatest energy density of commonly available materials, as well as a high resilience. We cut our springs from latex tube stock fabricated with a continuous-dip process (*Primeline Industries*) using a 3D printed jig. The final spring has an active latex mass of 1.5 grams, and a total mass (with attachment features) of 2.5 grams. The stiffness of the spring on the prototype was estimated to be 0.45 Nm/rad during experiments; somewhat stiffer than the optimum (Fig. 3.8).

Our target platform mass is 85 grams, of which the leg and spring claim 13.3, leaving just over 70 grams for actuation, and attachment to the experimental test stand.

We used a low-power, low-cost, off-the-shelf geared motor (*Pololu 20D 154:1*) to test the operating principle of the power modulating leg. This motor weighs 46.9 grams, including the mounting hub. It offers little in the way of control authority, but was readily accessible and demonstrates the power-modulating properties of the robotic leg. The total mass of the robot including leg, body and actuator is 73.4 grams.

Our driven jumping experiments were performed with the robot attached to a vertically-oriented linear slide rail which increased the mass of the robot to 84.8 grams, shown in Fig. 3.9. The leg is free to rotate in pitch on the linear slide carriage. This carriage contributed significant friction in our experiments; there was little room in the mass budget to rigidify the carriage, and any off-axis forces tended to cause jamming issues. To collect data, we logged angle information from two AS5048B magnetic encoders mounted on the ternary carbon fiber link, and motor output, the current of the motor as sensed by a shunt resistor, and the ground reaction force from an ATI Nano43 force sensor, which served as the jumping platform. The force sensor was covered in neoprene rubber to isolate it from shock loads. 1080p video footage of each experiment was recorded at 500 frames per second.

To explore the range of jump heights this robot can attain, we commanded a set of open-loop motor commands in lieu of a closed-loop controller. The robot was set in a starting position with a MA larger than the minimum attainable by the mechanism, which limits the jump height and power modulating capacity of the linkage, as shown in Fig. 3.8. However, this configuration $\psi = g(y)$ was necessary to overcome friction generated by the linear slideway.

SE+MA Mechanism Prototype Results

In this section we present results from robot experiments and simulation. The robot mass was set to be 85 grams in simulation to match the experimental platform. Fig. 3.10 compares the spring and motor power for the simulation vs an experimental jump of the robotic leg. Power is calculated by taking the product of the torque deflecting the spring and the angular velocity of the crank or motor, for spring and motor power respectively. The simulation shows good correspondence with the experiment. The power modulating mechanism allows the spring to

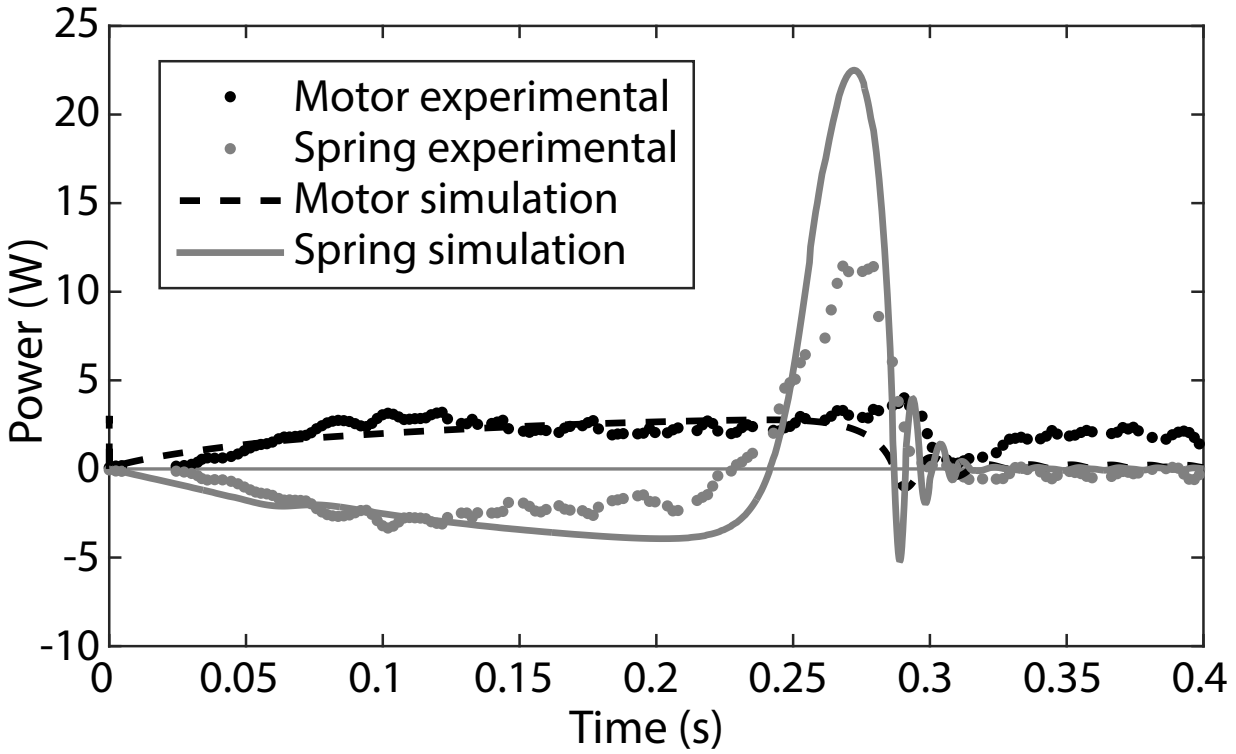

Figure 3.10: Simulated vs measured power for the 3W actuator installed in the prototype. Adapted from [41].

deliver a peak power of 11.4 W, with the motor delivering an estimated maximum of 3.14W, for an instantaneous power modulation factor of 3.63. This factor is lower than the maximum attainable (see Fig. 3.11) in simulation because the robot was not started in its minimum MA position. Friction in the mechanism and slideway resulted in lower peak spring power observed in experiments than the simulation predicted.

We explore the effect of power input level on the power modulating mechanism using a simulation matched to the physical parameters of the robot. For each of these simulations, we fix the maximum torque input and vary the maximum speed of a virtual actuator.

Fig. 3.11 shows the normalized power from the motor and spring during a simulated jump of the leg, as a function of stance time for power input levels of 25W and 2W. The power modulating properties of the linkage are clear for both power input levels. A 25W input to the leg yields a power modulation ratio of 3.6; a 2W input has a much higher ratio of 11.5. The time for the jumping leg to lift off decreases with increasing actuator power, indicating that jumps can be made more frequently with a higher-power actuator.

Fig. 3.12 shows the achievable operational space of the jumping linkage for a range of power inputs to the power modulating leg. These axes are identical to those of the comparison chart shown in Fig. 3.2. Zones of operation were determined by exploring the range of attainable jumps in simulation using open-loop motor commands. This exploration

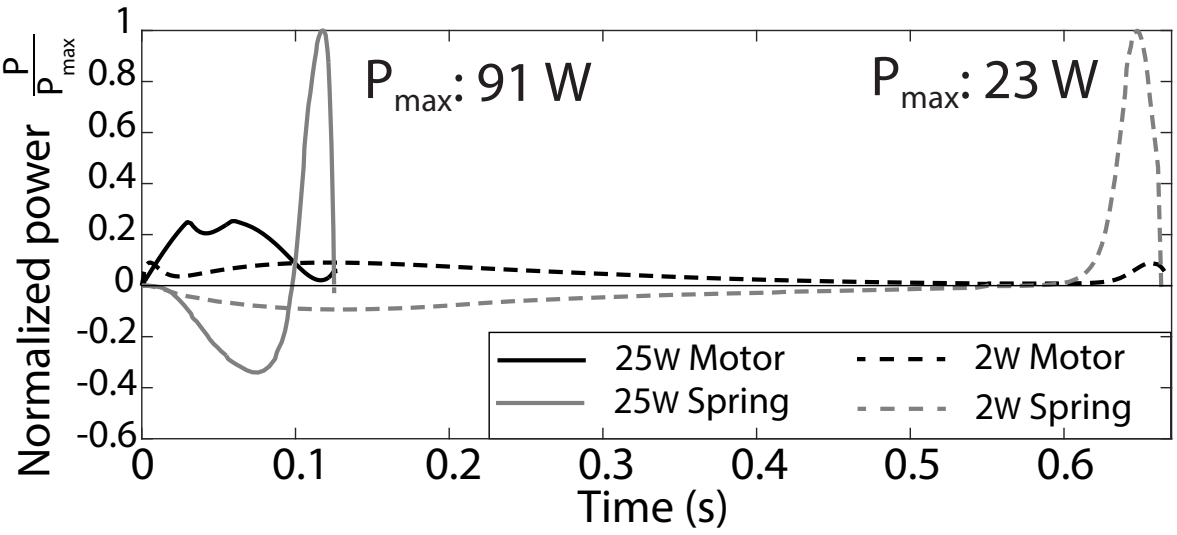

Figure 3.11: Normalized motor and spring power for simulated actuators producing a maximum power of 25W and 2W. Adapted from [41].

yielded a pareto-optimal set in the operational space. The operating region is defined as the projection of the set of pareto-optimal jumps to the horizontal axis; physically this means that any jump that can be made quickly can also be made slowly by delaying the onset of actuation. The simulation predicts that the robot can make controlled, repeatable jumps anywhere in these zones of operation.

The greater the level of power input to the leg, the more agile the system becomes and the greater the attainable jump height, up to a maximum of 2.2m at a power input level of 15W. We found that no significant gains in jump height are expected by further increasing the power to 25W; the increased operational space only appears as a slight expansion of higher frequency motion.

Also shown in this figure are experimental data gathered from the robot jumping on the test stand. Each of these data points represents the robot jumping with motor commands defined as follows: first the motor PWM command is set to 90% of full range to lift the mechanism out of the low MA region. When the mechanism is almost out of this region, the motor command changes to a fixed constant value from -100% to +100% PWM duty cycle. Varying the motor command causes the robot to jump to various heights, as shown in the inset of Fig. 3.12. Increasing motor commands lead to a corresponding increase in jump height. The experimental data falls within the envelope expected for a 3W power level. The jump height observed in experiments falls below the predicted maximum, which is a combined effect of a spring that was stiffer than predicted (see Fig. 3.8), exacerbated by friction and jamming in the linear slideway. The maximum agility was 0.71 m/s; this value is not shown in Fig. 3.2 because the robot drew power from a tether.

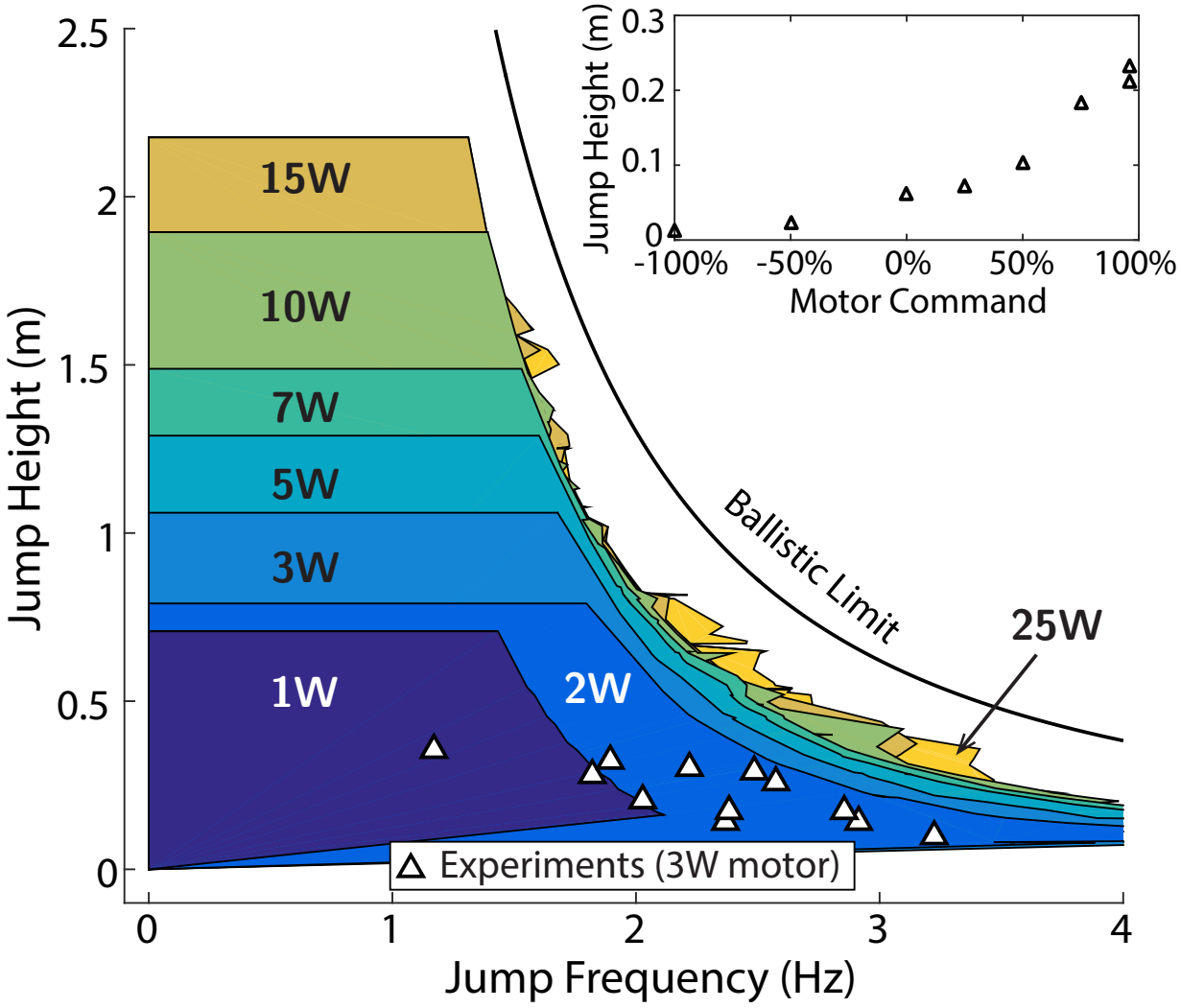

Figure 3.12: The achievable operational space of the power modulating mechanism for a range of power inputs. Also shown are experimentally observed jumps with the leg prototype. *Inset:* Experimental data showing jump height as a function of motor command, the motor input specified as a fraction of maximum voltage applied during the second phase of the jump. Both figures created for the 85 gram jumping platform. Adapted from [41].

3.3 A Robotic Prototype Integrating Power Modulation

With encouraging results from the leg mechanism prototype, we built a physical robotic prototype, Salto (shown in Fig. 3.3C), to experimentally examine power modulation and its effect on locomotory performance. The result of the design methodology is a monopedal jumper composed of a refined version of the leg mechanism, a higher-power series-elastic

actuator, and an inertial tail for attitude control. Salto was designed to minimize mass so that less energy is required per unit height gain and to improve robustness against high-energy collisions created by agile locomotion. Physical parameters of Salto are given in Table 3.2. It jumps in free space, with neither tether nor planarizing boom, both of which might interfere with agile motions.

Improved series-elastic actuator

Salto uses the same conic-sectioned latex spring employed by the leg mechanism prototype, but the motor was upgraded to a custom BLDC motor and gearbox from the COTS motor. The brushless motor started as a Scorpion S-1804-1650KV winding kit obtained from the factory, wound with 48 turns of 30AWG (American wire gauge) magnet wire. We statically verified the torque constant. The custom wound stator was mounted in a custom 25:1 gearbox for a total mass of 25.29 g. An AS5047P magnetic encoder calibrated to rotor position generated commutation signals for a current controlling brushless DC motor driver (AZB10A4, ADVANCED Motion Controls). The reference was generated by an Imageproc robot control board [8] (printed circuit board: https://github.com/biomimetics/imageproc_pcb, firmware: https://github.com/dhaldane/roach). A second AS5048B magnetic encoder measured the angle of the lower ternary link; the angular deflection of the spring was estimated with an inverse-kinematics look-up table.

System electronics

The system was powered by a three-cell 11.1-V 180mA-hour lithium polymer battery (Turnigy nano-tech). The control board recorded telemetry (six-axis inertial measurement unit, estimated body angle, leg position, and motor position) at 1000Hz. It was controlled from a laptop via an onboard ZigBee radio interface. The robot was controlled with two independent linear feedback laws: a proportional controller on motor position and a proportional-derivative controller on body angle. Body angle was estimated by integrating a single axis on the onboard gyroscope. The controller for the wall jump was implemented as a state machine. When started, it sets the pitch set point forward to angle the robot toward the wall. Once the pitch angle reaches a threshold, leg extension is triggered and the robot jumps. In the air, the robot retracts its leg, and the pitch setpoint is set to the angle at which the robot should contact the wall. Contact with the wall is detected by either the spring displacement exceeding a threshold or the rotational rate of the robot exceeding a threshold. This detector ensemble is more robust against variations in the angle of incidence with the wall than either detector in isolation. Once wall contact is detected, leg extension is again triggered and the robot jumps off the wall.

Inertial tail

The final component of the robot is an inertial tail for pitch reorientation. This strategy is used by leaping agama lizards [68] and has been used in several other robotic platforms [104, 60, 61]. In contrast to these other systems, which use an unbalanced distal mass, our tail is mass-balanced about its point of rotation (similar to the KAIST (Korea Advanced Institute of Science and Technology) Raptor). This decouples the angular position of the tail from the center of mass location of the system. Furthermore, it allows the use of a smaller tail motor that would be otherwise overwhelmed by torques generated by characteristically large accelerations developed in stance phase.

3.4 Robotic experiments

To measure the vertical jumping agility of Salto and determine the efficacy of the SE+MA strategy, we performed a series of vertical jumping experiments to determine the maximum height gain that the robot could achieve. The robot was equipped with a lightweight foot (visible in Fig. 3.3C) to statically stabilize out-of-plane rotation. The robot was placed on the floor with the center of mass directly above the foot; a step input was then applied to the motor position that drove the jumping linkage to full extension. The tail was not activated for these trials, precluding a controlled landing. The robot was caught by hand after it reached apex. This procedure was repeated for 10 consecutive trials. The maximum jump height was 1.008 $\pm$ 0.007 m (N = 10, mean $\pm$ 1 SD). The average stance time was 0.1223$\pm$0.0006s, and the average flight time to apogee was 0.4533$\pm$0.0015s, for a frequency of 1.74Hz and an average vertical jumping agility of 1.75 m/s. This point is shown in Fig. 3.2, demonstrating that Salto has achieved the highest vertical jumping agility of any extant robot.

To anchor the meaning of vertical jumping agility in the context of locomotion, we demonstrate a wall jump with the Salto robotic prototype. In this experiment, the robot starts in a stable configuration on the floor, uses the tail to orient itself toward the wall, jumps, reorients, and then jumps again off the wall. Parameters for this jump were tuned to maximize the height gained off the wall. The wall jump was performed consecutively for eight trials until the robot failed to perform the maneuver. This failure resulted from damage accrued by the inertial tail, causing the robot to fail to properly orient itself toward the wall. The battery was returned to a full state of charge before each wall jump to isolate sources of experimental variability. The robot was placed 0.59 m away from the wall; markers on the ground ensured repeatable alignment. The wall in these experiments consisted of a 0.25-inch-thick acrylic plate mounted to an extruded aluminium frame. To increase traction, a 0.175-m diameter of 0.25-inch-thick polyurethane rubber was added 0.88m above the floor, where the robots foot was expected to make contact. The frictional coefficient was such that Saltos foot did not slip during any of the trails. In addition to telemetry, video footage of each experiment was recorded at 500 fps using a MegaSpeed HHCX7. Video tracking software

(ProAnalyst, Xcitex) was used to extract kinematics from each experiment. Motor power was calculated using the current command sent by the Imageproc using the identified motor model and measurements of motor speed. The spring power was estimated by approximating the torque from the spring deflection using estimated spring stiffness and multiplying that estimate by the measured rate of change of spring angle. The extrinsic energy of the system during the wall jump was estimated from the kinematic tracking data. The motor and spring power are shown in Fig. 3.13A for the starting jump and in Fig. 3.13B for the wall contact phase.

Fig. 3.13A shows motor and spring power as a function of time for the robot jumping from its fully crouched position. This figure shows the effect of the SE+MA appendage on power modulation. Eight consecutive trials are shown on this plot, with the time axis starting with the onset of motor activation. The leg stays in the low-MA region (shown in Fig. 3.6) until 0.06 s into the stroke, loading energy into the spring. After this point, the MA increases and the energy in the spring is returned to accelerate the robot. The average (N =8) peak spring and motor power were 40.3±1.54 and 13.7±0.0W, respectively, showing that the spring provided 2.94 times greater power than the motor alone can produce. These data also show the consistency of the power-modulating behavior when the platform starts from rest.

When jumping off the wall, the power-modulating effect is less prominent because contact is made with the leg extended out of the energy storage region, as shown in Fig. 3.13B. Integrating the motor power shows that an average of 1.22 ± 0.01 J was delivered during the starting jump, and 1.04 ± 0.03 J was delivered during the wall contact phase. Variation in initial conditions when the robot contacts the wall caused this phase to be more variable than the starting jump.

The wall jump was based on internal measurements, with a state machine governing the transitions between the phases of the maneuver. Without a controller operating on exteroceptive measures, this is an open-loop behavior; thus, variability is expected to grow over time. Fig. 3.14A shows motion-tracked position traces for the eight consecutive wall jump maneuvers, with the robot shown for scale. The starting jump produced closely grouped trajectories for the robot approaching the wall, the variation resulting from differences in tail action during stance. The trajectories diverge after the robot contacts the wall, as can be seen in Fig. 3.14 (A to C). This greater variability is driven by discrepancies in foothold location and body orientation relative to the wall. Fig. 3.14D is a bar chart showing the extrinsic energetic state of the robot before and after the wall contact phase. Each wall jump increased the energetic state of the robot from an average of 0.96 ± 0.03 to 1.21 ± 0.06 J. The average energy gain from the wall contact phase was 0.25 ± 0.04J; thus, the variation in extrinsic energy increases with each phase of the wall jump, but the variability of energy production for both phases was similar. We can estimate the efficiency of the starting jump and wall contact phase as the ratio of energy delivered by the motor to the increase in kinetic and potential energy. The starting jump had an average efficiency of 79 ± 3%, on par with other jumping robots [56]; the wall contact phase had a lower efficiency of 24±4%, presumably dissipating energy through collision with the wall.

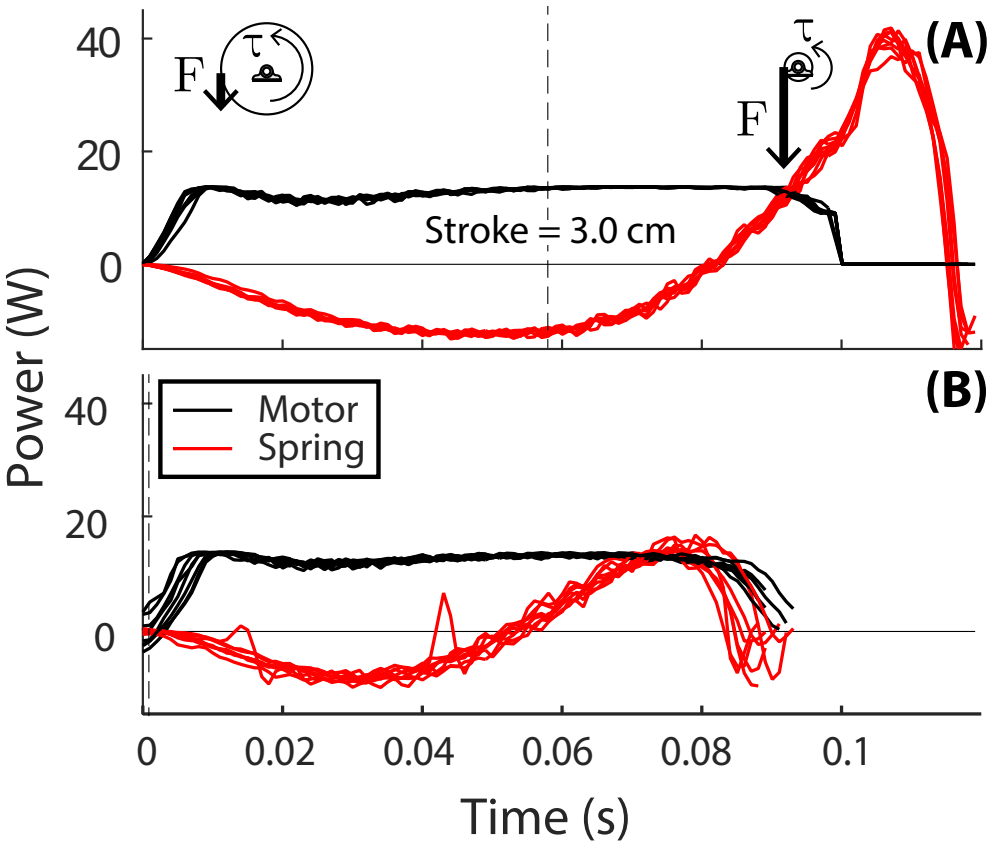

Figure 3.13: Spring and motor power for (A) the starting jump of the wall jump maneuver and (B) the wall contact phase (N = 8). The dashed line indicates where the leg moves from the storage to return MA regions (shown in Fig. 3.6). Adapted from [43].

The robot attained an average height gain of 1.21 ± 0.065 m for the wall jump, reaching an average of 0.4 m higher than the foothold location on the wall. The maximum height increase was 1.29 m, 0.28 m higher than the maximum achievable were the platform jumping from the floor.

3.5 Conclusions

A bioinspired series-elastic power-modulating strategy was tested with a robotic prototype, resulting in the highest recorded robotic vertical jumping agility: 1.75 m/s. Salto's vertical jumping agility was higher than that of a bullfrog but fell short of the vertical jumping agility of the galago (2.24 m/s).

Power modulation enables agile robots by reducing the motor power density required to perform energetic jumps. An optimal design study showed that any system with rigid or series-elastic actuators lacking an MA adaptation requires excessive power densities (more

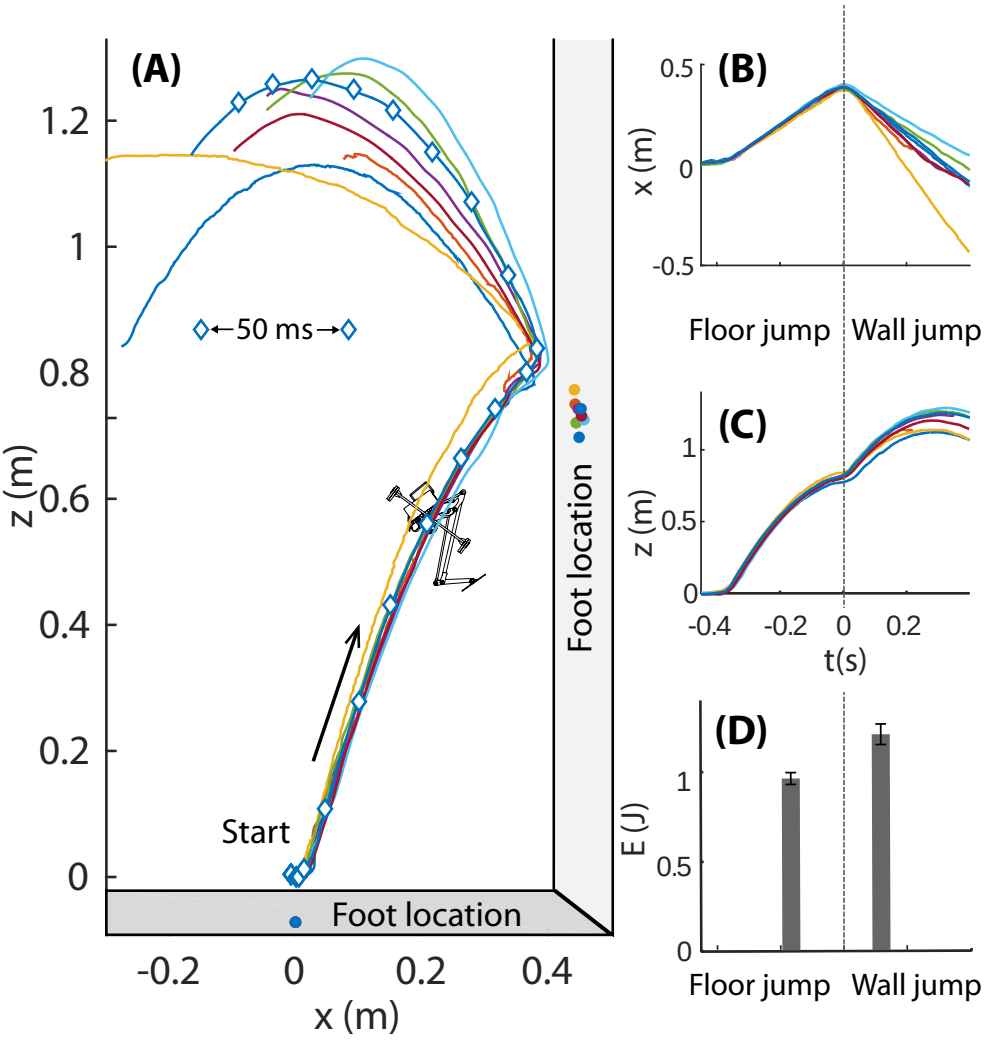

Figure 3.14: Trajectories of the robotic wall jump experiments. (A) Trajectory of the body center of mass for eight consecutive wall jumps. (B) Horizontal displacement versus time. (C)Vertical displacement versus time. (D) Bar chart of the energy of the robot before and after the wall contact phase. Error bars indicate 1 SD. Adapted from [43].

suited to hovering flight than legged locomotion), if they are to perform as well as the galago. A hypothetical piecewise constant MA adaptation, coupled with a series-elastic actuator, created a power-modulating system that reduced the required power density by a factor of 3.6, making a robot with the agility of a galago physically realizable. An alternative to an SE+MA actuator is the sort of parallel-elastic device that propels the highest-jumping robots in Fig. 3.2. The required power density (assuming spring winding during both stance and flight phases) is less than that required for an SE+MA actuator. However, there are several shortcomings associated with the parallel-elastic approach. These are perhaps best analyzed in the context of the wall jump maneuver. The wall jump requires two repeated, controlled

jumps. Parallel-elastic mechanisms typically require position control to set spring length and force and can thus complicate leg force production. An SE+MA actuator preserves force control authority by maintaining the actuator in a series arrangement. During the wall jump, Salto retracted the leg near the free-running speed of the motor to prepare for wall contact. This would not have been possible with a comparable parallel-elastic mechanism because of the energetic work required to change leg position. The robots ability to perform a high-power jump, rapidly reposition its leg, and jump again off a wall was enabled by the choice of an SE+MA actuation strategy.

The SE+MA leg had repeatable performance, as shown by the power curves in Fig. 3.13 and the small height variation in the vertical jump experiments. It also had predictable behavioridentical inputs producing similar outputs. The deviations in trajectories shown in Fig. 3.14 are not due to some inherent flaw in the mechanism but rather result from the lack of a true closed-loop controller for the behavior. The robot was able to gain height by jumping off the wall, using an environmental feature to increase its operational space. This maneuver can be seen as the first stage of a vertical chute ascent, which was first demonstrated by ParkourBot in its limited gravity environment [28]. This wall jump is an example of a maneuver enabled by highly vertically agile robots.

The main limitation of the experimental study is that the robot can only perform planar maneuvers. All of the actuation for leg extension and inertial reorientation is concentrated in the sagittal plane, and any perturbation away from this plane cannot be rejected. The robot was only operated on hard surfaces with reliable traction; how it would interact with real-world environments and granular media would be an interesting topic of study. The robot only had access to proprioceptive measures, with no capacity to reason about features in the environment and its pose relative to them. The wall jump behavior was open-loop in that sense, being regulated by a set of parameters tuned to produce a reliable behavior.

The study of series-elastic power modulation showed that it is an actuation strategy well suited to agile robots and a viable alternative to parallel-elastic actuation. These results are broadly applicable to robotic locomotion. More directly, the leg mechanism developed in this work can be coupled with a hip mechanism to form the legs of an agile polypedal robot. The vertical jumping agility metric forms a basis of comparison for agile motions, allowing further exploration of robotic actuation strategies. Our goal is that series-elastic power modulation will enable further study of highly agile robotic locomotion.

Chapter 4

Spatial Agile Locomotion

4.1 Introduction

We have shown that Salto, a robot with a series-elastic actuator and a variable mechanical-advantage (SE+MA) limb [41, 43, 80], can jump over 1 meter in height. The SE+MA actuation strategy allowed the robot to reach this height without a lengthy wind-up period, and without hampering the controllability of the leg with a mechanical escapement or reliance on explosive chemical propellants.

The major shortcoming of Salto was that it was purely planar. Any perturbation away from its plane of operation could not be rejected and so the robot could only perform behaviors with small numbers of jump without falling over. Furthermore, Salto only had proprioceptive sensing and lacked a controller that would enable it to perform an extended series of repeated jumps.

In this chapter we increase the capability of Salto by adding full attitude control. A mass-minimal strategy is used to ensure that the earlier power-density-first goals of the platform are not compromised. We implement the simple Raibert controller [82] to enable Salto-1P to jump repeatedly on a horizontal surface, and explore the range of impulses that can be generated by single stance events.

Section 4.2 outlines the development of the robotic hardware, attitude controllers, locomotion controller and experimental procedure. Results for attitude control and jumping experiments are given in Section 4.3, and conclusions are discussed in Section 4.4.

4.2 Methods

Attitude control

The first challenge for Salto-1P was to enable attitude control, so that the spatial touchdown angle of the leg could be modulated. The original Salto was planar, and used a mass-balanced inertial tail to control its orientation in the saggital plane [43]. This tail provided an effective

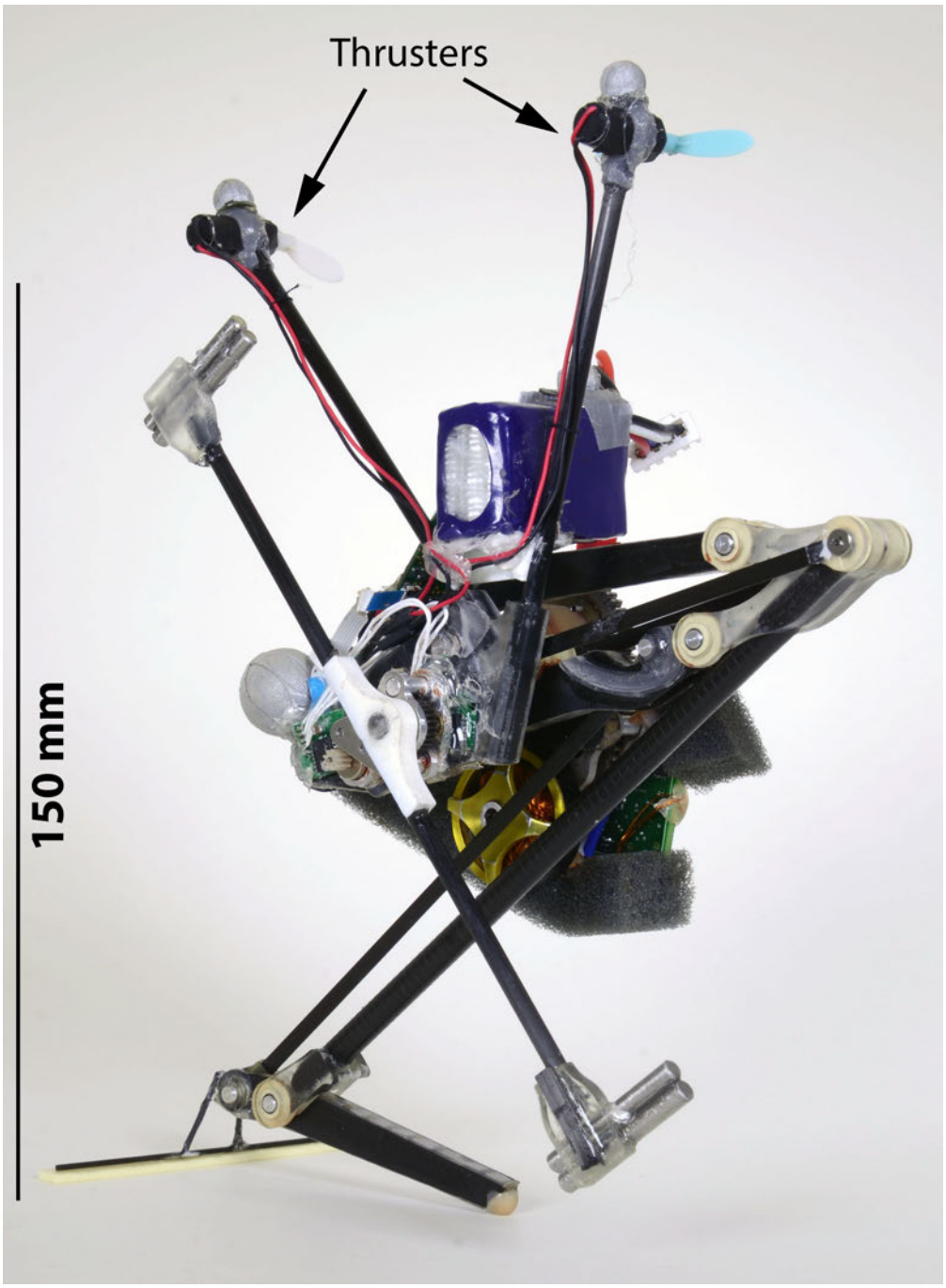

Figure 4.1: Photograph of Salto-1P with thrusters, fully crouched. Photo credit: Ethan Schaler. Adapted from [40].

means of attitude-control and allowed for the aggressive repositioning required to perform the wall-jump maneuver [43]. For Salto-1P we decided to maintain this capacity for rapid

reorientation in the saggital plane and minimally supplement it with enough control authority to keep the robot upright, with the correct yaw heading. A challenge for stabilizing extreme-acceleration jumping is the short duration of the stance time relative to flight time. Any method of stabilization that operates only in stance (such as a foot or articulated ankle) must correct the attitude within the 0.05s stance window, ensuring that the take-off angular velocity is low enough that the robot is within a few degrees of its desired touchdown angle at the next stance event, 0.5s later.

There have been numerous stabilization methods used for monopoedal robots (see Sayyad et al. for a review [86]). For testing purposes, most commonly the monopode is mounted to a boom to stabilize out-of-plane rotations, which is unsuitable for Salto-1P due to the low mass of the robot and the magnitude of its vertical excursions. Another option is to mount the leg on a two degree-of-freedom servo joint at the center of gravity of the body of the robot, as was done for the Raibert Hopper [82] and the 3D Bow Leg Hopper [103]. This is unattractive for Salto-1P because the movement range of the body becomes limited, greatly limiting the angular impulses it can reject. Any reorientation strategy with an offset mass (such as a 2 DoF tail [25]) presents difficulties for Salto-1P due to characteristically large accelerations in stance that create large torque requirements on the tail actuators. Other monopodes (e.g. [53, 96]) opt for statically stable feet and avoid jumps that would cause the robot to leave its support polygon. This approach is untenable for Salto-1P, which can jump two meters horizontally.

Several jumping robots use aerodynamic surfaces to glide after jumping [99, 63, 29]. Aerodynamic surfaces are attractive means of control for their low mass and ability to apply force while airborne (not just in stance). A drawback is the large requisite size at the Reynolds numbers associated with terrestrial locomotion, and that force they apply is velocity-dependent so a robot jumping vertically loses control authority at apex. We opted for a compact aerodynamic-stabilization method that does not rely on body velocity by using the thrusters seen in Fig. 4.1. These thrusters are commercial mini-quadcopter (*Cheerson CX-10*) propeller blades mounted in a 'V' configuration, with moment arms about the center of gravity that prioritize control over roll angle over yaw angle. A roll torque is created by driving both thrusters in the same direction; a yaw torque is generated with a differential motor command. The thruster assembly successfully stabilized the robot (see Figs. 4.4 and 4.5), and had a net mass of 0.0044 kg.

Robotic Hardware

Salto-1P is an improved version of the Salto robot [43]. The series elastic actuator and mechanism geometry from Salto have been preserved in Salto-1P. However, some of the links have been reshaped to allow Salto-1P to get lower in crouch than Salto, to increase the achievable jump height by enhancing the power-modulating effect of the linkage [41]. The body was also redesigned using topology optimization to create a highly mass-efficient, low compliance structure. The tail gearbox has been upgraded to steel gears with an aluminum

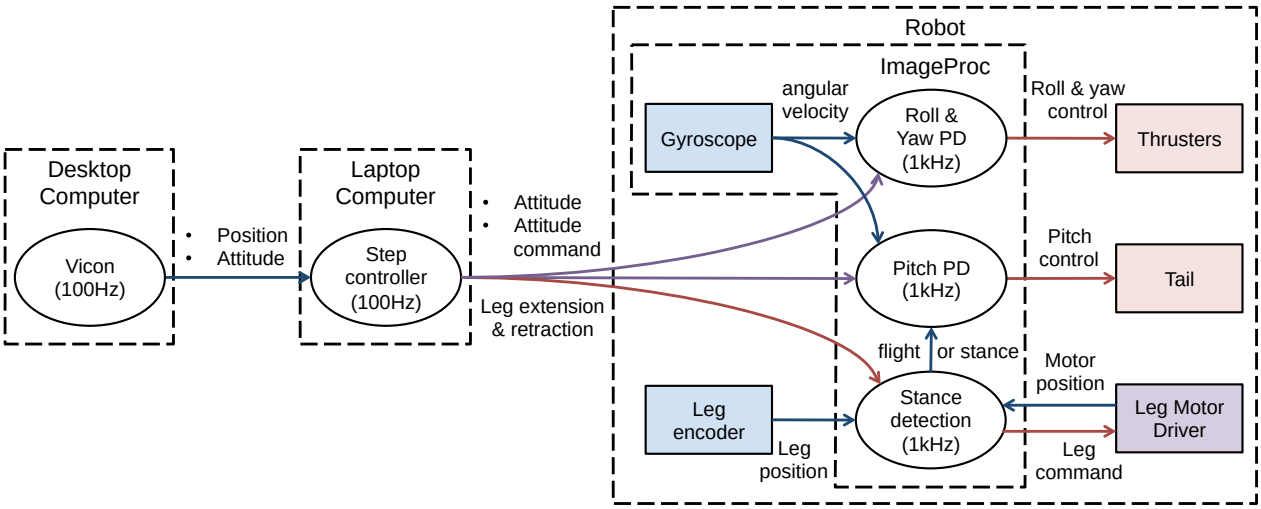

(a) Control block diagram

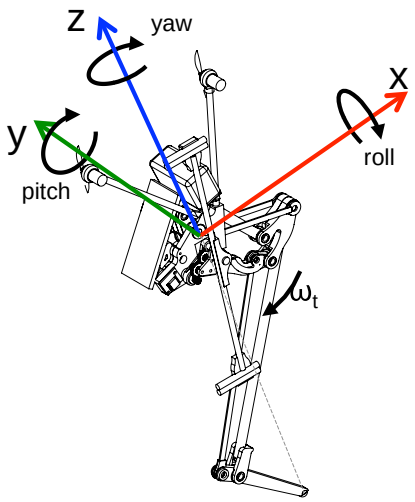

(b) Diagram of Salto with reference frame, control variables

Figure 4.2: Overall system block diagram and reference frame of Salto-1P. Adapted from [40].

housing in Salto-1P, after observing that Salto's plastic tail gearbox was a source of much unreliability [43].

Like Salto, Salto-1P is controlled with the ImageProc 2.5[1] robot control board [8]. The tail and thruster motors are driven from onboard H-bridges. Salto-1P uses a customized BLDC motor driver[2], which is smaller and lower mass than the COTS driver used by Salto.

[1]Embedded PCB: https://github.com/biomimetics/imageproc_pcb
[2]Embedded PCB: https://github.com/biomimetics/modular_robotics_pcb

The imageProc records telemetry from the motor driver, and an onboard 6-axis IMU at 1 kHz.

Salto-1P contacts the ground with a hemispherical rubber toe (IE7000, *Innovative polymers*). A sample of the toe material was rubbed on a sample of the carpet from the test chamber while a force-sensor (nano43, *ATI*) recorded data to determine the frictional coefficient, $\mu = 0.79$. When the robot is fully crouched, it rests on a ankle structure, seen in Fig. 4.1, that allows a statically-stable rest position. The height of this ankle is such that the center of mass is located behind the toe of the robot.

Jumping controller

Salto was designed as a direct instantiation of the spring-loaded inverted pendulum (SLIP) model of running [14], so that the control of the platform could be made as simple as possible. The goal was to have Salto appear dynamically as a point mass on a spring-loaded massless leg. Salto's toe point moves in a straight line, the mass of the leg was minimized, the leg mechanism was balanced so that motion of the links produces no body rotation, the inertial tail is mass balanced, and the mass of the body was centralized [41, 80]. This is an opposite design approach to the Acrobot jumper that used a minimal mechanical design with nonlinear control, and could barely slide while maintaining balance [12]. Designed in this way, Salto resembles an untethered, 0.098 kg version of the Raibert hopper [82] that has one of the leg angle positioning servos replaced with thrusters, and the other leg positioning servo replaced by an inertial tail for pitch control, has control over its yaw heading, and can jump 1.25m high.

Seeking the simplest solution, we elected to implement a linearized controller based on the Raibert step controller [82] for our initial experiments.

As in the Raibert step controller, control is decoupled into three parts, albeit here the three parts are: hopping height, tail velocity, and horizontal velocity.

Table 4.1: Robotic platform metrics

	Salto,Haldane2016a	**Salto-1P**
Mass (kg)	0.1000	0.0981
Active leg Length (m)	0.138	0.144
Maximum jump height (m)	1.007	1.252
Vertical jumping agility (m/s)	1.75	1.83
Max control torque (Nm):		
Pitch	0.029	0.034
Roll	0	0.0078
Yaw	0	0.0039

Hopping height is set by applying a fixed thrust on the ground. Thrust is specified by selecting the leg retraction length before touchdown and a leg extension distance that is triggered when the robot contacts the ground (detected by monitoring the deflection of the spring in the series-elastic actuator). Over multiple hops, the system converges to a steady state apex height.

Salto-1P's balanced tail is analogous to the balanced body of Raibert's hopping machine. However, since the tail rotates without limit, its angle is unimportant and we are concerned only with its angular velocity. During stance phase, the H-bridge driving the tail motor is put in brake mode to slow down the tail. This is important for maintaining control authority: the control torque the tail can produce decreases linearly with tail speed. Without braking, the tail accelerates to the free-running speed of the motor, and the robot is unable to maintain control of its locomotion.

Horizontal velocity is controlled by selection of an appropriate leg angle at touchdown. For simplicity, we use yaw-roll-pitch Euler angles to parameterize rotation. The robot-attached reference frame is shown in Fig. 4.2b. Since Salto-1P's inertial tail grants greater control authority about the pitch axis than the thrusters provide about the roll axis, maneuvers are guided to the sagittal plane and the desired yaw angle is 0. Given the desired CG positions and velocities, the touchdown roll and pitch angles are selected by:

$$\phi = -k_{Px} sat(x_d - x, x_{max}) - k_{Vx}(\dot{x}_d - \dot{x})$$
$$\theta = k_{Py} sat(y_d - y, y_{max}) + k_{Vy}(\dot{y}_d - \dot{y})$$

Where ϕ is the pitch angle, θ is the roll angle, and $sat(u)$ is the saturation function that limits the angle command due to position error. x is the position coordinate in the sagittal plane, y is the lateral coordinate.

Experimental procedure

To test the stabilizing capacity of attitude controlling actuators, the robot was suspended from the yaw, pitch, and roll axes in turn and was given impulse disturbances by hand. During this experiment the attitude controller tries to maintain a fixed angle; the angular perturbation and subsequent recovery was observed with external motion tracking (*Optitrack*). The size of the impulse was estimated using data from the on-board gyroscope.

Jumping experiments were conducted in a Vicon motion capture environment in order to provide position feedback. The trackable area in the room measures 2 by 3 meters on the ground. Vicon position and orientation measurements were passed at 100Hz to the ground station running in ROS on a laptop computer. The ground station estimated body velocity from the Vicon position measurement by discrete differentiation with a low pass filter. The ground station calculated the desired leg lengths and touchdown angles using the step controller detailed above and sent these commands along with the Vicon attitude measurement to the robot over an XBee radio connection. Sending the Vicon measured attitude, as well as an attitude command, prevents the onboard attitude estimate from drifting due to gyro integration error. The control flow is shown in Fig. 4.2a.

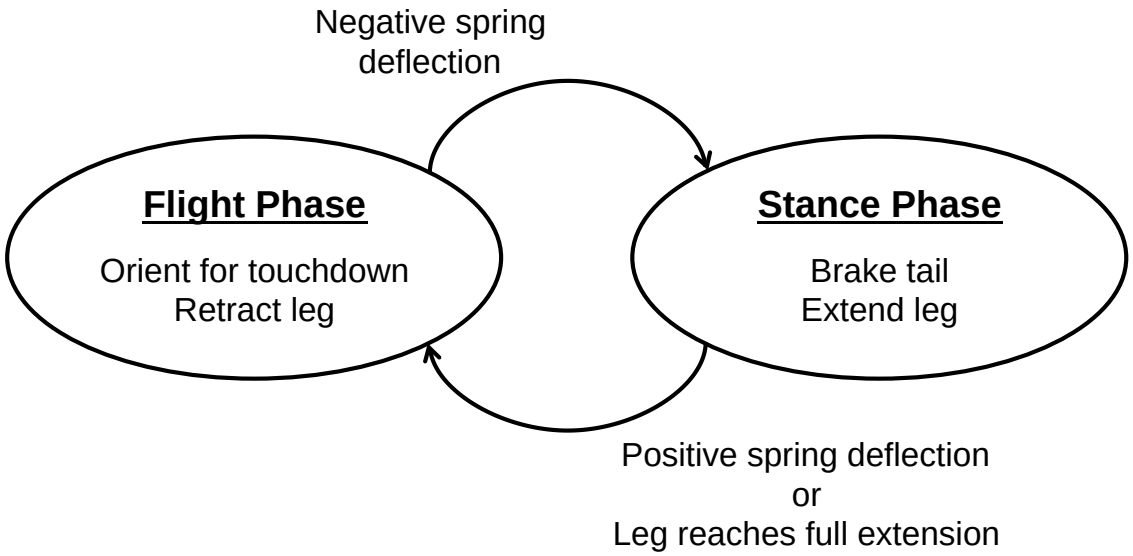

Figure 4.3: Stance and Flight control. Adapted from [40].

4.3 Results

Attitude stabilization

Fig. 4.4 shows 5% recovery time vs. perturbation impulse for Salto-1P in yaw, pitch, and roll. Salto-1P recovers from pertubations in pitch more quickly than any other axis. The inertial tail allows for this rapid response, providing larger torques than the thrusters are able to produce. Note that the maximum angular impulse the inertial tail can reject is limited.

The maximum angular impulse can be no more than $H_t = I\omega$, where I is the inertia of the tail, and ω is the maximum tail angular velocity. $H_t = 3.5mNm - s$ for the inertial tail on Salto-1P. The thrusters are configured to lend more actuation authority to roll rather than yaw (see Table 4.1) and the result of this configuration is shown in Fig. 4.4. The robot recovers from a disturbance impulse of a given magnitude faster in the roll axis than the yaw axis.

Fig. 4.5 shows the tracking performance of the attitude controller during a jumping experiment. The roll and yaw axes (Fig. 4.5(A),(B)) are under-damped with regular deviations of 0.1 radians from the setpoint. More aggressive gains do not yield better performance because the thruster motors are saturated, as shown in Fig. 4.5(C). More actuator authority would be needed to achieve better tracking performance. The inertial tail affords more control authority, allowing good tracking of the commanded pitch angle with typical errors at touchdown lower than 0.01 radians, as shown in Fig. 4.5(D). As mentioned previously, the tail motor (Fig. 4.5(E)) brakes during stance phase to slow down. After takeoff, the tail motor applies maximum effort to reposition the body to the next setpoint.

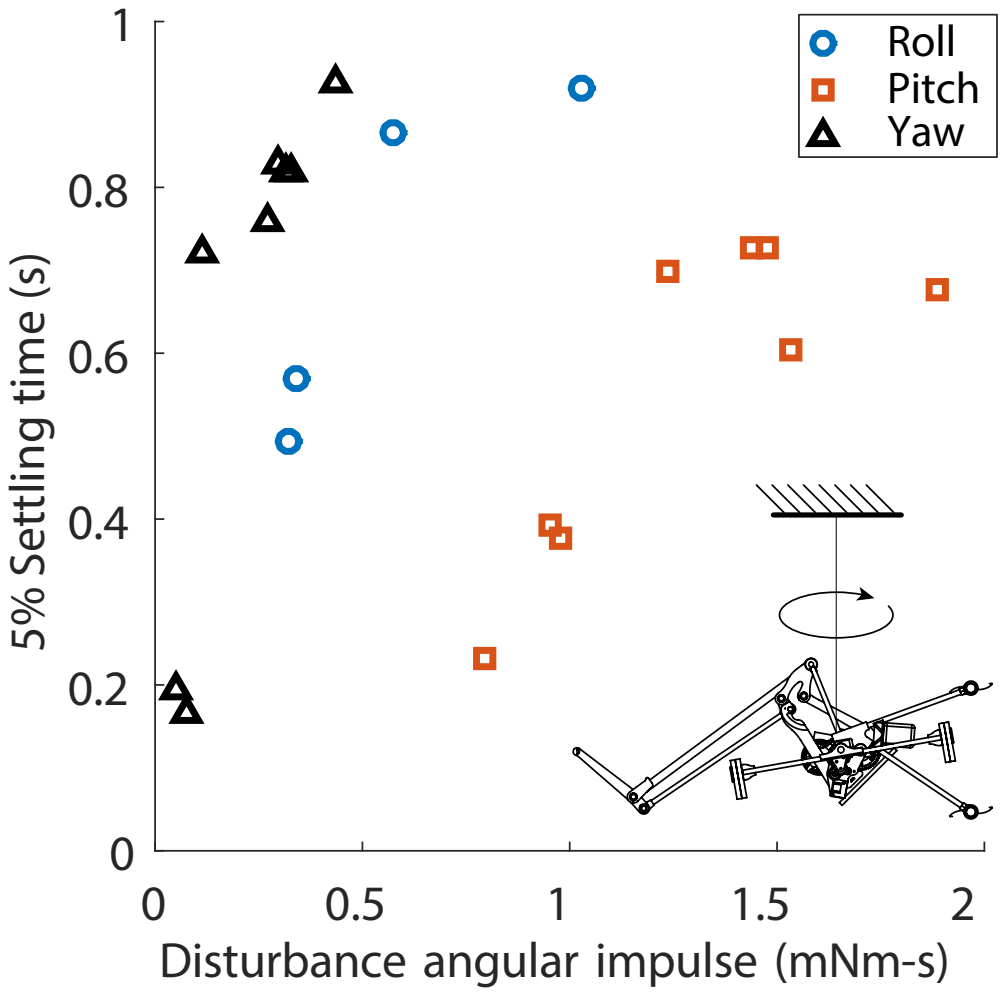

Figure 4.4: Time for Salto-1P to stabilize to within 5% of maximum overshoot vs disturbance impulse. Inset cartoon shows experimental setup for roll tests. Adapted from [40].

Saltatorial locomotion

Fig. 4.6a shows the spatial trajectory of Salto-1P during a forwards jumping experiment. Stills from high-speed video of the same experiment is shown in Fig. 4.6b. The robot starts in its fully crouched posture, statically stable on its ankle, with the center of gravity positioned behind the toe. Salto-1P's most energetic jumps occur when it starts from its fully crouched position, where the SE+MA jumping appendage is most fully in effect [41, 43]. Because the center of gravity is behind the toe, this initial energetic jump is backwards. This starting configuration was used for all of the jumping experimental runs because the first jump immediately establishes the high energetic state requisite for extreme saltatorial locomotion; the backwards direction perturbs the locomotion controller so that a large range of jumps are explored, and the convergence properties can be studied. The robot exits the

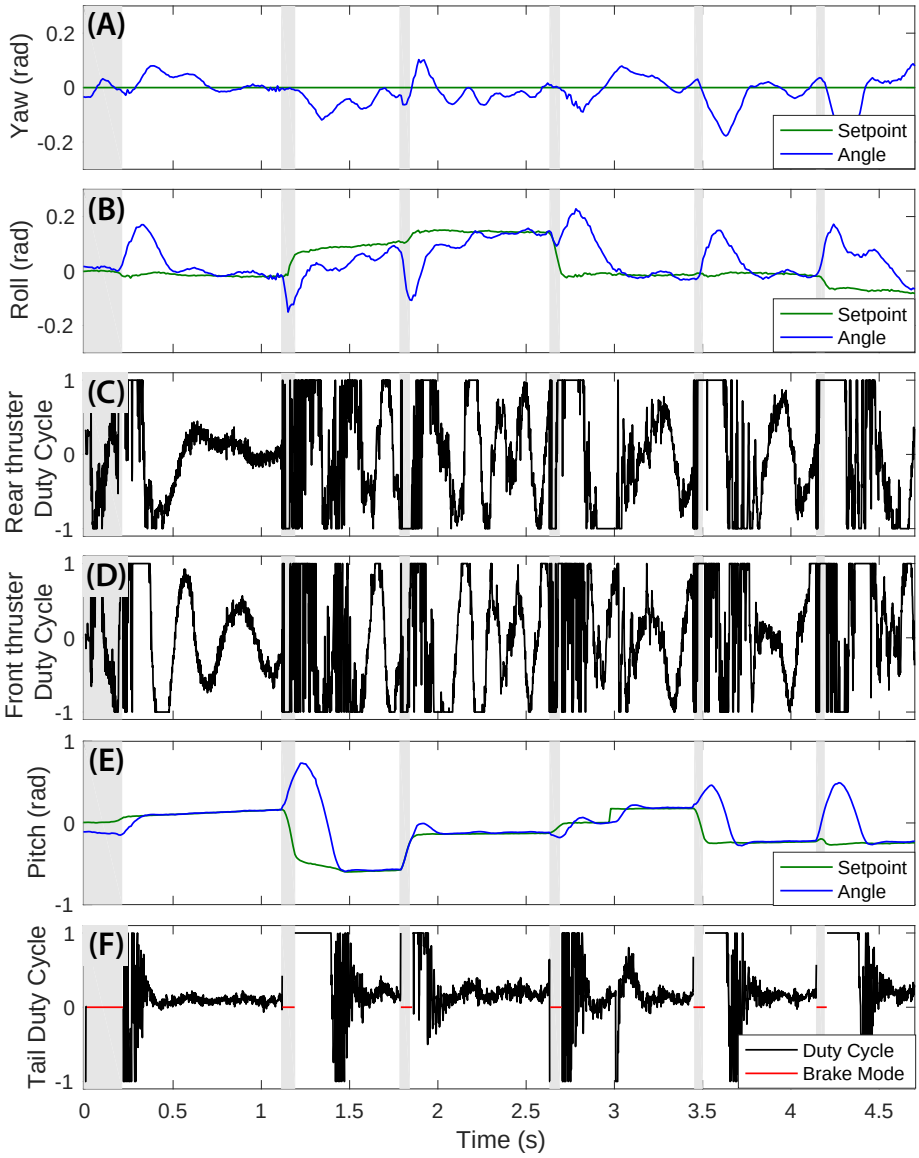

Figure 4.5: Attitude controller performance during jumping experiment. (A) Yaw angle and setpoint (B) roll angle and setpoint (C) Rear thruster motor duty cycle (D) Front thruster duty cycle (E) Pitch angle and setpoint (F) Tail motor duty cycle. Stance phases shown in grey. Adapted from [40].

trackable range of the experimental test chamber to end this experiment.

Fig. 4.7(A) shows the height of the center of gravity as a function of time for the same trial shown in Fig. 4.6a, with the stance phases shown in grey. The initial stance phase is the longest at 0.22 s, increased in duration by the SE+MA adaptation [41, 43] which allows the robot to jump higher than it would be otherwise able, 1.25 m above its starting

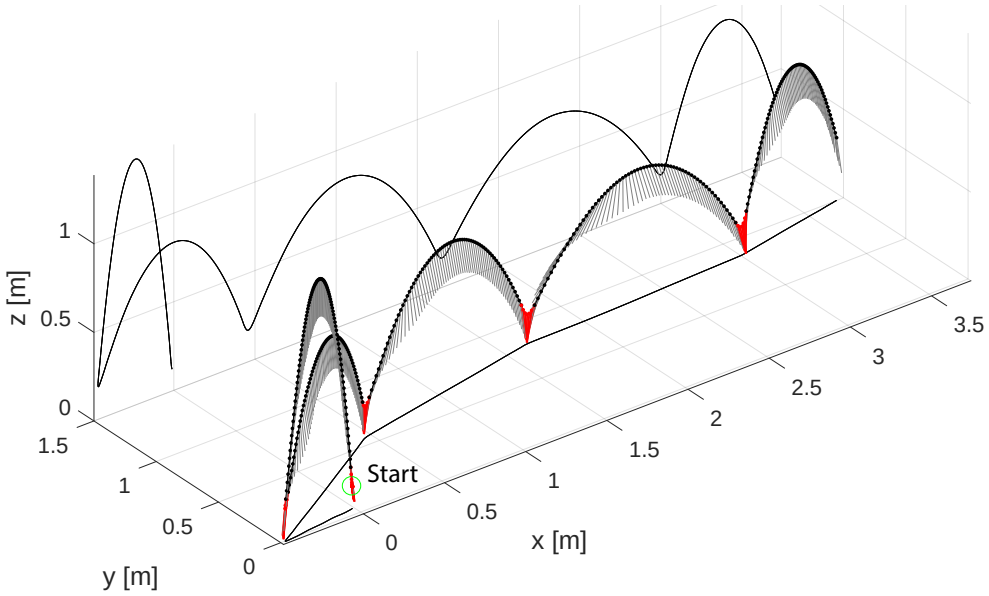

(a) Spatial trajectory of robot center of mass during a jumping experiment. Leg shown as grey in flight, red in stance. Data plotted at 10 ms intervals.

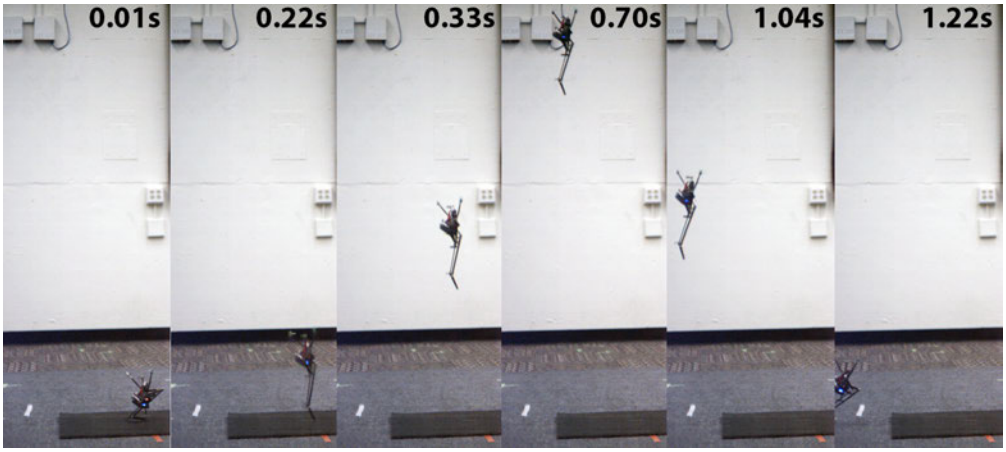

(b) Video stills from high-speed camera footage of first jump of experiment. Time is from onset of activation, aligned with Fig. 4.7.

Figure 4.6: Example data and video stills from forwards-running trial. Adapted from [40].

position, in this case. After the large initial jump, the jump height converges to the lesser height determined by the leg-thrust for this experiment. The average stance duration for this experiment was 0.057 s (not including initial stance); the average flight duration was 0.68 s, for an average duty factor of 0.077. The cumulative mechanical work done by the motor during this experiment is shown in Fig. 4.7(B). The motor inputs 1.45 J of energy during the initial stance phase, 1.2 J of which appears as extrinsic center of mass energy, for a mechanical efficiency of 83%. The energetic expense of the following jumps is less. The

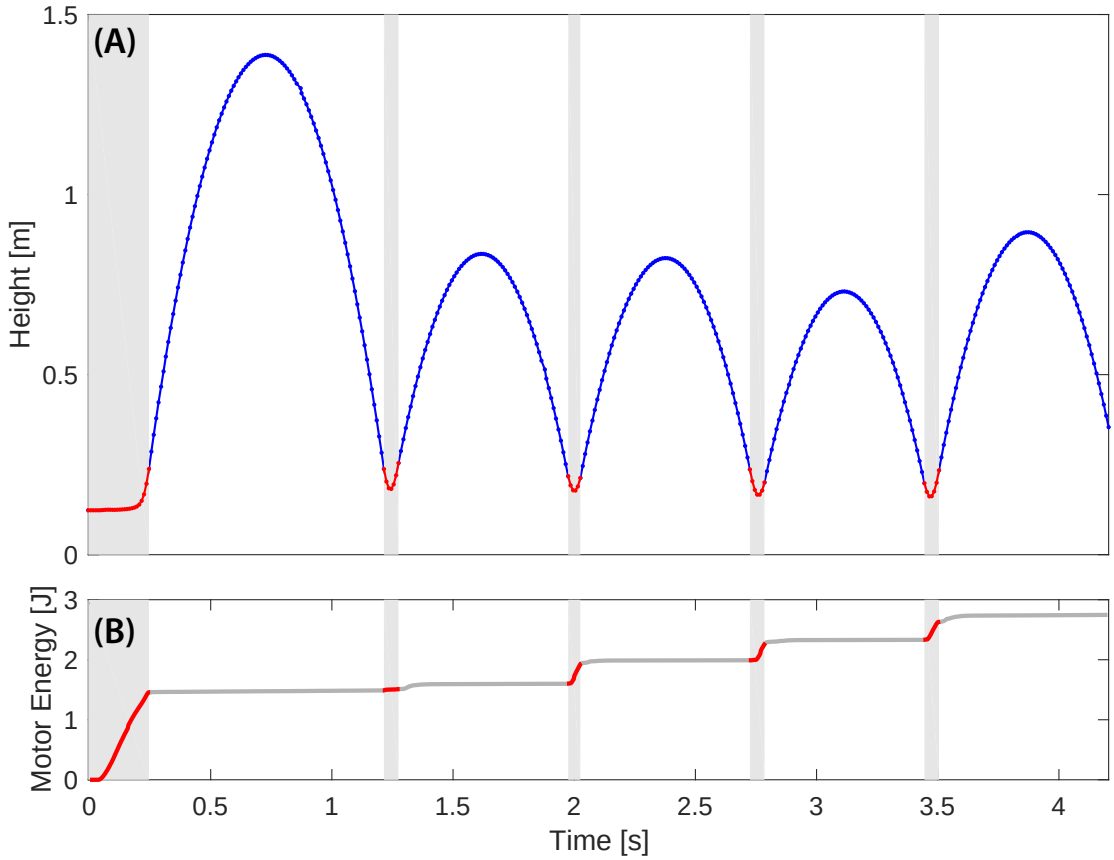

Figure 4.7: Energetics of height gain and repeated jumps. Stance periods are shown in grey. (A) height of center-of-mass (B) Cumulative mechanical energy input from motor. Adapted from [40].

series elastic leg is able to passively store and return an average of 65% of the kinetic energy; the motor inputs 0.3 J per jump to maintain height, overcoming losses from friction and impacts.

Locomotion controller

The goal of the locomotion controller was to allow Salto-1P to jump repeatedly, to explore the range of accessible jumping behaviors. We performed both in-place jumping tests wherein the robot tries to maintain a fixed $x - y$ position, and forwards-backwards running wherein the desired position is moved forwards and backwards to generate running locomotion. Fig. 4.8 shows the position of the Salto-1P's center of gravity during an in-place hopping experiment. After the robot recovers from the large intitial transient, it stays within 0.4 m of the stationary set point at (x,y) = (1,0). There is a steady state offset in the x direction which persists due to the fact that there is no integral term on the locomotion controller.

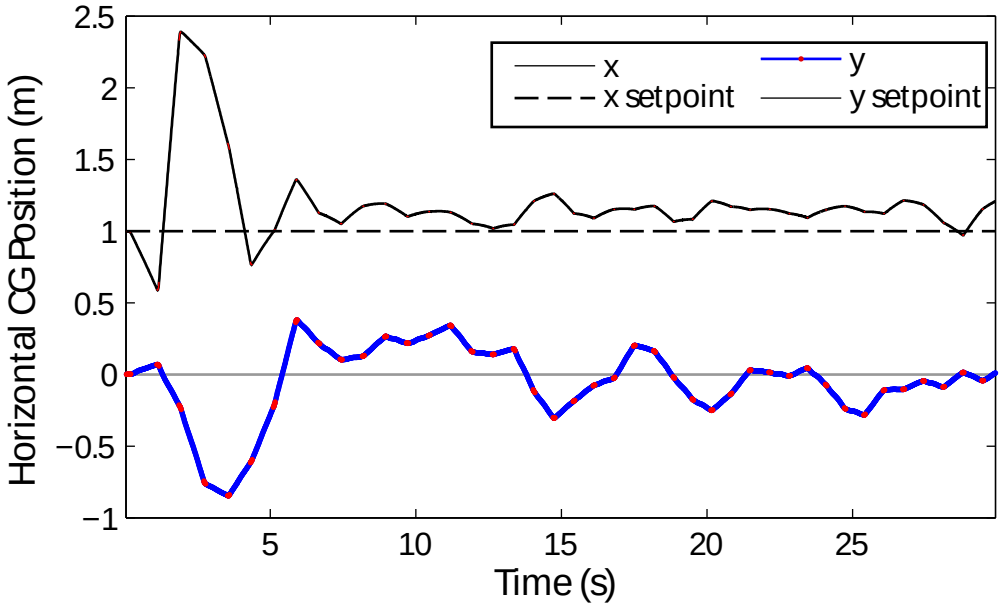

(a) Horizontal position of Salto-1P's center of mass.

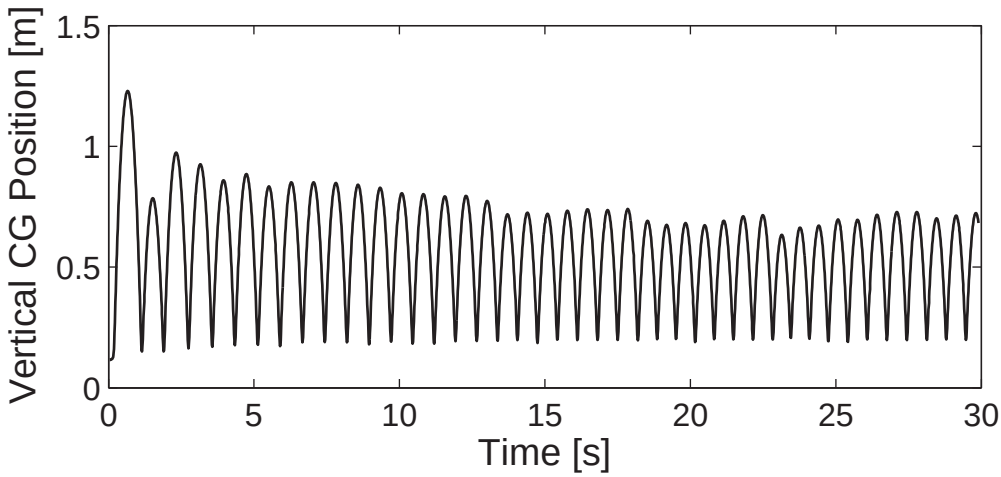

(b) Vertical position of Salto-1P's center of mass.

Figure 4.8: Motion of robot center of gravity during an in-place jumping experiment. Red portions of the trace indicate stance periods.

Fig. 4.9a shows the position of the Salto-1P's center of gravity during a forwards-backwards running experiment. Here the controller aims to maintain a 0° yaw heading and zero lateral displacement. The leg thrust in this experiment produces a modest average jump height of 0.65 m. The commanded x position is swept from 0 to 2m in a sawtooth pattern after an initial 3 second dwell at 0m. The sawtooth is repeated 10 times during which time Salto-1P makes 174 total jumps. With the exception of several deviations, the lateral

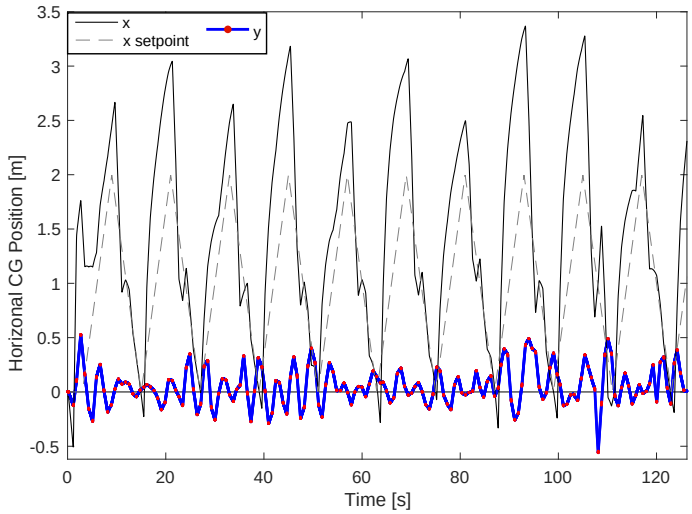

(a) Horizontal position of Salto-1P's center of mass.

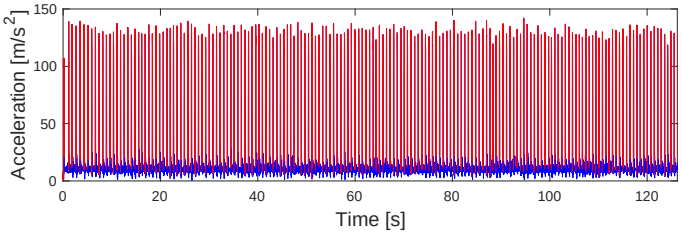

(b) Acceleration of Salto-1P's center of mass.

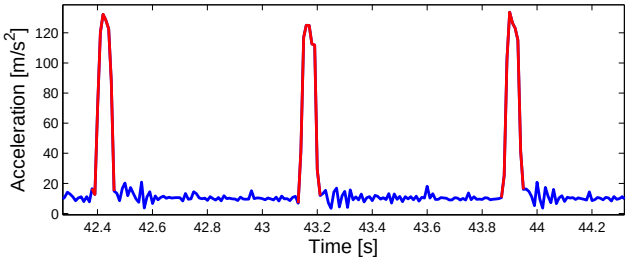

(c) Zoon-in on acceleration of Salto-1P's center of mass.

Figure 4.9: Motion of robot center of gravity during a forwards-backwards jumping experiment (174 total jumps). Red portions of the trace indicate stance periods. Adapted from [40].

position stays within 0.5m of the desired lateral position. The robot overshoots the sawtooth at the endpoints in the fore-aft direction, where the velocity changes direction. This was caused by aggressive gains on the velocity error of the center of gravity that elicited more of the dynamic character of Salto-1P than was appropriate for this locomotion task. The magnitude of Salto-1P's center of mass acceleration is shown in Fig. 4.9b.

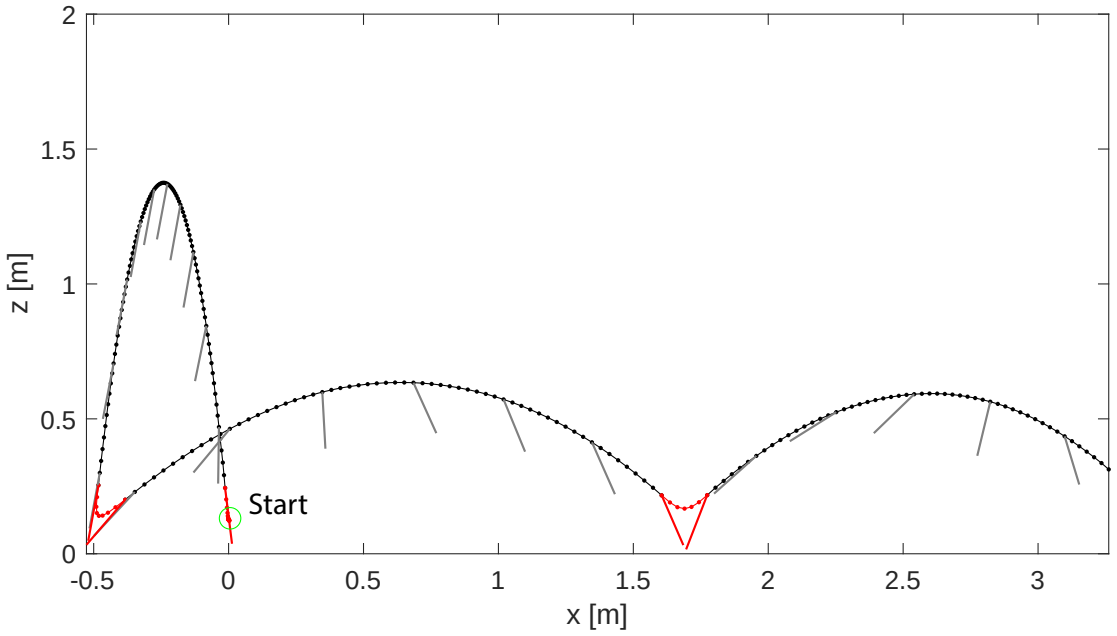

Figure 4.10: Vertical and horizontal position of Salto-1P during horizontal impulse experiment. Leg shown as grey in flight, red in stance. Leg drawn at touchdown and liftoff, and every 100ms in air. Adapted from [40].

Behavior exploration

With the robot operational, we sought to explore the space of feasible jumping behaviors. We ran a series of experiments varying leg thrust commands, and had the locomotion controller issue commands that would perturb the robot from a steady state locomotory behavior. Practically this meant running a forwards-backwards, and in-place hopping experiments with a set of highly-aggressive gains that produced large horizontal velocities.

The vertical and horizontal position of Salto during an experiment designed to produce a maximal horizontal impulse is shown in Fig. 4.10. Here the robot performs a maximal jump to start the experiment, touches down with a steep leg angle that causes a single-stride Δv_x of 4.2 m/s, Salto-1P then leaps over 2 meters horizontally, having room for one more stride before exiting the experimental volume.

Fig. 4.12 shows the vertical and fore-aft impulse for each of the 772 experimentally observed jumps. Most of the data are clustered around $\Delta v_x = 0$, generated from the in-place hopping experiments. Fig. 4.11 shows lateral vs fore-aft impulses; the data are clustered around $\Delta v_y = 0$ with some spread in Δv_x, driven by the forwards-backwards running experiments. The non-zero horizontal impulses were explored with forwards-backwards running trials, with the largest values found with the most aggressive gains. The largest single impulse was nearly vertical, with a magnitude of $\Delta v = 8.94$ m/s. The robot has trouble jumping below $\Delta v_z = 2$ m/s. The difficulty results because the attitude controlling actuators do not

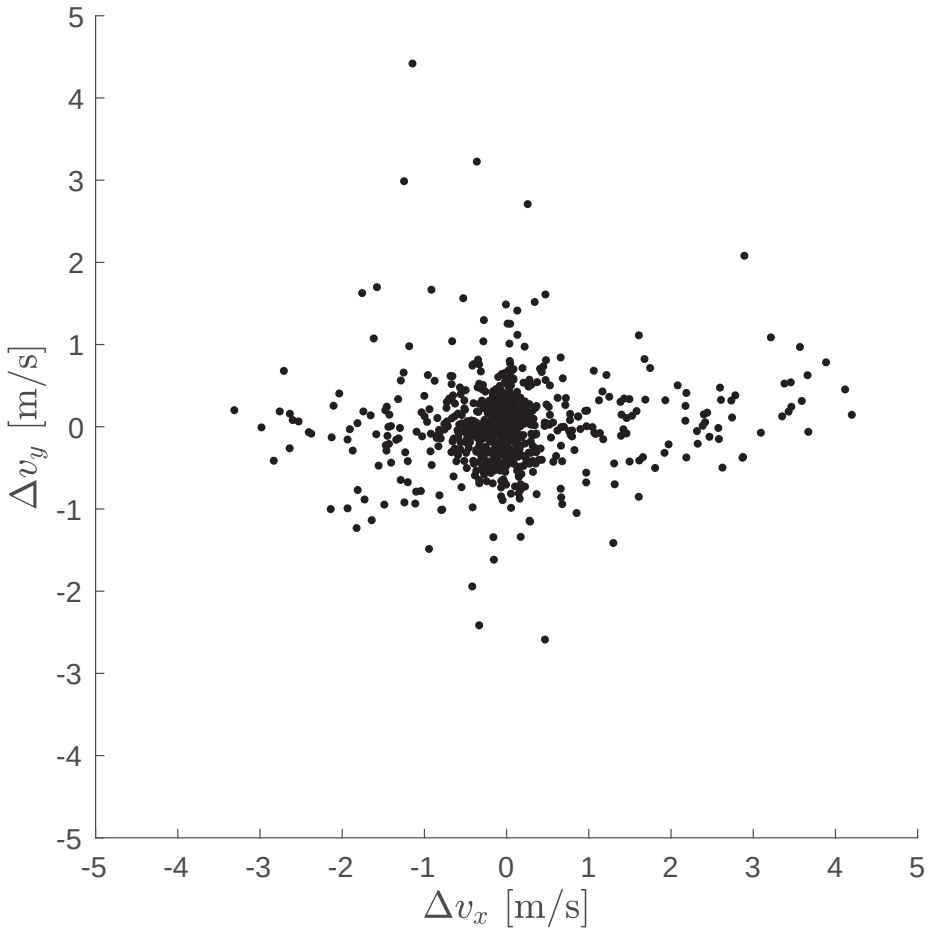

Figure 4.11: Lateral vs fore-aft impulses for each observed stance period (N=772). Adapted from [40].

have enough time to reorient the robot before the next stance event. These data are a subset of the attainable jumps; a better exploration scheme would more thoroughly establish the limits of Salto-1P's jumping capacity.

4.4 Conclusion and Future Work

In this work we introduced an improved version of a previously developed robot, Salto [43], called Salto-1P. This robot weighs 2 grams less than its predecessor and can jump 0.245 m higher, with a vertical jumping agility of 1.83 m/s, the highest recorded for any battery-powered robot. For this robot we developed a low-mass attitude control scheme that is appropriate for a highly agile, sub 0.1 kg monopedal robot. Two aerodynamic thrusters combined with an inertial tail allowed the robot to control its attitude in the air. The

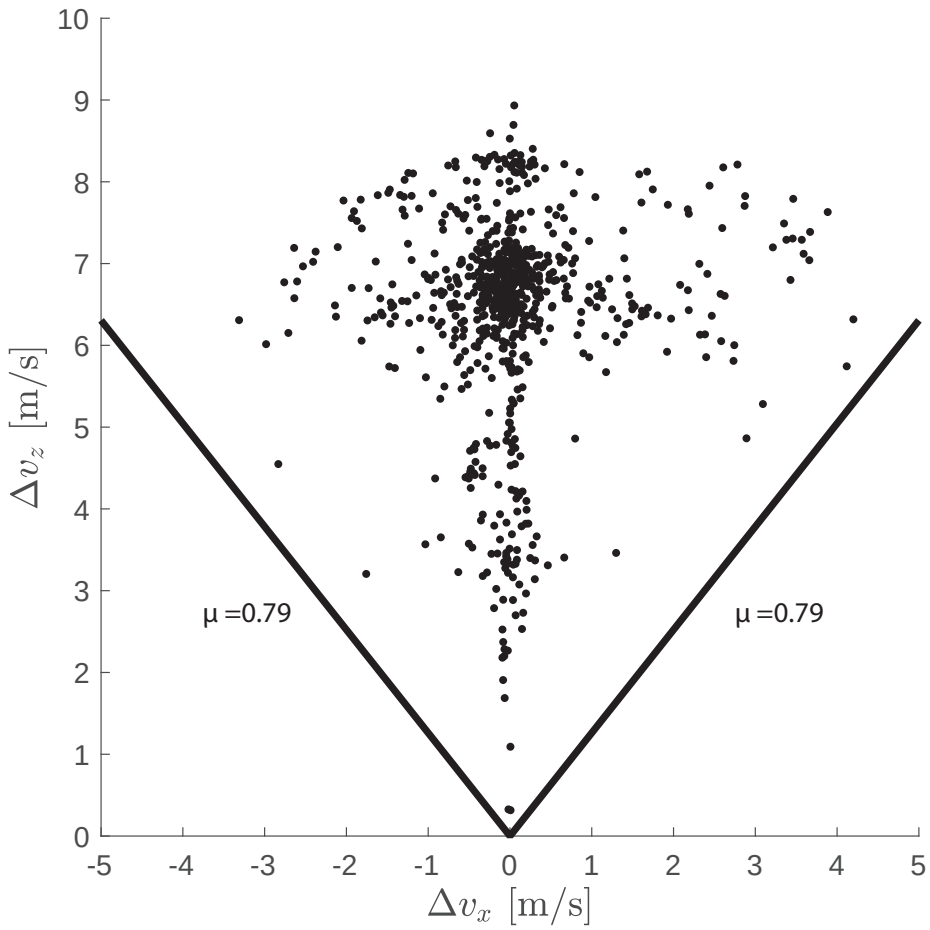

Figure 4.12: Vertical vs fore-aft impulses for each observed stance period (N=772). Friction cone for measured $\mu = 0.79$ is shown. Adapted from [40].

inertial tail was more effective at rejecting perturbations than the thrusters, which were driven to saturation regularly during the jumping trials. Greater control authority in the roll and yaw axes of the robot would expand the robot's envelope of operation.

The attitude control scheme enabled Salto-1P to execute many (up to 174 in a single trial) jumps in succession on a rigid horizontal surface. A simple linearized controller based on the Raibert step controller was used for global position control of the robot; we demonstrated both in-place hopping and forwards and backwards running. The operation of the attitude actuators in flight phase instead of stance phase meant that much smaller and less powerful actuators could be used; the thrusters could act over several-hundred milliseconds, whereas a ground-based solution would have been limited to the ≈ 50 ms stance duration.

Salto-1P is capable of exploring extreme saltatorial locomotion, demonstrating the ability to continuously jump over 1 meter in height with a duty factor as low as 0.077. Despite the challenges posed by this form of locomotion, selection/construction of appropriate robotic

hardware meant that the simple Raibert controller was able to elicit both stable locomotion and a range of dynamic maneuvers. With repeated experiments, we were able to explore the performance envelope for Salto-1P, shown in Fig. 4.11 and 4.12.

This work has shown that Salto-1P is capable of highly agile locomotion, with a maximum Δv per stance of 8.9 m/s. It has enough raw performance to be an effective platform for experimentally evaluating a recently developed ballistic planning framework [24], however full control of the platform, particularly precise landing control and foot placement, is still lacking. Future work will target development of foot placement controllers.

Chapter 5

Conclusions and Future Work

In this work we presented a power-density-first design strategy for mobile robotic platforms and evaluated it in the context of both rapid running locomotion and agile saltatorial locomotion. The basis of this strategy was to assign the task of energy production to a single centralized actuator. This increases the power-density of the platform over a traditional multiply-actuated device by removing the added mass and complexity of steering actuators that may do energetic work against each other, and do not provide propulsive effort for locomotion. The removal of the steering actuators was enabled by careful choice of kinematic structures that couple the motor to the extremities that interact with the environment. The structures were selected such that the desired behavior happens by default without the need for external control effort. When the energetic actuator in the X2-VelociRoACH was powered, the kinematic mechanism coupled to compliant legs produced stable running. When Salto's energetic actuator was activated, the leg mechanism creates a powerful jump free from rotation.

This design strategy produces robotic structures specialized for specific locomotory behaviors. More common design methodologies use multiple actuators per robotic appendage, allowing a generalized capacity to produce force in a workspace, similar to a serial-chain robotic manipulator. This capacity to produce force is then used to produce locomotion using any one of a variety of control strategies. The robots presented using the actuator-centralized approach in this work outperform all other extant robots in their respective areas. The X2-VelociRoACH is the fastest legged robot, as measured by its Froude number of 11.3. Salto-1P has the highest vertical jumping agility of any battery-powered robot at 1.84 m/s. The task-specific performance of these robots is higher than that of any comparable robot built using other design methodologies. However they lack the capacity for generalized force production that other more highly actuated robots have.

The high-frequency running experiments with X2-VelociRoACH showed that power-density is key for increasing the top speed of a robot by increasing the stride frequency. The onerous power demands at the highest speeds created a specific resistance profile that is not monotonically decreasing, a novel finding. Another contribution of this work is the SE+MA actuation strategy for jumping robots. It allows for powerful jumps while maintain-

ing all of the benefits and controllability of a series-elastic actuator. This actuation approach enabled the novel wall-jump behavior, as well as repetitive extreme-acceleration jumping.

A question for future work is how well the actuator-centralized approach works for creating robots skilled in multiple tasks. It has produced the fastest running robot and the most vertically agile jumping robot, but not one that is both. An extension of the design methodology presented here would be to adapt it to create highly-performant robots that are more adaptable. To see if a single energetic actuator is sufficient for a robot built to attain multiple objectives such as speed, jumping agility, range, rapid climbing, or flight.

The robotic platforms created in this work enable a wide body of future work. The top speed of the X2-VelociRoACH could be increased in the future by adding a flywheel to reduce the power consumption; it should be made from stronger materials that allow it to survive longer. The aerodynamic forces at top running speed could be significant and so future versions of the robot could experiment with creating lift or down-force to clear gaps or increase traction, respectively.

Salto can be used to develop more agile robotic behaviors. One such is a vaulting maneuver, a wall-jump in which the horizontal velocity does not reverse so instead the robot is propelled over the top of the wall. Salto-1P enables the exploration of 3D jumping maneuvers like using nearby walls to cross a gap and jumping between inclined planes. Salto's ability for high-power locomotion could be tested in a variety of environments, exploring the effect of compliance or granular media on agile jumping. The robot could be used to evaluate new foot designs that increase jumping performance in those same environments.

Appendix A

Salto actuation design

A.1 Specification

Salto's motor, drive train, and series-elastic element were designed based on a coarse specification of energetic requirements. We start be specifying that Salto will weigh 100 grams and jump to a height of 2.5 m. This height is an overestimate to allow for non-idealities (such as friction) in the motor, transmission, spring, and leg mechanism. We assume that all of this energy will be stored in the spring, so the needed stored energy for the jump is $E_j = 2.45$.

The input link of the leg mechanism travels $\theta_s = 4.36$ radians for full extension of the leg. If we assume a linear spring then we can determine that the stiffness required to store the energy over this stroke is:

$$k = \frac{2E_j}{\theta_s^2}$$

and the maximum motor torque after gearing is:

$$\tau_s = \frac{2E_j}{\theta_s}$$

Note the we have sought to minimize the maximum torque (by maximizing the angular stroke) so that less gearing is required, and the reflected inertia of the motor is less.

For Salto, $k = 0.26$Nm/rad and $\tau_s = 1.1$Nm.

A.2 Spring

The spring is a conically shaped latex element (developed by Rollinson et al. [85]) that is loaded in torsion. It is cut from thick walled latex tube, commercially available in a range of diameters for spear-gun applications. The goal is to have the spring as compact as possible, subject of the limitations of available dimensions and a maximum strain of 350%. The conic shape ensures that all of the elastic material is evenly loaded. A coarse identification found

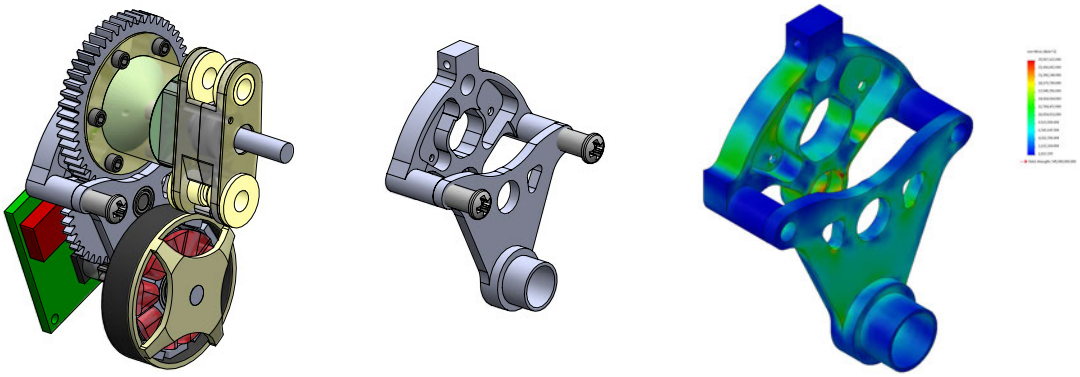

(a) Salto's transmission assembled with motor driver, spring, and input link

(b) The frame of Salto's transmission

(c) FEA resolts of frame of Salto's transmission

Figure A.1: Salto's transmission

that the shear modulus of latex is $G = 0.43$ MPa. Given an outer radius r_o, inner radius r_i, and desired stiffness k, the length of the conic section is determined as:

$$l = 2\pi \frac{r_o G}{3k}(r_o^3 - r_i^3)$$

Using 9/16" diameter tube with a 1/8" inner diameter (*McMaster*, 5234K681) yields a spring 9mm long, with a maximum shear strain of 346%. Due to nonlinear elastic effects, the spring deflects axially when deformed torsionally. This expansion is constrained by the addition of a thrust-bearing (seen in Fig.A.2) to avoid deforming the mechanism or transferring inappropriate force into the body.

The spring was cut using a 3D printed jig with a No-11 Techni Edge blade. To bond the spring to the polyurethane coupling (shown in Fig.A.2), the polyurethane was sanded with 80 grit sand paper, cleaned with isopropyl alcohol, and then Loctite 495 cyanoacrylate adhesive to attach the latex element to the polyurethane.

A.3 Transmission

Salto's transmission is shown in Fig.A.1a, assembled with the series-elastic spring and input-link of the leg mechanism. Fig.A.1b shows the mass-optimized transmission body. A cut-away view of the transmission is shown in Fig.A.2.

The bill of materials for the transmission housing is shown in TableA.1. The total inclusive mass of the transmission with the motor driver, all wiring and components, etc... is 24.78 g. The bounding dimensions of the assembled transmission are 32.4mm x 51.9mm x 23.3mm.

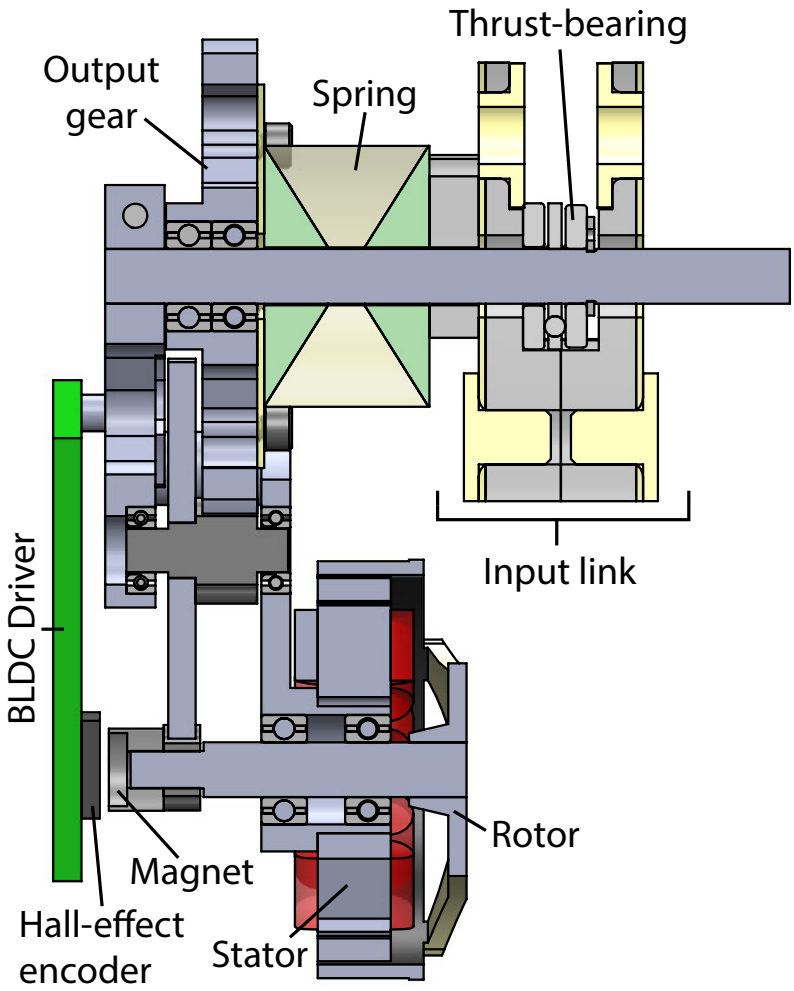

Figure A.2: Cutaway view of Salto's transmission.

Table A.1: Bill of Materials

Description	Quantity	Vendor	Catalog No.
6mm OD, 3mm ID, 2.5mm Width ball bearing	4	McMaster-Carr	7804K124
3/16" OD, 3/32" ID, 1/16" Width ball bearing	2	McMaster-Carr	57155K344
0-80 Socket-head cap screw	8	McMaster-Carr	91251A052
2-56 Phillips-head screw	2	McMaster-Carr	91772A265

Motor

Salto's actuator starts as a Scorpion S-1804-1650Kv brushless DC motor. With the stock winding its torque constant is 0.0058Nm/A, with a 0.4Ω phase resistance and suggested

Table A.2: GEARS

Description	Module (mm)	Face-width (mm)	Teeth	Material	Gear bending stress (MPa)	Gear contact stress (MPa)	Vendor	Catalog No.
Motor pinion	0.5	1.5	8	Brass	184	951	SDP-SI	A 1B 1MY05008
Compound gear-a	0.5	1.5	40	2024 Aluminum	105	951	SDP-SI	S10T05M040A0303
Compound gear-b	0.5	3.125	10	S45C Mild steel	291	1068	SDP-SI	KSSS0.5-10
Output gear	0.5	3.125	50	2024 Aluminum	166	1068	SDP-SI	S10T05M050A0303

maximum current of 5A. To reach the required 1.1 Nm, Salto would need a gear reduction of 38.3:1. To minimize mechanical weight and complexity we specify that the transmission will only use two stages of reduction. The maximum practicable reduction per stage of a spur gear train is slightly more than 5:1, so we choose the maximum reduction for Salto to be 25:1. This would require a current supply to the motor of 7.5A. To reduce the required current (and thus voltage-drop in the battery), we rewound the motor with 48 turns of 30 AWG wire to double the torque constant and thereby halve the required current.

Gears

Salto's transmission uses COTS gears (Table A.2) that have been custom machined. Gear dimensions and parameters were found using AGMA stress equations. We optimized for low weight and used aluminum gears in both stages. Aluminum has poor wear characteristics as compared to steel, but the weight savings are significant. The gears are shown in Fig.A.3.

Frame

The frame of the transmission, shown in Fig. A.1b was designed for maximum stiffness and minimum weight. The rough shape was found using topology optimization. This shape was then refined with a detailed CAD model and iterative FEA analysis (shown in Fig.A.1c). The frame is designed in two pieces so that both can be made simultaneously in a CNC mill using one-sided milling operations.

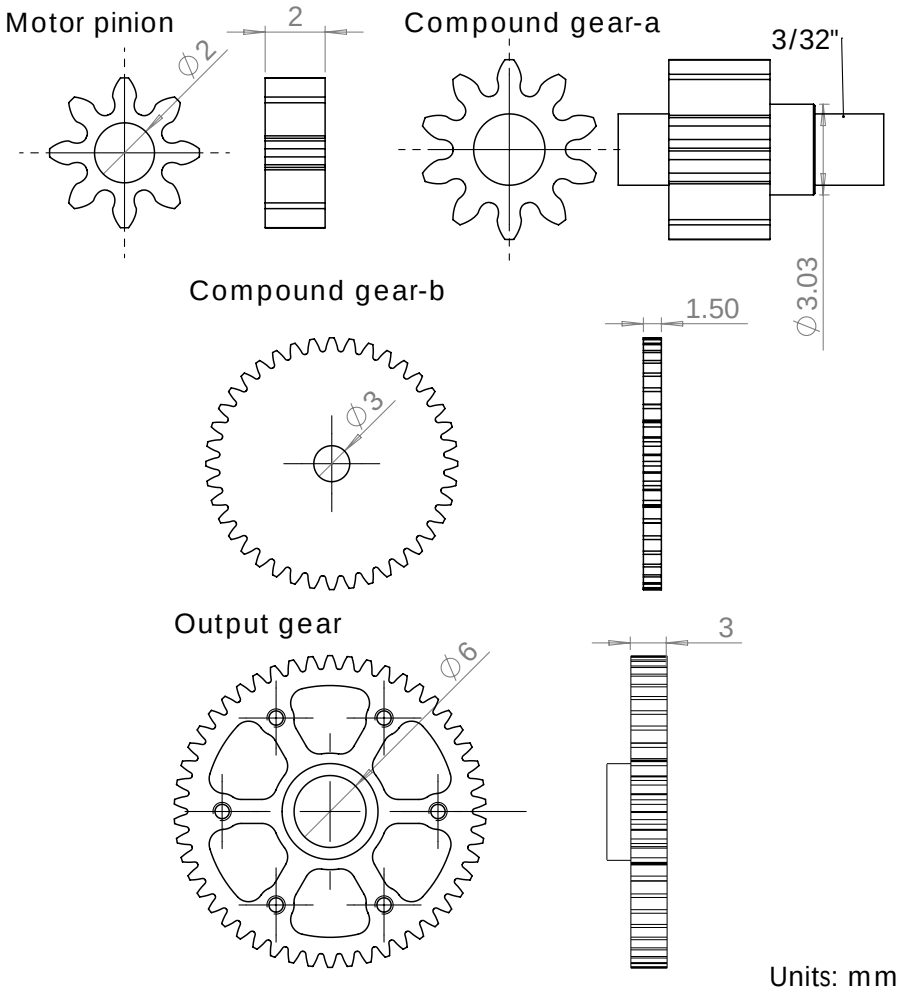

Figure A.3: CAD diagram of gears in Salto's transmission.

Bibliography

[1] Andy Abate, Ross L. Hatton, and Jonathan W. Hurst. "Passive-dynamic leg design for agile robots". In: *IEEE Int. Conf. Intell. Robot. Syst.* (2015), pp. 4519–4524. ISSN: 1050-4729. DOI: 10.1109/ICRA.2015.7139825.

[2] P. Aerts. "Vertical jumping in Galago senegalensis: the quest for an obligate mechanical power amplifier". In: *Philos. Trans. R. Soc. B Biol. Sci.* 353.1375 (1998), pp. 1607–1620. ISSN: 0962-8436. DOI: 10.1098/rstb.1998.0313. URL: http://rstb.royalsocietypublishing.org/cgi/doi/10.1098/rstb.1998.0313.

[3] R. McNeill Alexander. "A dynamic similarity hypothesis for the gaits of quadrupedal mammals". In: *J. Zool.* (1983), pp. 135–152.

[4] Anani Ananiev, Thorsten Michelfelder, and Ivan Kalaykov. "Driving Redundant Robots by a Dedicated Clutch-Based Actuator". In: *Robot Motion Control* 360 (2007), pp. 167–176.

[5] Ben Andrews et al. "Running over unknown rough terrain with a one-legged planar robot." In: *Bioinspir. Biomim.* 6.2 (2011), p. 026009. ISSN: 1748-3190. DOI: 10.1088/1748-3182/6/2/026009.

[6] Rhodri Armour et al. "Jumping robots: a biomimetic solution to locomotion across rough terrain". In: *Bioinspir. Biomim.* 2.3 (2007), S65–82. ISSN: 1748-3190. DOI: 10.1088/1748-3182/2/3/S01. URL: http://www.ncbi.nlm.nih.gov/pubmed/17848786.

[7] Henry C. Astley et al. "Chasing maximal performance: a cautionary tale from the celebrated jumping frogs of Calaveras County". In: *J. Exp. Biol.* 216.Pt 21 (2013), pp. 3947–3953. ISSN: 1477-9145. DOI: 10.1242/jeb.090357. URL: http://www.ncbi.nlm.nih.gov/pubmed/24133149.

[8] Stanley S. Baek, Fernando L Garcia Bermudez, and Ronald S. Fearing. "Flight control for target seeking by 13 gram ornithopter". In: *IEEE Int. Conf. Intell. Robot. Syst.* (2011), pp. 2674–2681. DOI: 10.1109/IROS.2011.6094581.

[9] Stanley S. Baek, Kevin Y. Ma, and Ronald S. Fearing. "Efficient resonant drive of flapping-wing robots". In: *IEEE Int. Conf. Intell. Robot. Syst.* (2009), pp. 2854–2860. DOI: 10.1109/IROS.2009.5354725.

[10] A. T. Baisch et al. "High speed locomotion for a quadrupedal microrobot". In: *Int. J. Rob. Res.* (2014). ISSN: 0278-3649. DOI: 10.1177/0278364914521473. URL: http://ijr.sagepub.com/cgi/doi/10.1177/0278364914521473.

[11] Maciej Bartos. "Alternative predatory tactics in a juvenile jumping spider". In: *J. Arachnol.* 36.2 (2008), pp. 300–305. ISSN: 0161-8202. DOI: 10.1636/CSt107-134.1.

[12] M. D. Berkemeier and Ronald S. Fearing. "Tracking fast inverted trajectories of the underactuated acrobot". In: *IEEE Trans. Robot.* 15.4 (1999), pp. 740–750.

[13] Paul Michael Birkmeyer, Kevin C. Peterson, and Ronald S. Fearing. "DASH: A dynamic 16g hexapedal robot". In: *IEEE Int. Conf. Intell. Robot. Syst.* (2009), pp. 2683–2689. DOI: 10.1109/IROS.2009.5354561.

[14] Reinhard Blickhan. "The spring-mass model for running and hopping". In: *J. Biomech.* 22.11-12 (1989), pp. 1217–1227.

[15] Reinhard Blickhan and Robert J. Full. "Locomotion energetics of the ghost crab". In: *Jnl. Exp. Biol.* 130 (1987), pp. 155–174.

[16] Reinhard Blickhan and Robert J. Full. "Similarity in multilegged locomotion: Bouncing like a monopode". In: *Jnl. Comp. Physiol. A Neuroethol. Sensory, Neural, Behav. Physiol.* 173.5 (1993), pp. 509–517.

[17] Thiago Boaventura et al. "Dynamic torque control of a hydraulic quadruped robot". In: *IEEE Int. Conf. Robot. Autom.* (2012), pp. 1889–1894. DOI: 10.1109/ICRA.2012.6224628. URL: http://ieeexplore.ieee.org/lpdocs/epic03/wrapper.htm?arnumber=6224628.

[18] Maarten F. Bobbert. "Dependence of human squat jump performance on the series elastic compliance of the triceps surae: a simulation study". In: *J. Exp. Biol.* 204.3 (2001), pp. 533–542. ISSN: 0022-0949.

[19] Anna Brill et al. "Tail-assisted rigid and compliant legged leaping". In: *IEEE Int. Conf. Intell. Robot. Syst.* (2015), pp. 6304–6311.

[20] B. Brown and G. Zeglin. "The bow leg hopping robot". In: *IEEE Int. Conf. Robot. Autom.* 1 (1998), pp. 781–786. ISSN: 1050-4729. DOI: 10.1109/ROBOT.1998.677072. URL: http://ieeexplore.ieee.org/lpdocs/epic03/wrapper.htm?arnumber=677072.

[21] C. Y. Brown, Dana E. Vogtmann, and Sarah Bergbreiter. "Efficiency and effectiveness analysis of a new direct drive miniature quadruped robot". In: *IEEE/RSJ Int. Conf. Robot. Autom.* (2013), pp. 5631–5637. URL: http://ieeexplore.ieee.org/xpls/abs{_}all.jsp?arnumber=6631386.

[22] Austin D. Buchan, Duncan W. Haldane, and Ronald S. Fearing. "Automatic identification of dynamic piecewise affine models for a running robot". In: *2013 IEEE/RSJ Int. Conf. Intell. Robot. Syst.* (2013), pp. 5600–5607. DOI: 10.1109/IROS.2013.6697168. URL: http://ieeexplore.ieee.org/lpdocs/epic03/wrapper.htm?arnumber=6697168.

[23] J. Burdick and P. Fiorini. "Minimalist jumping robots for celestial exploration". In: *Int. J. Rob. Res.* 22.7-8 (2003), pp. 653–674. ISSN: 0278-3649. DOI: 10.1177/02783649030227013. URL: http://ijr.sagepub.com/cgi/doi/10.1177/02783649030227013.

[24] Mylene Campana and Jean-Paul Laumond. "Ballistic motion planning". In: *IEEE Int. Conf. Intell. Robot. Syst.* 2016, pp. 1410–1416. ISBN: 9781509037612. DOI: 10.1109/IROS.2016.7759230.

[25] Evan Chang-Siu et al. "A nonlinear feedback controller for aerial self-righting by a tailed robot". In: *IEEE Int. Conf. Robot. Autom.* 2013, pp. 32–39. ISBN: 9781467356411. DOI: 10.1109/ICRA.2013.6630553.

[26] Jonathan E. Clark et al. "Design of a bio-inspired dynamical vertical climbing robot". In: *Robot. Sci. Syst.* (2007).

[27] Stephen M. Deban et al. "Extremely high-power tongue projection in plethodontid salamanders". In: *J. Exp. Biol.* 210.Pt 4 (2007), pp. 655–667. ISSN: 0022-0949. DOI: 10.1242/jeb.02664. URL: papers2://publication/doi/10.1242/jeb.02664.

[28] Amir Degani et al. "The ParkourBot - A dynamic BowLeg climbing robot". In: *Proc. - IEEE Int. Conf. Robot. Autom.* (2011), pp. 795–801. ISSN: 10504729. DOI: 10.1109/ICRA.2011.5979937.

[29] Alexis Lussier Desbiens et al. "Efficient jumpgliding: Theory and design considerations". In: *IEEE Int. Conf. Robot. Autom.* (2013), pp. 4451–4458. ISSN: 10504729. DOI: 10.1109/ICRA.2013.6631209.

[30] J. J. M. Driessen. "Machine and behaviour co- design of a powerful minimally actuated hopping robot". Masters. TU Delft, 2015, p. 100.

[31] Jeffrey M. Duperret et al. "Towards a comparative measure of legged agility". In: *Springer Tracts Adv. Robot.* Vol. 109. 2016, pp. 3–16. DOI: 10.1007/978-3-319-23778-7_1.

[32] Robert J. Full. "Mechanics and Energetics of Terrestrial Locomotion: Bipeds to Polypeds". In: *Energy Transform. Cells Org.* Verlag, 1989.

[33] Robert J. Full. "The Concepts of Efficiency and Economy in Land Locomotion". In: *Effic. Econ. Anim. Physiol.* Ed. by R. W. Blake. Cambridge Univ Pr, 1991, pp. 97–131.

[34] Robert J. Full and M S Tu. "Mechanics of a rapid running insect: two-, four- and six-legged locomotion." In: *Jnl. Exp. Biol.* 156 (1991), pp. 215–31. ISSN: 0022-0949.

[35] A. Galantis and R. C. Woledge. "The theoretical limits to the power output of a muscle-tendon complex with inertial and gravitational loads". In: *Proc. R. Soc. B Biol. Sci.* 270.1523 (2003), pp. 1493–1498. ISSN: 0962-8452. DOI: 10.1098/rspb.2003.2403. URL: http://rspb.royalsocietypublishing.org/cgi/doi/10.1098/rspb.2003.2403.

[36] Christian Gehring et al. "An optimization approach to controlling jump maneuvers for a quadrupedal robot". In: *Dyn. Walk.* (2015).

[37] Jurriaan H. de Groot and Johan L. van Leeuwen. "Evidence for an elastic projection mechanism in the chameleon tongue". In: *Proc. Biol. Sci.* 271.1540 (2004), pp. 761–70. ISSN: 0962-8452. DOI: 10.1098/rspb.2003.2637. URL: http://www.pubmedcentral.nih.gov/articlerender.fcgi?artid=1691657{\&}tool=pmcentrez{\&}rendertype=abstract.

[38] Duncan W. Haldane and Ronald S. Fearing. "Running beyond the bio-inspired regime". In: *IEEE Int. Conf. Robot. Autom.* (2015), pp. 4539–4546.

[39] Duncan W. Haldane and Ronald S. Fearing. "Using dynamic similarity scaling to inspire the design of a high-speed hexapedal millirobot". In: *Soc. Integr. Comp. Biol.* 2013.

[40] Duncan W. Haldane, Justin K. Yim, and Ronald S. Fearing. "Repetitive extreme-acceleration (14-g) spatial jumping with Salto-1P". In: *Submitt. to IEEE Int. Conf. Intell. Robot. Syst.* (2017).

[41] Duncan W. Haldane et al. "A power modulating leg mechanism for monopedal hopping". In: *IEEE Int. Conf. Intell. Robot. Syst.* (2016), pp. 4757–4764.

[42] Duncan W. Haldane et al. "Animal-inspired Design and Aerodynamic Stabilization of a Hexapedal Millirobot". In: *IEEE/RSJ Int. Conf. Robot. Autom.* (2013).

[43] Duncan W. Haldane et al. "Robotic vertical jumping agility via series-elastic power modulation". In: *Sci. Robot.* 1.1 (2016). URL: http://robotics.sciencemag.org/content/robotics/1/1/eaag2048.full.pdf.

[44] Tyson H. Harty. "The role of the vertebral column during jumping in quadrupedal mammals." PhD thesis. Oregon State University, 2010.

[45] Ross L. Hatton et al. "Geometric maneuverability with applications to low Reynolds number swimming". In: *IEEE Int. Conf. Intell. Robot. Syst.* 2 (2011), pp. 3893–3898. ISSN: 2153-0858. DOI: 10.1109/IROS.2011.6048659.

[46] G. Clark Haynes et al. *Laboratory on legs: an architecture for adjustable morphology with legged robots*. Tech. rep. Philadelphia, PA: University of Pennsylvania, 2012. DOI: 10.1117/12.920678. URL: http://proceedings.spiedigitallibrary.org/proceeding.aspx?articleid=1354436.

[47] Norman C. Heglund, C. R. Taylor, and T. A. McMahon. "Scaling stride frequency and gait to animal size: mice to horses." In: *Science* 186.4169 (1974), pp. 1112–3. ISSN: 0036-8075. URL: http://www.ncbi.nlm.nih.gov/pubmed/4469699.

[48] H. T. Henry. "Performance of guinea fowl Numida meleagris during jumping requires storage and release of elastic energy". In: *J. Exp. Biol.* 208.17 (2005), pp. 3293–3302. ISSN: 0022-0949. DOI: 10.1242/jeb.01764. URL: http://jeb.biologists.org/cgi/doi/10.1242/jeb.01764.

[49] Katie L. Hoffman and Robert J. Wood. "Passive undulatory gaits enhance walking in a myriapod millirobot". In: *IEEE/RSJ Int. Conf. Intell. Robot. Syst.* 2 (2011), pp. 1479–1486.

[50] Aaron M. Hoover and Ronald S. Fearing. "Fast scale prototyping for folded millirobots". In: *IEEE Int. Conf. Robot. Autom.* (2008), pp. 886–892.

[51] Aaron M. Hoover et al. "Bio-inspired design and dynamic maneuverability of a minimally actuated six-legged robot". In: *IEEE Int. Conf. Biomed. Robot. Biomechatronics* (2010), pp. 869–876. ISSN: 2155-1774. DOI: 10.1109/BIOROB.2010.5626034.

[52] Penny E. Hudson, Sandra A. Corr, and Alan M. Wilson. "High speed galloping in the cheetah (Acinonyx jubatus) and the racing greyhound (Canis familiaris): spatio-temporal and kinetic characteristics." In: *J. Exp. Biol.* 215.14 (2012), pp. 2425–34. ISSN: 1477-9145. DOI: 10.1242/jeb.066720. URL: http://www.ncbi.nlm.nih.gov/pubmed/22723482.

[53] Fumiya Iida, R. Dravid, and C. Paul. "Design and control of a pendulum driven hopping robot". In: *IEEE Int. Conf. Intell. Robot. Syst.* 2002, pp. 2141–2146. ISBN: 0-7803-7398-7. DOI: 10.1109/IRDS.2002.1041584. URL: http://ieeexplore.ieee.org/lpdocs/epic03/wrapper.htm?arnumber=1041584.

[54] Guowu Jia, Guang Chen, and Ming Xie. "Design of a novel compact dexterous hand for teleoperation". In: *IEEE Int. Symp. Comput. Intell. Robot. Autom.* (2001), pp. 5–10. DOI: 10.1109/CIRA.2001.1013164.

[55] Aaron M. Johnson and Daniel E. Koditschek. "Toward a vocabulary of legged leaping". In: *IEEE Int. Conf. Robot. Autom.* (2013), pp. 2568–2575. ISSN: 10504729. DOI: 10.1109/ICRA.2013.6630928.

[56] Gwang-Pil Jung et al. "An integrated jumping-crawling robot using height-adjustable jumping module". In: *IEEE Int. Conf. Robot. Autom.* (2016), pp. 4680–4685.

[57] Hamidreza Karbasi, Jan Paul Huissoon, and Amir Khajepour. "Uni-drive modular robots: Theory, design, and experiments". In: *Mech. Mach. Theory* 39.2 (2004), pp. 183–200. ISSN: 0094114X. DOI: 10.1016/S0094-114X(03)00113-7.

[58] Gavin Kenneally, Avik De, and Daniel E. Koditschek. "Design principles for a family of direct-drive legged robots". In: *Robot. Sci. Syst. Work.* 1.2 (2015), pp. 17–19. ISSN: 23773766. DOI: 10.1109/LRA.2016.2528294.

[59] Sangbae Kim, Jonathan E. Clark, and Mark R. Cutkosky. "iSprawl: Design and Tuning for High-speed Autonomous Open-loop Running". In: *Int. Jnl. Robot. Res.* 25.9 (2006), pp. 903–912. ISSN: 0278-3649. DOI: 10.1177/0278364906069150.

[60] N. J. Kohut et al. "Aerodynamic steering of a 10 cm high-speed running robot". In: *IEEE Int. Conf. Robot. Autom.* (2013), pp. 5593–5599. ISSN: 21530858. DOI: 10.1109/IROS.2013.6697167.

[61] N. J. Kohut et al. "Precise dynamic turning of a 10 cm legged robot on a low friction surface using a tail". In: *IEEE Int. Conf. Robot. Autom.* (2013), pp. 3299–3306. ISSN: 10504729. DOI: 10.1109/ICRA.2013.6631037.

[62] Mirko Kovač et al. "A miniature 7g jumping robot". In: *IEEE Int. Conf. Robot. Autom.* 2008, pp. 373–378. ISBN: 978-1-4244-1646-2. DOI: 10.1109/ROBOT.2008.4543236. URL: http://ieeexplore.ieee.org/lpdocs/epic03/wrapper.htm?arnumber=4543236.

[63] Mirko Kovač et al. "The EPFL jumpglider: A hybrid jumping and gliding robot with rigid or folding wings". In: *IEEE Int. Conf. Robot. Biomimetics* (2011), pp. 1503–1508. DOI: 10.1109/ROBIO.2011.6181502.

[64] Matthew Lattanzio. "Escape tactic plasticity of two sympatric Norops (Beta Anolis) species in Northeast Costa Rica". In: *Amphibia-Reptilia* 30 (2009), pp. 1–6. ISSN: 0173-5373. DOI: 10.1163/156853809787392658.

[65] Pierre Legreneur et al. "Hindlimb interarticular coordinations in Microcebus murinus in maximal leaping." In: *J. Exp. Biol.* 213.Pt 8 (2010), pp. 1320–7. ISSN: 1477-9145. DOI: 10.1242/jeb.041079. URL: http://www.ncbi.nlm.nih.gov/pubmed/20348344.

[66] David Lentink, Stefan R. Jongerius, and Nancy L. Bradshaw. "The Scalable Design of Flapping Micro-Air Vehicles Inspired by Insect Flight". In: *Fly. Insects Robot.* Ed. by Dario Floreano et al. Berlin, Heidelberg: Springer-Verlag Berlin Heidelberg, 2010, pp. 185–205. ISBN: 978-3-540-89392-9. DOI: 10.1007/978-3-540-89393-6. URL: http://link.springer.com/10.1007/978-3-540-89393-6.

[67] Fei Li et al. "Jumping like an insect: Design and dynamic optimization of a jumping mini robot based on bio-mimetic inspiration". In: *Mechatronics* 22.2 (2012), pp. 167–176. ISSN: 09574158. DOI: 10.1016/j.mechatronics.2012.01.001. URL: http://dx.doi.org/10.1016/j.mechatronics.2012.01.001.

[68] Thomas Libby et al. "Tail-assisted pitch control in lizards, robots and dinosaurs". In: *Nature* 481.7380 (2012), pp. 181–4. ISSN: 1476-4687. DOI: 10.1038/nature10710. URL: http://www.ncbi.nlm.nih.gov/pubmed/22217942.

[69] R. L. Marsh and H. B. John-Alder. "Jumping performance of hylid frogs measured with high-speed cine film". In: *J. Exp. Biol. Biol.* 188 (1994), pp. 131–41. ISSN: 0022-0949. URL: http://www.ncbi.nlm.nih.gov/pubmed/7964379.

[70] J. Melville and R. Swain. "Evolutionary correlations between escape behaviour and performance ability in eight species of snow skinks (Niveoscincus : Lygosominae) from Tasmania". In: *J. Zool.* 261.2003 (2003), pp. 79–89. ISSN: 09528369. DOI: Doi10.1017/S0952836903003984.

[71] Talia Y. Moore and Andrew A. Biewener. "Outrun or outmaneuver: predator-prey Interactions as a model system for integrating biomechanical studies in a broader ecological and evolutionary context". In: *Integr. Comp. Biol.* 55.6 (2015), pp. 1188–1197. ISSN: 15577023. DOI: 10.1093/icb/icv074.

[72] Minkyun Noh et al. "Flea-Inspired Catapult Mechanism for Miniature Jumping Robots". In: *IEEE Trans. Robot.* 28.5 (2012), pp. 1007–1018. ISSN: 1552-3098. DOI: 10.1109/TRO.2012.2198510. URL: http://ieeexplore.ieee.org/lpdocs/epic03/wrapper.htm?arnumber=6204349.

[73] H. Nolle. "Linkage coupler curve synthesis: A historical review - I. Developments up to 1875". In: *Mech. Mach. Theory* 9.2 (1974), pp. 147–168. ISSN: 0094114X. DOI: 10.1016/0094-114X(74)90034-2.

[74] D. Paluska and Hugh M. Herr. "Series elasticity and actuator power output". In: *IEEE Int. Conf. Robot. Autom.* May (2006), pp. 1830–1833. DOI: 10.1109/ROBOT.2006.1641972. URL: http://ieeexplore.ieee.org/lpdocs/epic03/wrapper.htm?arnumber=1641972.

[75] Hae Won Park, Sangin Park, and Sangbae Kim. "Variable-speed quadrupedal bounding using impulse planning: Untethered high-speed 3D Running of MIT Cheetah 2". In: *IEEE Int. Conf. Robot. Autom.* Vol. 2015-June. June. 2015, pp. 5163–5170. ISBN: 9781479969227. DOI: 10.1109/ICRA.2015.7139918.

[76] Hae-won Park, Patrick M. Wensing, and Sangbae Kim. "Online planning for autonomous running jumps over obstacles in high-speed quadrupeds". In: *Robot. Sci. Syst.* (2015).

[77] S. N. Patek et al. "Linkage mechanics and power amplification of the mantis shrimp's strike". In: *J. Exp. Biol.* 210.20 (2007), pp. 3677–3688. ISSN: 0022-0949. DOI: 10.1242/jeb.006486. URL: http://jeb.biologists.org/cgi/doi/10.1242/jeb.006486.

[78] James Douglass Penn. "A Multiple Degree of Freedom Actuator Using a Single Vibrating Transducer". PhD thesis. Massachusetts Institute of Technology, 2012.

[79] Mark M. Plecnik and J. Michael McCarthy. "Design of Stephenson linkages that guide a point along a specified trajectory". In: *Mech. Mach. Theory* 96 (2016), pp. 38–51. ISSN: 0094114X. DOI: 10.1016/j.mechmachtheory.2015.08.015. URL: http://dx.doi.org/10.1016/j.mechmachtheory.2015.08.015.

[80] Mark M. Plecnik et al. "Design exploration and kinematic tuning of a power modulating jumping monopod". In: *J. Mech. Robot.* 9 (2016), pp. 1–13. ISSN: 1942-4302. DOI: 10.1115/1.4035117.

[81] A. O. Pullin et al. "Dynamic turning of 13 cm robot comparing tail and differential drive". In: *IEEE Int. Conf. Robot. Autom.* (2012), pp. 5086–5093.

[82] M. H. Raibert, H. Benjamin Brown, and M. Chepponis. "Experiments in balance with a 3D one-legged hopping machine". In: *Int. J. Rob. Res.* 3.2 (1984), pp. 75–92. ISSN: 0278-3649. DOI: 10.1177/027836498400300207.

[83] T. J. Roberts and R. L. Marsh. "Probing the limits to muscle-powered accelerations: lessons from jumping bullfrogs". In: *J. Exp. Biol.* 206.15 (2003), pp. 2567–2580. ISSN: 0022-0949. DOI: 10.1242/jeb.00452. URL: http://jeb.biologists.org/cgi/doi/10.1242/jeb.00452.

[84] Thomas J. Roberts and Emanuel Azizi. "Flexible mechanisms: the diverse roles of biological springs in vertebrate movement". In: *J. Exp. Biol.* 214.Pt 3 (2011), pp. 353–361. ISSN: 0022-0949. DOI: 10.1242/jeb.038588.

[85] David Rollinson et al. "Design and modeling of a series elastic element for snake robots". In: *ASME DSCC*. 2013. ISBN: 978-0-7918-5612-3. DOI: 10.1115/DSCC2013-3875. URL: http://proceedings.asmedigitalcollection.asme.org/proceeding.aspx?doi=10.1115/DSCC2013-3875.

[86] Ajij Sayyad, B. Seth, and P. Seshu. "Single-legged hopping robotics research - A review". In: *Robotica* 25.05 (2007), pp. 587–613. ISSN: 0263-5747. DOI: 10.1017/S0263574707003487. URL: http://www.journals.cambridge.org/abstract{_}S0263574707003487.

[87] Umberto Scarfogliero, Cesare Stefanini, and Paolo Dario. "Design and development of the long-jumping "grillo" mini robot". In: *IEEE Int. Conf. Robot. Autom.* April. 2007, pp. 467–472. ISBN: 1424406021. DOI: 10.1109/ROBOT.2007.363830.

[88] Sangok Seok et al. "Design principles for energy-efficient legged locomotion and implementation on the MIT Cheetah robot". In: *IEEE/ASME Trans. Mechatronics* (2014), pp. 1–13. ISSN: 1083-4435. DOI: 10.1109/TMECH.2014.2339013. URL: http://ieeexplore.ieee.org/lpdocs/epic03/wrapper.htm?arnumber=6880316.

[89] Reay H. N. Smithers. "The Mammals of Botswana". Ph. D. University of Pretoria, 1971, p. 340.

[90] Theodore Stankowich and Richard G. Coss. "Effects of risk assessment, predator behavior, and habitat on escape behavior in Columbian black-tailed deer". In: *Behav. Ecol.* 18.2 (2007), pp. 358–367. ISSN: 10452249. DOI: 10.1093/beheco/arl086.

[91] Sascha A. Stoeter et al. "Autonomous stair-hopping with scout robots". In: *IEEE Int. Conf. Intell. Robot. Syst.* 1 (2002), pp. 721–726. DOI: 10.1109/IRDS.2002.1041476. URL: http://ieeexplore.ieee.org/lpdocs/epic03/wrapper.htm?arnumber=1041476.

[92] Gregory P. Sutton and M. Burrows. "Biomechanics of jumping in the flea." In: *J. Exp. Biol.* 214.Pt 5 (2011), pp. 836–47. ISSN: 1477-9145. DOI: 10.1242/jeb.052399. URL: http://www.ncbi.nlm.nih.gov/pubmed/21307071.

[93] Takashi Tsuda, Hiromi Mochiyama, and Hideo Fujimoto. "Quick stair-climbing using snap-through buckling of closed elastica". In: *Int. Symp. Micro-NanoMechatronics Hum. Sci.* (2012), pp. 368–373. DOI: 10.1109/MHS.2012.6492485.

[94] Sam Van Wassenbergh et al. "Extremely fast prey capture in pipefish is powered by elastic recoil". In: *J. R. Soc. Interface* 5.20 (2008), pp. 285–296. ISSN: 1742-5689. DOI: 10.1098/rsif.2007.1124.

[95] B. Vanderborght et al. "Variable impedance actuators: A review". In: *Rob. Auton. Syst.* 61.12 (2013), pp. 1601–1614. ISSN: 09218890. DOI: 10.1016/j.robot.2013.06.009.

[96] T. E. Wei, G. M. Nelson, and R. D. Quinn. "Design of a 5-cm monopod hopping robot". In: *IEEE Int. Conf. Robot. Autom.* (2000), pp. 2828–2833. ISSN: 10504729. DOI: 10.1109/ROBOT.2000.846456. URL: http://ieeexplore.ieee.org/xpls/abs{_}all.jsp?arnumber=846456.

[97] Joel D. Weingarten et al. "Automated Gait Adaptation for Legged Robots". In: *IEEE Int. Conf. Robot. Autom.* (2004), pp. 2153–2158. ISSN: 10504729. DOI: 10.1109/ROBOT.2004.1307381.

[98] By Peter Weiss. "Hop Hopbots!" In: *Sci. News* 159 (2001).

[99] M. A. Woodward and M. Sitti. "MultiMo-Bat: A biologically inspired integrated jumping-gliding robot". In: *Int. J. Rob. Res.* 33 (2014), pp. 1511–1529. ISSN: 0278-3649. DOI: 10.1177/0278364914541301. URL: http://ijr.sagepub.com/cgi/doi/10.1177/0278364914541301.

[100] Y. Yesilevskiy, Weitao Xi, and C. D. Remy. "A comparison of series and parallel elasticity in a monoped hopper". In: *IEEE Int. Conf. Robot. Autom.* (2015), pp. 1036–1041. DOI: 10.1109/ICRA.2015.7139304.

[101] V. Zaitsev et al. "Locust-inspired miniature jumping robot". In: *IEEE Int. Conf. Intell. Robot. Syst.* 2015, pp. 553–558. ISBN: 9781479999941. DOI: 10.1109/IROS.2015.7353426. URL: http://dx.doi.org/10.1088/1748-3190/10/6/066012.

[102] G. Zeglin and B. Brown. "Control of a bow leg hopping robot". In: *IEEE Int. Conf. Robot. Autom.* 1.May (1998), pp. 793–798. ISSN: 1050-4729. DOI: 10.1109/ROBOT.1998.677082. URL: http://ieeexplore.ieee.org/lpdocs/epic03/wrapper.htm?arnumber=677082.

[103] G. Zeglin and H. Benjamin Brown. "First Hops of the 3D Bow Leg Hopper". In: *5th Int. Conf. Climbing Walk. Robot.* (2002), pp. 357–364.

[104] Jianguo Zhao, Tianyu Zhao, and Ning Xi. "Controlling aerial maneuvering of a miniature jumping robot using its tail". In: *IEEE/RSJ Int. Conf. Intell. Robot. Syst.* 29.3 (2013), pp. 3802–3807. URL: http://ieeexplore.ieee.org/xpls/abs{_}all.jsp?arnumber=6696900.

[105] Jianguo Zhao et al. "Development of a controllable and continuous jumping robot". In: *IEEE Int. Conf. Robot. Autom.* (2011), pp. 4614–4619. DOI: 10.1109/ICRA.2011.5980166. URL: http://ieeexplore.ieee.org/lpdocs/epic03/wrapper.htm?arnumber=5980166.